PhD thesis in physics

Integration of tunneling magnetoresistive sensors for high resolutive magnetic particle detection

Written by

Camelia Albon

Department of Physics
Bielefeld University
November 2009

PhD thesis in physics

Integration of tunneling magnetoresistive sensors for high resolutive magnetic particle detection

Written by

Camelia Albon

Department of Physics
Bielefeld University
November 2009

I hereby declare that I wrote this thesis by myself and used none but the indicated resources.

Bielefeld, 7th November 2009

(Camelia Albon)

Reviewers:
Prof. Dr. Andreas Hütten
Prof. Dr. Armin Gölzhäuser

Preface

The development of nanotechnology pushes the limits of biomedicine in regions where the size of solid state based devices and biomolecules are in the same range of magnitude. The integration of bionanodevices in the molecular diagnostic field leads towards improvements in our life quality by assuring fast and cheap diagnosis devices. Low cost production hand-held biochips are foreseen to be incorporated in the next generation of bionanodevices. Among them, tunneling magnetoresistive (TMR) biosensors are of great interest and their improvements constitute the subject of the present thesis.

The construction of TMR sensors is realized by employing e-beam lithography and ion beam etching means in order to obtain a detection system of an increased sensitivity. The magnetic biosensors based on TMR effect are downscaled to submicron dimensions and have been used for the detection of different magnetic markers. The sensors exhibit an increased spatial resolution, being able to distinguish different 1 μm bead orientations towards the sensor by examining the detected signal. Their sharp sensing properties are proven by detecting 14 nm Co nanoparticles, where different interaction processes gave rise to specific signals. Several advances have been performed for a proper integration of low noise TMR sensors with microfluidic and magnetic beads manipulative systems in order to sense the dynamic motion of the magnetic beads above the sensors area.

The TMR biosensors are foreseen to have several applications in cell and molecular biology. By integrating the TMR sensors in biological environment, a breakthrough can be expected in achieving information about drug delivery systems or interactions between biomolecules.

Publications

C. Albon, A. Weddemann, A. Auge, K. Rott, A. Hütten, *Tunneling magnetoresistance sensors for high resolutive particle detection*, Applied Physics Letters, Vol 95, Issue 2, (2009) Pages: 023101-023101-3

C. Albon, A. Weddemann, A. Auge, D. Meissner, P. Jutzi, K. Rott, A. Hütten, *Number sensitive detection and direct imaging of dipolar coupled magnetic nanoparticles by tunnel magnetoresistive sensors,* Applied Physics Letters, Vol 95, Issue 16, (2009) Pages: 163106-163106-3 - selected for the November 2, 2009 issue of Virtual Journal of Nanoscale Science & Technology

A. Weddemann, A. Auge, C. Albon, F. Wittbracht, A. Hütten, *On the resolution limits of tunnel magnetoresistance sensors for particle detection*, accepted for publication in New Journal of Physics 11 (2009)

A. Weddemann, A. Auge, C. Albon, F. Wittbracht, A. Hütten, *Towards the magnetoresistive detection of single magnetic nanoparticles: new strategies for particle detection by adjustment of sensor shape,* submitted to Applied Physics Letters

Conferences

DPG-Tagung 2007, Regensburg – *Poster* – "Using a highly sensitive TMR sensor array for the detection of moving biomolecules"

Nanobionics IV – from molecules to applications, 2007 Marburg –*Talk* - "Using a highly sensitive TMR sensor array for the detection of superparamagnetic beads"

DPG-Tagung 2008, Berlin – *Talk*- "The use of nanometer size tunneling magnetoresistance sensors in the detection of superparamagnetic beads"

The 10th Conference of Biosensors, 2008, Shanghai – *Keynote Talk*- "Tunneling magnetoresistance sensors towards single molecule detection"

DPG-Tagung 2009, Dresden –*Talk*- "Highly sensitive detection of magnetic markers by tunnelinng magnetoresistance sensors"

BioImaging 2009, Bielefeld – *Poster* - "Tunneling magnetoresistance array for high precision magnetic bead detection"

Table of Contents

1. Introduction

1.1 Biosensors – description and application

In present days, the boundaries between different science fields disappear and leave place to the introduction of new composed research areas. Improvements required in life quality and safety leads to the development of novel research strategies. The recent introduced research fields have the aim to develop new systems that will find their applicability in life sciences. The latest discoveries in physics can be exploited to their full potential if they are integrated in biological sciences. Further and continuous progress is needed for the discovery of new treatments in different medical problems.

The biosensor term include a combination between physics which came out with the recognition and transmission of a signal produced by a biological environment and the biological science that comprise the systems which produce the signal. The human body has integrated in its structure great sensitive receptors that give birth to the receptive organs as eye, skin, ear, nose and tongue. The biosensors construction is based on the function system of the receptive organs. The signal that is detected and transmitted by the physical part of a biosensor can have various forms. It can consist of different types of modifications, such as: electrical changes (electric potential, electric current, electric conductance, electric impedance), intensity and phase of electromagnetic radiation changes, mass change, temperature change, viscosity change, change of pH, heat transfer, uptake or release of gases or a magnetic change (1). The biologically sensed elements vary also and give specificity to the sensing procedure. They can include enzymes (the history of biosensors begins with the first enzyme electrodes developed in 1962 by the scientist L.C. Clark), antibody, nucleic acid, cell, microbial or polysaccharides. Combining the two parts of the biosensor sometimes requires additional elements known as markers which label the connection between the biological elements and the physical sensing parts. Employing labels in biodetection is sometimes used to increase the sensitivity of detection, but for some types of sensors it is a mandatory requirement. The first types of labels used in biomedicine were the radioisotopes,

but now, due to their radiation risk are being replaced. Other used labels are the ones that have fluorescent, luminescent or light scattering properties and can be easily detected and counted under the optical microscope. The enzymatic type of labeling is widely adopted to produce a chemical reaction with the analytes and to detect through the result of the chemical reaction the concentration of the analyte. The recent label generation includes magnetic nanoparticles, nanocrystals and quantum dots (2). A short description of a biosensor is visualized in Fig.1.1. The implementation of markers in biosensing systems requires proper functionalization processes that demand a high care and can always be a source of contamination for the biological molecular compounds or destruction for the physical part of the biosensor. By considering the labeling procedures, the biosensors can be divided in main classes: the ones that don't require any markers utilization, which are more convenient in use due to their simplicity and the ones that employ markers handling. Other parameters that characterize the sensors are their sensitivity, specificity, selectivity together with their easy portability and low cost production. In the next subchapter the types of biosensors already assigned and the ones on the way of development will be classified. Up to the present day, pregnancy tests and glucose sensors are probably the most popular types of sensors used worldwide (3). The glucose sensors help the diabetics to monitor and keep their disease under control, decreasing the side effects of their condition. The improvements that have been arisen in the nanotechnological field (nanowires, quantum dots) are expected to emerge on the biosensors developments (4). It is awaited that the implementation of novel technologies in biomedicine will surely lead to highly sensitive and less invasive sensors (5). By considering all the information above it is comprehensible why humanity has high expectations from biosensors in the future. One long-time goal expected to be accomplished is the real time monitoring of different analytes (level of different hormones, enzymes in the blood,

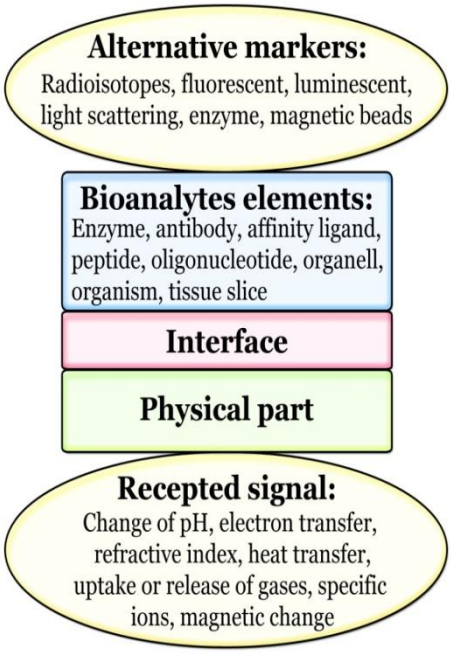

Fig. 1.1 Schematic representation of a biosensor

different hormones in the bloodstream) with an "*in vivo*" device for proper diagnostic (6). In this manner the effect of medication can be carefully controlled and react in time in case of adverse reactions to allergens, infectious agents or toxins. With the help of such devices, it might be possible to achieve a better understanding of the drug delivery mechanism at the cellular level, which could increase the quality of medicine in the future. A short term goal of the biosensors is the development of hand held "*in vitro*" diagnostic devices suitable for intermittent use. By this, a fast specific diagnostic can be produced with minimum body injury. Considering the importance of life safety, other approach of biosensors should include the detection of different pollutants in the environment such as pesticides, toxins, food pathogens or even biological warfare agents (3).

Types of biosensors

The first developed category of sensors, which embraced a lot of success on the market were the electrochemical biosensors. These can be divided in conductimetric, amperometric or potentiometric biosensors. Their working principle is based on the detection of ions or electrons released from chemical reactions where the analytes to be measured take part. A short description of this class of biosensors can be found in Anex 1. The biosensors based on an antibody-antigen reaction are called immunosensors. The conductimetric biosensors detect changes that appear in the conductance of the solution where the analytes are measured. The change is proportional with the amount of analyte present in solution. These types of sensors are enzyme labeled and are used for the detection of e.g. paracetamol, creatinine, L-asparagine, penicillin G and glucose (7) and have a low sensitivity (1). The amperometric sensors are also enzyme labeled (if the analytes are not electroactive, a chosen enzyme will catalyze the chemical reaction) and measure the changes of the current produced in the solution. These high sensitive biosensors lead to the development of glucose sensors, where the amount of glucose in blood is proportional to the output signal. The glucose sensors revolutionized the biosensors market and the next generations are expected to be more sensitive and minimally invasive, such as implantable subcutaneous glucose electrodes.

The potentiometric biosensors measure potential differences caused by the changes in electrolytes due to antigen-antibody reactions. The major advantage of this type of sensors is their labelness, being more comfortable in use. The limiting factor of

the label free devices is the risk of detecting unspecific analytes. The potentiometric biosensors are divided further into: FET (field effect transisor) sensors, pH electrodes and gas sensing electrodes.

The FET sensors are based on field effect transistor devices, where the charge change produced by biomolecules give rise to carriers disequilibrium in the semiconductor that can be measured further as an electrical signal which is proportional to the concentration of the analyzed sample. The idea of integrating the solid state physics with the bimolecular recognition was revolutionary at that time (8), so modern biosensors devices are based on the combination between the two technologies.

The following class includes the thermal biosensors, which are based on the detection of the enzyme catalyzed reactions accompanied by heat production (25-100 kJ/mol). Those are used to sense e.g. pesticides, pathologic bacteria, cholesterol, glucose, ATP, urea, triglicerides, acorbic acid, lactose, ethanol, penicillin or sucrose.

The optical biosensors class is also well developed and, as a consequence is divided into two large areas: the one that include a signal generating label and the one that detect directly the optical signal.

Optical sensors based on luminescence spectroscopy use an enzyme as a label and can supervise the light coming from a bioluminescent (high sensitive) or chemiluminiscent reaction. The direct optical sensors normally don't require any label, but a fluorescent label can be used to increase the sensitivity of detection. As shown in Anex 3, this sensor category is divided into: holographic sensors, fluorescence, reflectance, ellipsometric, SPR and waveguide sensors. The waveguide sensors are also split into fiber optic waveguide, interferometers, grating coupler and resonant mirror sensors. Of all direct optical sensors it's worth emphasizing the SPR (surface plasmon resonance) label free sensors due to their high affinity and ability of performing real time detection processes. Surface plasmon resonance appears at the interface between two materials with a dielectric constant of opposite sign (such as a metal and dielectric material) and consists of a charge density oscillation associated with an electromagnetic wave (9). The future of SPR sensors is oriented towards the detection of small concentration of analytes with the integration of microfluidic channels (10).

Other affinity sensors able to monitor real time detection are the mass detecting sensors. The detection system can be based on piezoelectric crystals or acoustic waves. The piezoelectric crystals detect mass changes because of modifications occurring in

the oscillation frequency proportional to the amount of analytes situated on the sensors surface. The disadvantage of these label free sensors consists in the impurities that might contaminate the sensor surface and give a false detection signal.

The last type of biosensors are the magnetic ones, which will be described in detail in the following subchapter because of the intensive work realized onto one of this type of sensors. This category is also split in three categories that include GMR, spin-valve and TMR sensors. The technology used for magnetic biosensors is based on the magnetoresistance effect.

Magnetic biosensors

The content of this subchapter will emphasize the description of magnetic sensors based on the magnetoresistance effect. Other types of magnetic biosensors are based on SQUID (superconducting quantum interference device) which are flux sensitive, while the biosensors based on magentoresistance effect are field sensitive sensors (11). The phenomenological description of the magnetoresistance effect will be explained in details during the next chapter. The basic principle of this phenomenon is the change in resistance of a device consisting of ferromagnetic thin films due to the relative orientation of magnetization. Three different types of magnetoresistive patterns are suitable for biological detection: giant magnetoresistance, spin valve and tunneling magnetoresistance sensors. The differences between these types of sensors are schematic exemplified in Fig. 1.2.

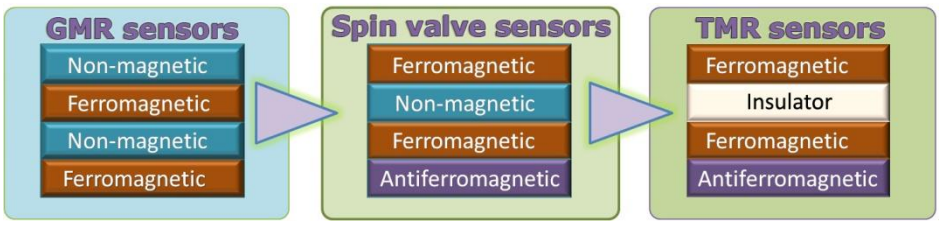

Fig. 1.2 Schematic overview of magnetoresistance sensors

The magnetoresistance sensors use magnetic labels for biodetection. The label consist of a magnetic marker, commercially available superparamagnetic beads or magnetic nanoparticles, which present a magnetic dipole moment when are magnetized. The magnetic stray field produced by the magnetic labels will influence the

changes that occur in the sensor's magnetoresistance. The magnetic tags can be functionalized with biological or chemical end-groups such as –SH, streptavidin, biotin, -COOH which are further attached to the analytes that have to be detected. A schematic overview of a magnetic bead is presented in Fig. 1.3.

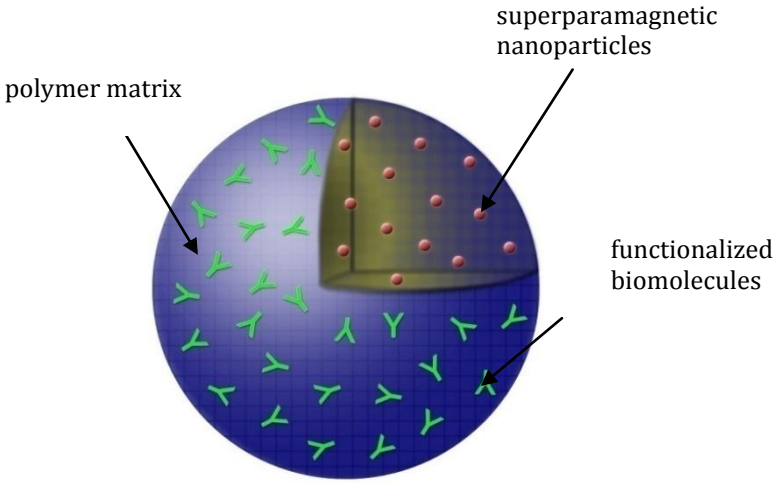

Fig. 1.3 Sketch of a magnetic bead

The employment of magnetic markers in biorecognition has the advantage of high specificity being detected only the biological analytes attached to the magnetic labels. On the other side, the functionalization of beads with biomolecules is itself an elaborate process, fact that might bring complexity to the sensing processes and therefore decrease the efficiency of this detection technique.

The magnetic makers used for detection can have superparamagnetic properties, presenting a magnetic moment only when are immersed in a magnetic field, or ferromagnetic properties, presenting a permanent magnetic moment. It is preferable to use superparamagnetic labels for magnetic detection considering their reduced agglomeration. The ferromagnetic labels have the tendency to cluster due to the attraction forces that exist between them, fact that will lead to an imprecision in the detection process. Magnetic labels can be magnetized by applying a magnetic field generated by external coils or by using on chip integrated current lines. The magnetic field produced by the coils can be produced by an AC or DC current that is passing through the coils. The orientation of the magnetic field related to the sensing layer can be in plane, angle or out-of-plane magnetic field. When conducting lines are integrated on chip and a cur-

rent is passing through these lines, a magnetic field will be formed that attracts the beads on the line surface and magnetize them at the same time (12).

The GMR effect arises from the asymmetry in the spin-dependent scattering at the non-magnetic/magnetic interfaces for spin-up and spin-down electrons. The researchers from Naval Research were the pioneers in developing a sensing device based on giant magnetoresistance (GMR) technique starting with BARC I (bead array counter) and continuing with BARC III sensors which are characterized by a current in-plane geometry. The dimension of the sensors presented by them is large, being 1.6 μm wide on a 4.0 micrometer pitch, with a total length of 8 mm within a 200 micrometers diameter circular zone (13).

Compared to GMR multilayers, where the magnetization direction depends on the non-magnetic (Cu, Ru) spacer thickness leading to oscillatory coupling, in spin-valves, the bottom ferromagnetic layer is having its magnetization pinned by exchange bias to an antiferromagnetic layer, while the top sensing layer can rotate freely. Using a standard working cell of a spin valve structure with two ferromagnetic layers separated by a Cu spacer, typical MR values of up to 11% are obtained. At the pinned layer, the exchange energy should be large, so the exchange field prevails against demagnetizing fields. For sensor applications the sensor output must be linearized. This can be achieved by inducing a transverse magnetization direction in the pinned layer, while the magnetization of the free layer is in the longitudinal direction.

The magnetic tunnel junctions (MTJ) have the working principle based on the spin dependent tunneling effect, where electrons tunnel across an insulating barrier between two ferromagnetic electrodes. MTJs have a low resistance state when the two electrode magnetizations are in parallel orientation and a high resistance state when they are in antiparallel orientation.

The sensor's sensitivity is reflected in its ability to detect a single magnetic marker. This capability is limited by the minimum field the sensor can detect. As the magnetic particle stray field is averaged over the sensor area, an increase of the sensor area comes with a decrease of the sensor sensitivity. A smaller sensor may be used to detect a small number of magnetic particles and at the limit this technology can be used for single biomolecular recognition events (14).

In the processes of bead detection it is important to take into account all the existing magnetic fields that are magnetizing the bead. It has been predicted by a theoretical

model and also correlated with experimental results that the magnetic fields produced by the magnetic layers and the magnetic field created by the current that is passing through the sensor contribute along with the external magnetic field to the bead magnetization (15).

The crossover from biosensors based on scattering processes, GMR and spin-valve sensors, to the ones based on tunneling processes relays on the high magnetoresistance ratio of MTJs. Recent developed double barrier MTJs can reach a value of up to 1056 % at room temperature (16). The increased TMR value leads to highly sensitive elements. Another advantage presented by MTJ's sensors is their large lateral resolution. Owe to this property it is possible to pattern the sensor elements in a closed-packed array with the aim of having multitask lab-on-a-chip assays. The future perspectives for biosensing devices are oriented towards integrated biochips with the possibility of rapid detection of interactions taking place at a single molecule level.

1. 2 Magnetic markers

The content of this subchapter includes a short characterization of the magnetic markers used in magnetic detection experiments with their physical characteristics and biological applications. The magnetic markers are divided into two main categories: the iron oxide based magnetic beads and the transitional metal based nanoparticles.

General characteristics of magnetic markers

The magnetic markers are used for labeling the biomolecules (enzymes, antibodies, antigens, DNA). Their size similar to biomolecules is an important property and makes them suitable for magnetic biosensors. They consist of magnetic nanoparticles embedded in a polymer matrix and are used for a wide range of applications. For biomedical applications it is necessary to accomplish the following requirements: large saturation magnetization, no coercitive field, no remanence magnetization and small size.

A short introduction in magnetic macroscopic notions is needed to comprehend the further given information regarding magnetic properties of the nanoparticles. A

magnetic dipole moment m is defined by a current I that is passing through an infinitely small loop dA.

$$\mathrm{m} = \mathrm{I} \int \mathrm{dA} \ [\mathrm{A} \cdot \mathrm{m}^2] \tag{1.2.1}$$

The magnetization M of a magnetic material consists of the total N magnetic moment per volume unit V:

$$\mathrm{M} = \mathrm{m}\frac{\mathrm{N}}{\mathrm{V}} \ [\mathrm{A/m}] \tag{1.2.2}$$

The response of a magnetic material to a magnetic field H is expressed by the magnetic induction or magnetic flux density B:

$$\mathrm{B} = \mu_0(\mathrm{H} + \mathrm{M}) \ [\mathrm{Wb/m}^2] \tag{1.2.3}$$

Where μ_0 is the magnetic permeability of free space and is dimensionalless. The relation between M and H is given by:

$$\mathrm{B} = \mu_0(1 + \chi)\mathrm{H} \tag{1.2.4}$$

Where χ is the magnetic susceptibility of the material.

If the size of a magnetic structure is less than 500 nm it is not favorable for the structure to form magnetic domains, because a typical thickness of a domain wall is:

$$\delta = \sqrt{\frac{\mathrm{JS}^2\pi^2}{\mathrm{Ka}}} \tag{1.2.5}$$

with J being the magnetic exchange constant, S the total spin quantum number of each atom, a the interatomic spacing and K the magnetic anisotropy constant for the magnetic material (17). Using equation (1.2.5), the thickness for a domain wall in iron bulk material is calculated to be 42 nm. Considering the domain wall thickness, the minimum required size for a nanoparticle with a monodomain structure can be calculated. The single domain particles have been characterized by applying the Stoner-Wolfarth model of ferromagnetism (18). The superparamagnetic behavior of magnetic nanoparticles depends entirely on the magnetic anisotropy of the material from which the nanoparticles are built. This magnetic specificity forbids the nanoparticles to agglomerate and to interfere, making them suitable for biological applications, due to the avoidance of embolism or other possible lethal side effects that can appear in a human body. In the superparamagnetic size regime, between 1-10 nm, a fluctuation of the magnetic moment of the nanoparticles exists. This is attributed to the thermal energy (k_BT) (19). So, the magnetic moments are randomly arranged and the net magnetization has a null value. When superparamagentic nanoparticles are immersed in a magnetic field, they will be uniformly magnetized (20). If the coercivity is present, it indicates a magnetic

interaction between the nanoparticles. Below the so called blocking temperature, the ferromagnetic order appears, because the magnetization relaxation process becomes slow compared to the time required for a particular investigation technique (21). In case of superparamagnetic nanoparticles, the magnetization curve is characterized by the Langevin equation as follows (22), (23):

$$M_L = M_S L\left(\frac{\mu_0 mH}{k_B T}\right) \quad (1.2.6)$$

where $L(x) = cothx - 1/x$ is the Langevin function, M_S is the saturation magnetization, μ_0 is the magnetic permeability of vacuum, m is the magnetic moment of a particle, H is the applied magnetic field, k_B is the Boltzmann constant and T is the absolute temperature.

Iron oxide based magnetic beads

The nanoparticles currently used in biomedicine are based on magnetite (Fe_3O_4) or maghemite (Fe_2O_3). Their advantages rely in their small size and non-interaction between nanoparticles. Their magnetic properties and biocompatibility has been extensively investigated, being established that they can be metabolized by the human body (through liver and kidneys). Nowadays, they are used as contrast agents in MRI techniques or as hyperthermia agents in cancer therapies. Further applications for nanoparticles are foreseen in drug delivery systems to specific location of disease, magnetic cell separation and biomolecular technology (24). Their functionalization with biomolecules is mandatory for their use in biomedicine, but due to different biological treatments, their magnetic moment can be reduced (25). The nanoparticles interchange is based on dipole-dipole interaction and exchange interactions (26), (27). Any kind of interaction between nanoparticles is suppressed if the distance between the nanoparticles is larger than three times their diameter.

The commercial magnetic beads Dynabeads® MyOne™, used for detection means in the work presented in this thesis, are formed by embedding iron oxide nanoparticles in porous monosized polymer beads and coated afterwards with a layer of polymer without charged groups (28). Individual maghemite nanoparticles in the formed magnetic beads have sizes from 6 to 12 nm. Some of them cluster and form structures of up to 20 nm. The entire bead has a size of 1.05 μm and is coated with different end-groups such as carboxylic acid, streptavidin etc. The micromagnetic beads

have been investigated with AGM (alternating gradient magnetometer), their magnetic characterization being presented in Fig. 1.4.

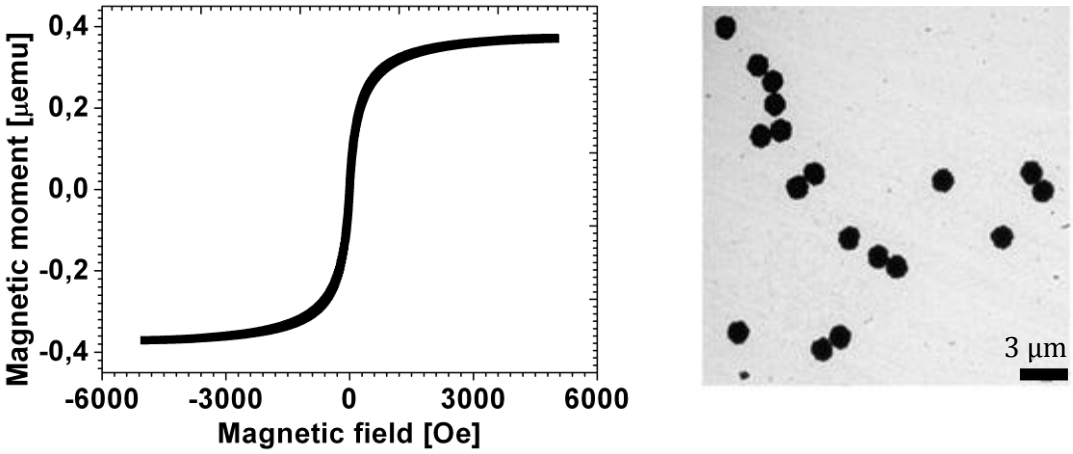

Fig.1.4 Magnetic measurements of Dynabeads® MyOne™ coated with carboxylic acid and their TEM image (taken from (29))

From the physical characteristics of the beads and their magnetic characterization, the saturation magnetic moment per particle was calculated leading to a value of m=36.2 aAm^2. The value of the magnetic moment is important when one has to consider the dipole interaction between two particles or to calculate the dipole field created by a magnetized particle that influences the magnetic biosensor. The dipole type magnetic field of the microparticle is reduced in the following form:

$$H_{dipole} = \frac{3(m\cdot\hat{r})\hat{r}-m}{r^3} \qquad (1.2.7)$$

In this equation, the $\hat{r}$ vector points from the center of the magnetic bead towards the detection point. In case of magnetic beads sensing, the detection point for the microbead is situated in the middle of the top sensing layer of the sensor.

Considering equation (1.2.7) it can be pointed out the importance of having an increased magnetic moment of the bead, with a strong stray field in order to achieve its magnetic detection.

The iron oxide based magnetic beads are embedded in different coating materials to ensure their biological applications. The polystyrene coating gives a good size distribution and spherical shape, but its hydrophobic surface leads to unspecific protein binding, so a chemically modifications of the surface is needed. The magnetic silica

based particles provide an efficient DNA and proteins binding, but improvements have to be done regarding the size distribution and spherical shape. The polysacharide coating gives good perspectives for in vitro applications, but they provide an irregular shape. The poly (lactic acid) coatings are biodegradable but their hydrofobic surface makes them susceptible to bind easily to plastic surfaces (17).

Transitional metal based nanoparticles

It has been established that the Co, CoFe and CoPt nanoparticles have higher saturation magnetization values compared to the iron oxide based nanoparticles. This can be verified by observing their magnetophoretic mobility in the same medium. It has been determined that the particles with high magnetophoretic mobility exhibit also the highest saturation magnetization (30). A detailed preparation method of magnetic nanoparticles based on transition metals is presented elsewhere (31), (32). Experimental observations showed that Co and CoFe nanoparticles alter their magnetic properties after exposure to atmospheric conditions, due to oxidation and shrinking of their magnetic volume (29). Despite their advantages related to magnetic properties, their toxicity regarding "*in vivo"* applications is an important issue that has to be investigated further. It is well known that Co is a toxic non-reactive metal that is hardly metabolized. For "*in vitro"* applications, their gains seem to be much higher owed to their high magnetic moment. Magnetic nanoparticles are considered to be excellent candidates for magnetic tags in biodetection. If they are functionalized with biomolecules of similar size (1.8÷5.3 nm), magnetic nanoparticles could be used for the detection of genetic diseases. The CoPt nanoparticles have a high anisotropy constant and due to Pt polarization present low magnetophoretic mobility. These properties make them suitable for use in data storage applications rather than in biomedical devices.

Table 1.2 Characterization of the magnetic markers used for magnetic detection

	Size	Saturation magnetic moment	Coercitive field
COOH Dynabeads	1.05 μm	370.6 μemu	2.82 Oe
Co nanoparticles	14.2 nm	800.3 μemu	47.35 Oe
CoFe nanoparticles	9.35 nm	96.75 μemu	2.33 Oe

General conclusions for magnetic markers

By summarizing the magnetic markers characteristics it should be pointed out the importance of nanoparticles in biomedicine engineering. Their reduced size comes along with a superparamagnetic behavior that makes them easy manipulative by magnetic fields. The iron oxide based nanoparticles have potential use in *"in vivo"* applications such as drug targeting, MRI contrast agents, magnetic separations etc. The nanoparticles based on Co or CoFe materials are suitable for *"in vitro"* application, due to their unknown interaction in the body system. Their *"in vivo"* appliance is desirable owed to their small size (the blocking of small blood vessels could be easily avoided), but their biocompatibility is an issue that has to be considered. Their high saturation magnetization is an advantageous property when detection by submicron sized magnetic biosensors is considered. Their labeling with single biomolecules is linking the molecular biology field with the solid state based sensing systems. This opens new research avenues in molecular and genetic engineering, where detection of processes that take place at a molecular level will help us overcoming the present limits in understanding the constitution of the building blocks of life.

Another important issue regarding magnetic biomarkers is related to their biofunctionality. The iron oxide based nanoparticles, owed to their coating can be easily functionalized with biological probes (33). The nanoparticles based on transition metals, due to their manufacture procedure are covered with an oleic acid shell. Due to that, the biofunctionalization becomes a much difficult process. Nowadays, new biochemical procedures are implemented to overcome the biofunctionalization issues.

1.3 Tunneling magneto-resistance processes

The content of this subchapter has the aim to give an overview of the characteristics and properties of magnetic thin films materials. The interacting phenomena between magnetic thin films such as magnetic coupling and tunneling magneto-resistance effect will be overviewed.

Magnetic anisotropy

Among the chemical elements it is well known that some are revealing magnetic attributes. In case of transitional elements (Fe, Co, Ni), the band magnetism occurs due to the imbalanced electrons spins in the 3d band structure. For the achievement of a favorable energy state, the exchange energy will align all the unbalanced electron spins in the same direction. The exchange energy depends on the interatomic distance and gives rise to the magnetic domains separated by the domain walls. The ferromagnetic properties of rare earth elements occur due to the localized magnetism, which are evident only at low temperatures.

Magnetocrystalline anisotropy

The magnetocrystalline anisotropy is caused by the spin-orbit coupling. The electron orbitals are linked to the crystallographic structure of the material. Due to the interaction between electron spins and electron orbitals, the electron spins will be aligned along a preferential direction that is generic called easy axis. The direction of magnetization in a bulk structure is determined by the magnetocrystalline anisotropy, while the exchange energy has the role of aligning the electron spins in the same direction. The magnetocrystalline anisotropy constant K_i is temperature and material dependent. The characteristics and properties of thin film materials are mainly controlled by the compromise between the uniaxial anisotropy K_u and the magnetocrystalline anisotropy K_i. From simulation and experimental results it has been concluded that due to the miscut in the film growth, the uniaxial anisotropy is vanishing when the thin film thickness is higher than 3.1 nm (34), (35). The formation of single domain states is preferred in structures composed of very thin films with a lateral dimension of less than 500 nm.

Shape anisotropy

If the magnetic material has finite length, poles will form at the surface giving rise to a stray field E_{stray} outside the material. In order to counteract the stray field, a demagnetizing H_{demag} field inside the material is produced.

$$E_{\text{stray}} = -\frac{1}{2}\int \mu_0 M H_{\text{demag}} dV \tag{1.3.1}$$

The shape anisotropy constant is:

$$K^V_{\text{shape}} \approx -M^2 < 0 \qquad K^V_{\text{shape}} > K_i \tag{1.3.2}$$

The shape anisotropy dominates the magnetocrystalline anisotropy and favors the alignment of magnetization towards a preferential direction given by the shape of the magnetic element. In case of an elliptic element, the orientation of magnetization will be uniformly aligned along the large axis. By increasing the thickness of the thin film layer, the stray field of the submicron size element will increase also. The magnetocrystalline anisotropy can be counteracted by the shape anisotropy only in elements of low dimensions ($< 500\ nm$).

Magnetic domains

An important aspect that has to be pointed out in the magnetic thin film behavior is related to magnetic domains. These are regions where all unbalanced spins are aligned due to the exchange energy. The boundaries between the magnetic domains are given by domain walls, where the magnetization is changing gradually. They have a width of about 20 atoms and represent a compromise between the magnetocrystalline and exchange energy terms. In the case of Bloch walls, the magnetization points out of plane. In 1955, Néel proposed an alternative domain wall where the magnetization is rotating inside the plane, no surface energy being present. The Néel walls are favored in thin films (34). It has been interestingly shown that the Néel walls are shrinking also by reducing the lateral size of the elements.

Magnetic coupling

Since the discovery of thin film technology, many improvements have been performed in understanding the special magnetic properties of these structures. Because the mean free path of the electron is higher than the thin film thickness, the magnetic phenomena that occur in thin films are different than the ones present in bulk systems. This is due to different couplings and interface effects that are dominant in thin film

structures. In the next paragraphs only the couplings effects that occurred in the systems studied throughout this work are presented.

Exchange coupling

The phenomenon of exchange coupling has been observed in 1956 by Meiklejohn and Bean, representing the magnetic interaction between a FM (ferromagnetic) spin system and an AFM (antiferromagnetic) spin system. It has been first noticed in FM Co particles embedded in their native AFM oxide CoO. Similar to other exchange interactions between ferromagnetic materials it has its origin in interface phenomena. In case of metallic thin film structures, the FM layer is deposited on the AFM layer. The system is annealed at a temperature T:

$$T_N < T < T_C \tag{1.3.3}$$

where T_N represents the Néel temperature of the antiferromagnet and T_C is the Curie temperature of the ferromagnet. During annealing, the system is immersed in a magnetic field and the FM spins align along the field direction, while the AFM has its spins randomly oriented. While cooling down the system through Néel temperature, due to the spin waves transmitted at the interface between the two different ferromagnetic materials, the AFM spins at the interface will orient along the same direction as the FM spins. When an external magnetic field is applied in the same direction as the annealing field, the FM, due to its much weaker anisotropy will tend to align with the magnetic field. But, as the AFM layer has a stronger anisotropy, it will exert a torque on the FM spins and force the FM spins not to align with the external field. So, the field needed to reverse the FM spins is larger than usual as there would be an internal exchange bias field due to the interaction between the FM and AFM layer.

A condition for the existence of exchange bias is:

$$K_{AFM} t_{AFM} \geq J_{int} \tag{1.3.4}$$

So, the anisotropy K_{AFM} and thickness t_{AFM} of the AFM layer should exceed the one of the FM layer, and their product is higher than the exchange at the interface, denoted by the interface coupling constant J_{int}. The exchange bias field H_E is proportional with the exchange field at the interface and inversely proportional with the thickness t_F and saturation magnetization M_S of the ferromagnetic layer:

$$H_E = -\frac{J_{int}}{M_S t_F} \tag{1.3.5}$$

The phenomenological features that can be observed due to the exchange bias are: a shift of the hysteresis curve due to the exchange field H_E, an increase of the coercitive field (that can be emphasized when the AFM anisotropy is weak, and then the FM will drag some AFM spins, thus increasing the hysteresis loop coercivity), sin θ torque curve and high field rotational hysteresis. Because the AFM spins will always torque the FM spins in the field cooling direction, the exchange bias anisotropy is unidirectional, also due to the sin θ dependence. All the effects associated with exchange bias vanish at the blocking temperature, T_B, which in case of magnetic thin layers is smaller than the Néel temperature, T_N of the antiferromagnet.

Exchange oscillatory coupling in magnetic multilayers

The oscillatory coupling occurs between two ferromagnetic layers separated by a very thin (10 Å) non-magnetic layer. Different ferromagnetic structures with various non-magnetic spacers have been intensively studied in order to characterize this phenomenon. The coupling is due to direct exchange between the d electrons of the ferromagnet through the electron gas of s electrons of the non-magnetic spacer (36). It has been experimentally proven that a strong antiferromagnetic coupling occurs in the CoFe/Ru/CoFe structure at a spacer of one atomic plane. Two models have been developed to describe the oscillatory coupling: the free electron theory and the tight bonding model. The free electron theory gives good approximation for the weak coupling limit and is based on the RKKY (Ruderman-Kittel-Kasuya-Yosida) theory (36). The tight bonding model includes the lattice structure in the calculation and points out the importance of the roughness between layers for the phenomenon explanation. This theory explains the long period oscillations that were inconsistent with the free electron model. The results of calculations with different spacing layers concluded that the oscillatory coupling strength depends mostly on the interlayer thickness than on the ferromagnetic thicknesses, so the main reason for this phenomenon are the interface scattering processes than the bulk processes (37), (38). The period of oscillation Λ has been calculated by considering the Fermi surface properties of the spacer layer and can be described by the following formulas:

$$\Lambda = \frac{\lambda_F}{2} = \frac{\pi}{k_F}, \text{ where } k_F = \frac{(12\pi^3)^{1/3}}{a} \tag{1.3.6}$$

is the Fermi wavevector. If we approximate the coupling strength J with

$$J \approx \frac{x\cos x - \sin x}{x^4} \xrightarrow{x\to\infty} \frac{1}{x^3}, \text{where } x = 2k_F d \quad (1.3.7)$$

It can be observed that in function of the spacer layer thickness a parallel or an antiparralel orientation of the two ferromagnetic layers can be obtained as shown in Fig. 1.5 (26).

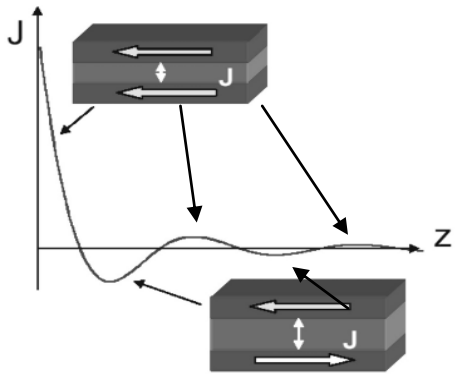

Fig. 1.5 Dependence of the spacer layer thickness of ferromagnetic or antiferromagnetic alignment of the ferromagnetic layers, as the coupling strength is J>0 or J<0 respectively. Taken from (26)

The interlayer exchange coupling energy is expressed in function of the interlayer exchange constant:

$$E(H) = A_{12}\cos\theta_{12} - M_s t_{FM} H(\cos\theta_1 + \cos\theta_2) \quad (1.3.8)$$

With:

A_{12}- interlayer exchange constant ; M_s- magnetization of FM layers

t_{FM} - thickness of each FM layer; θ_1- angle between the magnetization of one layer and the external field H

θ_{12}- angle between the magnetization of the two ferromagnetic layers; E(H) – exchange coupling energy

H – magnetic field;

In a parallel orientation of the ferromagnetic layers the exchange coupling constant is:

$$A_{12} = \frac{H_s M t_F}{2} \quad (1.3.9)$$

The interlayer exchange coupling energy can be described by a bilinear term J_{BL} and a biquadratic term J_{BQ}. If the case of biquadratic exchange interaction the two ferromagnetic layers are oriented perpendicular to each other.

$$E_{IEC} = -J_{BL}\cos(\theta_1 - \theta_2) - J_{BQ}\cos^2(\theta_1 - \theta_2) \quad (1.3.10)$$

The oscillatory coupling phenomenon leads to the discovery of the giant magnetoresistance effect, an effect present in the multilayers systems formed from magnetic and nonmagnetic materials. When the multilayer structure is situated in a changing magnetic field, a change in resistance with respect to the parallel or antiparallel orientation

of the ferromagnetic layers is observed. A. Fert and P. Grünberg received in 2007 the Nobel Prize for Physics for the discovery of the GMR effect in 1988 (39).

The oscillatory coupling phenomenon is used in spin valve and MTJ structures to emphasize the pinning effect of the bottom ferromagnetic layer, so the influences on the top soft layer are very weak.

Ferromagnetic (Néel or "orange peel") coupling

Néel magnetic coupling can be present in magnetic multilayer systems where two ferromagnetic layers are spaced by a non magnetic spacer (e.g. TMR structures). This type of dipolar coupling occurs due to the magnetostatic charges induced by the surface roughness. The Néel coupling is present in MTJ multilayers at the interface between the two ferromagnetic electrodes spaced by the insulator barrier. The ferromagnetic coupling decreases with increasing the insulator barrier thickness. The presence of pinholes in the barrier can lead to the observation of the same magnetic effects as the ferromagnetic coupling itself. It has been experimentally observed that the Néel coupling effect strength is increasing slightly by increasing the thickness of the pinned layer and decreases by increasing the thickness of the free layer. By ensuring a proper engineering of the ferromagnetic layers, it is possible to increase or decrease the ferromagnetic coupling in function of desired properties of the structures. Otherwise, a strong and unwanted orange peel coupling could lead to the destruction of the TMR element, a smaller sensitive field, a decrease of the TMR effect or even the presence of unstable magnetic states due to the torque exerted from the pinned ferromagnetic layer on the free ferromagnetic layer. In the construction of a sensor type element, it is necessary to have the top ferromagnetic layer as free layer in order to be sensitive to the local magnetic field change that has to be detected. Considering this, the bottom pinned layer must have a very small influence on the top layer, so the free layer thickness is usually increased.

Tunneling magnetoresistance

The process of tunneling has been modeled after the development of quantum mechanics, due to the association of the spin wave function to an electron (40). Even if in the classic mechanics the penetration of a thin insulator layer is forbidden, the quantum mechanics allows that thanks to the probability of tunneling of the electron wave function. The tunneling between metal-insulator-metal, metal-insulator semiconductor,

etc, has been studied since 1929, multiple models of tunneling being proposed since. The tunneling probability T through a barrier of height V and length l can be described by the following formula:

$$T \sim e^{-c\sqrt{\frac{2mV}{h^2}}l} \quad (1.3.11)$$

where c is a constant of order of unity, which depends on the detailed shape of the barrier and on the electron wavefunctions. The electron wavefunctions are crucial in tunneling process and become more important when the materials that are intercalating the barrier are ferromagnetic, resulting in spin dependent wavefunctions (41). The imbalance of the spin electrons at the Fermi level in a ferromagnetic material occurs because the density of states available for the spin-up and spin down electrons are similar but shifted in terms of energy one to each other. As a consequence to the shift, the bands will be filled unequally providing a net magnetic moment for the ferromagnetic materials. The spin-up and spin-down electrons at the Fermi level are unequal in number, character and mobility (42). Spin polarization can be expressed in terms of the number of carriers n that can have spin up (n↑) or spin down (n↓) as:

$$P = \frac{(n\uparrow - n\downarrow)}{(n\uparrow + n\downarrow)} \quad (1.3.12)$$

According to Stearns model, the transmission probability depends on the effective mass of the electrons, which is different for different bands. The localized d electrons have a larger effective mass and therefore decay very rapidly in the barrier region, but the dispersive s electrons decay slowly in the barrier. In the Stearn model, the s type electrons are the one that tunnel in a MTJ (magnetic tunnel junction). The calculations based on Stearn model of the polarization for different magnetic materials are consistent with experiments, providing 45% for Fe and 10% for Ni (43).

Considerable improvements have been done in understanding the tunneling process since the development of Julliere's model (44) of magnetic tunnel junctions in 1975. In the case of Julliere's model, the tunneling barrier is intercalated by two ferromagnetic materials. It was observed that the tunneling current depends on the relative orientation of magnetization of the two ferromagnetic electrodes on both sides of the barrier (43). Two basic assumptions constitute the base for the Julliere model:

1. The spin of electrons is conserved during tunneling, so the tunneling of spin up and spin down electrons are two independent processes. If the two ferromagnetic electrodes are parallel to each other, the minority spins from one feromagnet tunnels to the

minority spin states in the other ferromagnet, consequently for the majority spin electrons. If the two ferromagnetic electrodes are magnetized antiparallel to each other, then the identity of the majority (spin up) and minority (spin down) electrons is reversed, so the majority spins from one ferromagnetic electrode tunnel to the minority spin states in the other ferromagnetic electrode and vice versa.

2. The conductance for any state of spin orientation is proportional to the product of the effective tunneling density of states (DOS) of the two ferromagnetic electrodes.

Following the two assumptions of the Julliere's model of tunneling it can be defined the tunneling magnetoresistance ratio (TMR) as the conductance difference between the parallel and antiparallel magnetizations, normalized by the antiparallel conductance:

$$TMR \equiv \frac{G_P - G_{AP}}{G_{AP}} = \frac{R_{AP} - R_P}{R_P} \tag{1.3.13}$$

The spin dependent tunneling current can be calculated on the basis of Fermi's golden rule:

$$I = 2e\frac{2\pi}{\hbar} \int_{-\infty}^{+\infty} |T|^2 n_1(E - eU) n_2(E)[f(E - eU) - f(E)]dE \tag{1.3.14}$$

Where E is the energy with respect to the Fermi energy E_F, U the applied bias voltage, T, the tunneling probability, $n_{1,2}$ the density of states of the first and second electrode and $f(E)$ is the Fermi function with E referenced to the Fermi energy:

$$f(E) = \frac{1}{e^{\frac{E}{K_B T}} + 1} \tag{1.3.15}$$

The Slonczewski model includes the importance of the barrier properties in the spin dependent tunneling process along with the electronic states of the ferromagnetic electrodes.

A schematic representation of the tunneling processes in MTJ structures is represented in Fig. 1.6 where the dependence of the tunneling current values on the relative orientation of magnetization of both ferromagnetic layers is clearly shown. The tunneling effect is observed when a small bias voltage is applied across the stack and the entire stack is situated in a sweeping magnetic field. It has been observed that the TMR effect decreases with increasing the applied bias voltage, so usually small bias voltages are applied (5-10 mV). The breakdown of the barrier depends on its properties and usually appears at around 1-2 V.

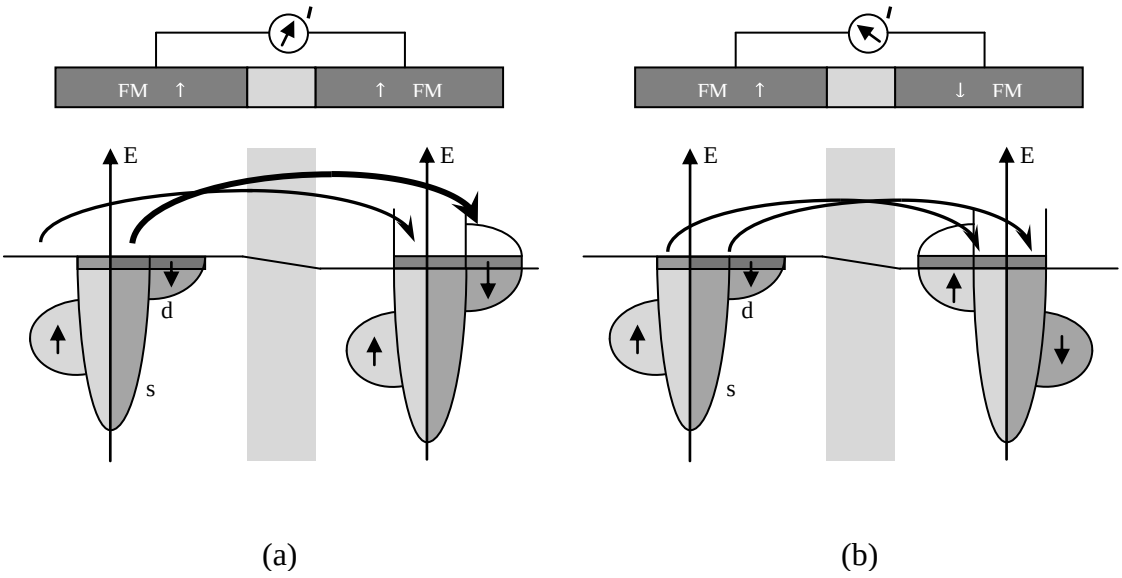

Fig 1.6 Characterization of tunneling process between two ferromagnetic layers separated by an insulator barrier. Remade after (26)

By improving Al_2O_3 barrier quality, Moodera et al were able to observe high TMR values at room temperature leading to a breakthrough in this research field. The magnetoresistance effect in the junctions with Al_2O_3 as insulator material show TMR values of up to 70% due to the amorphous nature of the barrier (45). During the last decade many advances have been achieved in this field direction. Magnetic tunneling junctions that involve MgO material as the insulator barrier between the two ferromagnetic electrodes are nowadays intensively studied. Huge TMR ratios (up to 6000%) have been predicted for Fe(100)/MgO(100)/Fe(100) epitaxial grown structures (46). Up to the present day, magnetoresistance ratios reaching the value of 1054% at room temperature (16) have been observed. The high TMR values are attributed to the crystalline tunneling barrier that has a (100) oriented structure even if it's intercalated between two amorphous electrodes. Also, it has been stated that a major contribution in the high TMR effect is given by the crystalline structures created by the ferromagnetic electrodes in the near vicinity of the barrier. The composition of the electrodes is important, being concluded that a high content of Co in the CoFeB electrodes will decrease the MR ratio (47). There are many other factors that can influence the TMR values, from which will be reminded the thickness of the MgO barrier, the annealing temperature, the electrodes composition, the sputtering conditions etc. All the groups that

reported high TMR values have a very low base pressure in the sputtering chamber, in the lower 10^{-9} mbar range. This factor decreases the probability of having impurities in the sputtering material, especially in the TMR cell that might influence negatively the tunneling phenomenon.

It has been predicted that the half metallic materials should present 100% spin polarization of the electrons at the Fermi level because of the presence of a band gap for the minority electrons. This should definitely lead to very high TMR values (48). Among half metallic alloys, the most promising appear to be the full Heusler alloys X_2YZ such as: Co_2FeSi, Co_2MnSi, Co_2FeAl. These alloys crystallize in the $L2_1$ structure. Using full Heusler alloys grown on MgO substrates as bottom electrodes and an Al_2O_3 barrier with top pinned CoFe electrodes, rather small TMR ratios has been obtained at RT such as: 51% for Co_2FeAl and 44% for Co_2FeSi (48). Further details regarding Heusler alloys will be presented in Chapter 3, because they were used as a top ferromagnetic electrode for the elements prepared for sensor applications.

As side effects there are many factors that might decrease the TMR values: formation of an oxide layer at the interface between Fe or FeCo and MgO. This would enforce an antiferromagnetic coupling between the monolayers that will influence the DOS of electrons. Also, there could be a spin-flip of the tunneling electrons due to the interaction with different charged particles, magnons or ferromagnetic impurities present in the barrier. By combining all these, efforts are done by the groups working in this area of interest to achieve the theoretical predicted TMR ratios. By reaching high TMR ratios, the applicability of the MTJ's structures in the sensors field increases because element's sensitivity is also enhanced.

Other future commercial applications of the MTJ field include their usage in HDD read heads and in MRAM devices. In 2004, Seagate Technology came into market with the first read head based on TiO_x MTJ technology. For commercial utilization, one of the most important requests consist in the low area resistance product (between 2-20 $\Omega\mu m^2$), that can be achieved by refinement of the construction process. Further development of magnetoresistive random access memory (MRAM) aims to the attainment of a new type of memory, that would be as fast as SRAM, but having the density of DRAM and the non-volatility of HDD (49).

2. Preparation and analytical tools

This chapter includes an overview of the instruments and methods that were used for the preparation and evaluation of the magnetic sensor devices. The entire process starts with the multilayer deposition, followed by elements patterning using e-beam lithography and ion beam etching methods. Afterwards, the electro-magnetic transport through the tunneling magneto-resistance devices is measured.

2.1 Thin film sputtering

The latest developments in thin film technology conduce to additional advances in information technology. The application of thin films compounds in computer and other sensitive technologies is and will be of further interest. Because of the fact that thin films thickness ranges from a few angstroms to a few nanometers, the interface effects are dominant. The atoms present in thin films have mostly interface sites, so they exhibit a different behavior compared with the atoms present in bulk systems. This gave rise to a new branch of physics, where processes at the nanoscale regime had to be modeled. The new models must take into account that the mean free path of the electrons in solids is in the same range as the thickness of the thin film. Regarding this, the electrical, thermal and transport properties of thin films cannot be explained by classical means and the introduction of quantum theory models is mandatory.

Thin film sputtering is known since 1842 (50) and is based on vacuum technology. When the target material that will be eroded is situated at the cathode side (-) and the substrate at the anode side (+) and a potential in the range of several hundred volts is applied between the plates, a plasma ignition occurs for pressures in the 10^{-3} mbar range by scattering effects of background events. The accelerated ions will subtract material from the

target and deposit as neutral atoms on the substrate (51). Magnetron sputtering is widely used because the magnitude of the current is higher with the voltage maintained at low values, so the sputtering rate is increased. The power applied on the target depends on the target size. In case of the used systems, for small size metal targets of 42 mm in diameter a power of 25 W is applied for DC sputtering, while larger targets of 101 mm in diameter require a power of 115 W for DC sputtering. For the deposition of insulator materials (TaO_x) the RF reactive sputtering from metallic targets in the presence of a reactive gas (O_2) mixed with an inert gas (Ar) is used (52). All samples are sputtered at room temperature.

The sample stacks used for this work have been sputtered in Leybold "CLAB 600 Clustertool" (53). The machine has the possibility of automatic magnetron sputtering with six 4″ targets and two 2″ targets. Five of the 4″ targets are used for DC sputtering (at a power of 115 W) two of them having special construction characteristics for ferromagnetic targets. The insulator barrier is sputtered by using a Hüttinger RF generator (13.56 MHz) and an MgO target (54). The base pressure of the sputtering system is $1 \cdot 10^{-7}$mbar. The pressure of the sputter gas is controlled by two parameters such as: Ar flow for achieving the sputter pressure in the range of 10^{-3} mbar and the throttle position (valve that is controlling the flow by obstruction or constriction). In order to achieve reproducible sputtered elements stacks it is important to have a good control over the Ar flow and throttle position. For the DC sputtering of metallic elements an Ar flow of 20 sscm is used and a throttle position of 21%. During the RF sputtering of MgO barrier, the Ar flow stays 20 sscm but the throttle position is 3%. The optimizations of sputtering parameters for a good quality tunneling barrier have been realized by A. Thomas and V. Drewello in their doctoral and diploma work (55), (56).

During the patterning of magnetic tunnel junction elements, an additional sputtering machine prepared at Bielefeld University is used for the deposition of TaO_x as insulator layer and for Ta and Au layers. For the deposition of TaO_x, the partial oxygen pressure used is $2 \cdot 10^{-4}$ mbar and Ar flow is adjusted to reach a pressure of $3.5 \cdot 10^{-3}$ mbar. TaO_x insulator material is RF sputtered at a power of 50 W. For the sputtering of oxide materials it is

important to have a proper control of the partial oxygen pressure, because negative oxide ions can be formed and will re-sputter from the film (51). By increasing the oxygen partial pressure from $1.5 \cdot 10^{-4}$ mbar to $3.5 \cdot 10^{-4}$ mbar it is observed that the sputter rate of TaO_x is reduced by 28%. The Ta and Au materials are magnetron sputtered at a power of 25 W in the same machine.

The thin films have been deposited on a Si wafer, with 50 nm thermally oxidized SiO_2 on top having an entire thickness of 525 μm. The wafer has a (100) orientation (57).

2.2 Vacuum annealing

The vacuum annealing process is used in order to realize the exchange bias between the ferromagnetic and antiferromagnetic thin film layers and is based on a vacuum furnace, where the samples are annealed at temperatures comprised between the Curie temperature of the ferromagnet and Néel temperature of the antiferromagnet. The base pressure of the vacuum furnace is $1 \cdot 10^{-7}$mbar. During annealing a strong magnetic field of 6500 Oe is applied which is provided by a permanent magnet, to define the magnetic order of the ferromagnetic layer. Afterwards, the sample is field cooled through the Néel temperature of the antiferromagnetic layer at room temperature.

For the samples used in the work presented in this thesis, the annealing has been done at 350°C for one hour in the presence of a hard magnetic field (which will give the orientation of magnetization of the hard axis of the elements). The field cooling has been realized for 30 minutes. The vacuum annealing is also done to obtain a crystalline structure of the MgO barrier in order to achieve the conditions required for coherent tunneling.

2.3 MOKE measurements

The magneto-optic Kerr effect (discovered in 1877 by John Kerr) is based on the detection of changes produced in the optical properties of a reflected beam by a magnetized ferromagnetic layer (51). After the annealing processes the magneto-optic Kerr effect

of the samples has been analyzed to visualize the pinning effect on the hard bottom ferromagnetic layer and the softness of the top detection layer. In order to observe the magneto-optic response of thin films is required for them to have a thickness of less than 20 nm.

2.4 Lithography processes

The scanning electron microscope (SEM) used for the present work is a LEO 1530 Gemini system (58), with acceleration voltage comprised between 0.2-30 kV. The electron beam can be produced by thermionic field effect emission and due to its property of being easily manipulated by electric and magnetic fields it can be focused on a spot size of only a few nanometers.

The SEM is used for visualizing the prepared samples due the scanned (deflected) coil present in the optics of the microscope and it has a nominal resolution is of 1.5 nm for 20 kV. The SEM has an integrated lithography system from Raith Elphy Plus (59). The lithography process is realized by using resists (polymers that react in contact with an electromagnetic wave or e-beam). The resist can be of positive (the exposed areas of resist will be dissolved in the developer solution) or of negative (the exposed areas stay after developing the sample) type. A comprehensive table with the solutions used in the lithography process can be found in Table 2.1.

For sensor applications it is important to have elements of small size that can be patterned only by e-beam lithography. The reason lies in the necessity of having single domain structures with a small distance between them. For the further biological suitability of the elements it is needed to comprise the elements in a closed packed array. Optical lithography (parallel UV or laser lithography) provides minimum achievable structures of 1.2 μm. The resolution in optical lithography is limited due to the reflection of the electromagnetic wave (51). The lateral size of the structures patterned by e-beam lithography is limited by the resist thickness and the proximity effect of the secondary electrons. By using diluted negative resist, the lateral resolution of the structured elements can reach 50 nm.

The positive e-beam resist has a much reduced thickness (see Table 2.1), so the patterned structures can have sizes of less than 20 nm.

Table 2.1 Procedures and solutions used in the e-beam lithographic processes

	Positive e-beam lithography	Negative e-beam lithography
Resist type	PMMA 610.03 **Allresist** (60)	AR-N 7520.18 from **Allresist** (60)
Coating	4000 rpm - 140 nm 6000 rpm - 120 nm	4000 rpm for 30 s - 400 nm 6000 rpm for 30 s - 350 nm
Baking	15 min at 150°C	2 min at 85°C
Developing	AR 600-55 from **Allresist** (60) for 2 min Stopper AR 600-60 from **Allresist** (60) for 30 s	AR 3000-47 from **Allresist** (60)for 5-9 min Rinse with DI water for 30 s
Removing	AR 300-70 **Allresist** (60)for 5 minutes in an ultrasonic bath at room temperature Rinse with ethanol afterwards	1-Methyl-2-pyrrolidinone,Chromasolv Plus from **Aldrich** (61) for 30-60 min in an ultrasonic bath at a temperature between 60-80°C Rinse with ethanol afterwards

2.5 Ion beam milling

The etching process is based on removing material from the substrate by physical or chemical means. For the prepared samples, physical etching is used in combination with negative e-beam resist for the patterning process. The incident ions (Ar^+) are accelerated into the surface where they remove the material that is not covered by resist. The removed particles can be neutral or charged. The charged particles pass through an energy filter and are analyzed by a mass spectrometer that is attached to the etching chamber. From the analyzed particles, the material that is eroded is known precisely. This feature is very helpful when an accurate etching stopping point is necessary.

2.6 Magneto-transport detection

The measurement of the tunneling process is done with a 2 probe technique. For the tunneling current measurement, a voltage of 10 mV is applied. The reason for choosing this value is because it is comprised in the linear range of a tunneling device IV curve and the tunneling magneto-resistance ratio is kept at elevated values. The tunneling current is measured with an electrometer at different amplifier settings. The output of the electrometer is measured by a Keithley Model 2000 digital multimeter. The value of the measured current is comprised between 1.2 to 28 nA. For in plane measurements, a magnetic field is applied through coils with iron core that produce a magnetic field of ± 3000 Oe (56). The magnetic field is measured at the sample position with a Bell Tesla meter. For out-of-plane and angle field measurements Helmholtz coils without an iron core are used, so the produced magnetic field is smaller (±200 Oe).

3. Description of TMR sensors

This chapter includes a characterization of the standard stack used for sensor development, the preparation methods employed to obtain the elements, the effect of the shape anisotropy on the elements output and sensitivity. An overview regarding different thin films stacks used to obtain a linear output will also be presented. The aim of the overview is to emphasize the importance of the proper construction for a sensing element. The necessity of having a hard pinned bottom electrode and a soft top magnetic layer of the element for sensor applications is revealed. Additionally, a short characterization of the noise present in submicron tunneling magnetoresistance structures will also be included.

3.1 Preparation of TMR elements

One of the main advantages of TMR sensors is revealed by their current perpendicular to plane geometry. Owe to this property, the lateral dimension of the sensors can be reduced, and consequently the distance between two sensors can be very small. The possibility to construct a closed-packet array with elements of reduced dimensions is accomplished by the electron-beam lithography technique. An MTJ element can be used as a sensor if it fulfills the following conditions: single domain structure, linear output behavior and high sensitivity over a large magnetic field range. As shown before (Chapter 1.2), if a magnetic structure has a dimension of less than 500 nm, the internal magnetic energy is too low to form magnetic domains, so the structure will be monodomain. The energy will be expensed in the form of an external magnetic stray field. The linear output can be forced to an element by having an orthogonal orientation of the two magnetic layers that intercalate the oxide barrier. The methods that have been used to accomplish this will be presented in detail in the next subchapter. The sensitivity is expressed by dividing the magne-

toresistance ratio by the magnetic field range where the sensors exhibit a linear behavior. As the MTJ elements have a higher magnetoresistance ratio compared to the giant magnetoresistance elements, it is expected to have also an increased sensitivity.

For the appliance of TMR sensors in the field of molecular biology is desirable that they have a size in the same range as the magnetic markers that have to be detected, which also should have similar dimensions with the biomolecules they are attached to. In order to have a multiplex analysis of biomolecules, for biosensing application the distance between sensors should be as reduced as possible. All the above conditions are accomplished by the sensor array that has been designed for e-beam lithography processes. The distance between two adjacent sensors is 1.2 μm, one sensor having an elliptical size with 100nm×400nm. By employing e-beam lithography procedure 20 sensors are patterned in an area of 18.2 μm^2.

The construction of the TMR sensors is based on a chain of e-beam lithography, ion beam etching, removing and coating techniques. The entire patterning process of TMR elements is based on three main steps. A short graphic description of these steps with their corresponding procedures is given in Fig. 3.1- Fig. 3.3. In the first step, the bottom contact is exposed to e-beam, together with the crosses for orientation that will be needed in the next lithography processes due to the matching requirements of the entire lithographic steps. The next procedures of the first step consist in the ion beam etching and removing the resist from the patterned lithographic systems. After these processes, the entire MTJ stack is present only in the structures that have been exposed. An important requirement for the first etching stopping point is that it should be set at precise point, considering that in the second etching stopping point to have reached the SiO_2 layer in the outside part of the non-patterned film and Ta layer in the space between the elements.

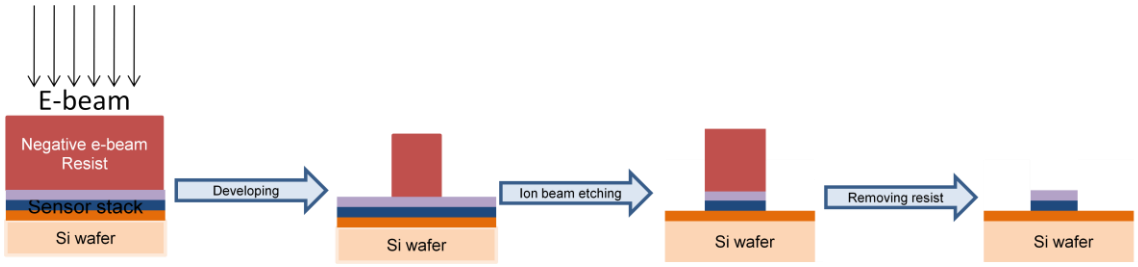

Fig.3.1. Transversal view of the first lithography step and its adjacent process

In the second patterning step, the TMR elements and the bottom contacts will be exposed to e-beam resist. The bottom contacts have to be shortcut because in magneto transport measurements, a voltage will be applied through the stack. The voltage drop is between the bottom contact and the element contact in order to have a current flow perpendicular to the plane of the element. Due to the precision requirements, the orientation of the sample is done with the help of the crosses that have been exposed in the first lithography step. The developing time is chosen to be higher after the second lithographic process in order to achieve the desired dimension of the elements. Due to the resist properties, the reached size of the elements is always higher than the nominal value. Also, because of the reduced size of the elements, the dose that has to be applied during lithography is higher than the dose required for structures in the micrometer range. It is mandatory to perform a dose test for the elements in order reach the appropriate size and to ensure the patterning reproducibility if the same conditions are kept. If for the exposure of structures with a size larger than 1 μm a dose factor of 1.3 is required for a resist sensitivity of 170 μAs/cm^2, at the structuring of 100 nm×400 nm elements, a dose factor of 2.6 is needed for the same value of the resist sensitivity. In these conditions, the real size of the elements is increased with around 25% related to the nominal size. Obtaining structures with reduced dimension on the lateral size is one of the most challenging tasks in the e-beam lithographic procedures. In all the work done throughout this thesis, the smallest achievable lateral size was of 80 nm with the negative resist (by using a working distance in the SEM chamber of 20 mm). The working distance is referred to the distance between the final lenses and the sample. If this distance is larger, the cone of electrons is narrower and the

field depth is increased. The second lithographic step is followed by a second ion beam etching procedure. This is recommended to be done at a position tilted with 30° to the ion beam in order to avoid redeposition of the removed material that would shortcut the sample. The stopping etching point for this step is determined by the necessity of having Ta material between the elements so that the further deposition of TaO_x insulator layer to be possible. The thickness of the insulator sputtered between the elements has to be large enough to ensure the electrical isolation of the elements and small enough to facilitate the further lift-off process. It has been observed during the preparation processes of the submicrometer elements that when the thickness of the resist was around 200 nm, because of the diluted resist with thinner, the lift off process , removing the resist with a layer of TaO_x on top, required too long time (more than 90 minutes). This is disadvantageous to the element because long ultrasonication process can lead to the element destruction. A thickness of 50-60 nm of TaO_x proved to be a good electrical insulator and the lift off process time for a non-diluted resist is around 30 to 40 minutes. After finalization of this step, the only part of the wafer that contains the entire TMR stack is in the region where the elements are present.

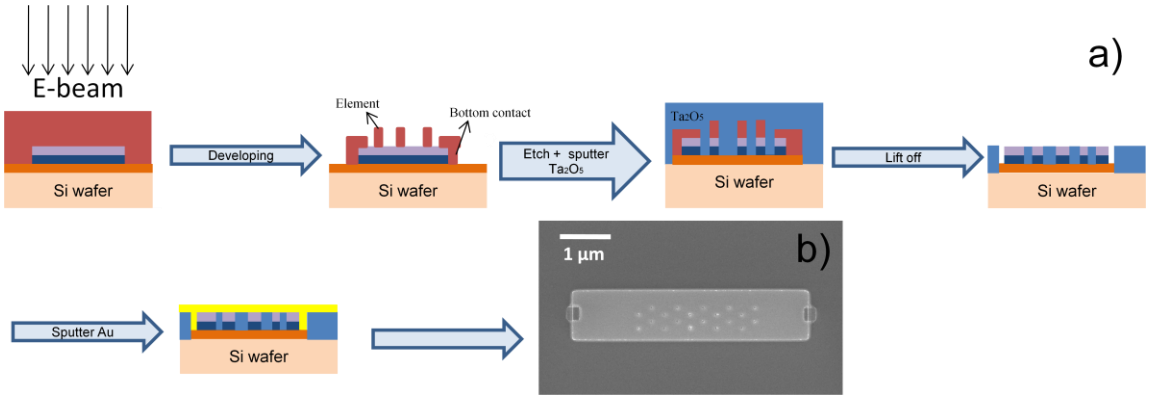

Fig. 3.2 (a) Transversal view of the second lithography step and its adjacent processes and (b) an SEM picture of the TMR elements after the Ta_2O_5 lift off procedure

The last procedure of the second step of patterning is sputtering of Ta and Au layers for the conduction lines that will be put on top of the sensors in order to contact them for the measurements. The total thickness of this layer is 55 nm. A compromise has to be done in choosing the thickness of this layer, because a thick layer would increase the distance between the sensing layer from the sensor and the magnetic marker that has to influence the sensor, while a small thickness would lead to a high total measured resistance of the element that is expressed in an increased noise.

The last lithographic step for the finalization of the sensor array consists of exposing to e-beam the conducting lines that has to contact the elements in order to be measured. This is again followed by an ion beam etching procedure, where caution must be taken to stop in the TaO_x layer in order to have an insulation material between the conducting lines. The next step is the resist removal situated on top of the patterned lines (negative e-beam resist). After this final stage the sample is ready to be measured and characterized. The magneto resistance curve of the sensors is determined from the measurements by applying a voltage of 10 mV and collecting through the amplifier the tunneling current.

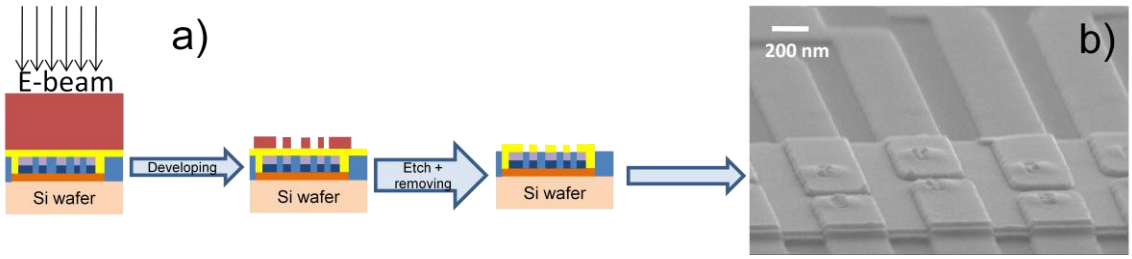

Fig. 3.3 (a) Transversal view of the third lithography step and its adjacent processes and (b) SEM image of the elements after being contacted with the top conducting lines

In many cases further manipulation lines that have to be situated on top of the sensors are required. The purpose of the manipulating lines is to control the movement of the magnetic markers on top of the sensor area. Their construction necessitates additional lithographic steps. Firstly, a lithography process is used to protect the sensor's contact pads and to preserve the sensors for further electrical measurements. Afterwards, a layer

of TaO_x is sputtered to ensure that sensors will not be directly contacted with the upper lines. The purpose of the insulator is to avoid any electrical contact between the conducting lines that are contacting the sensors and the manipulation lines on top. Usually a thickness between 100 and 200 nm of TaO_x satisfies these requirements. Another important issue that has to be considered is related to the capacitive effects that occur between the two conducting lines separated by the insulator. This can be avoided by having an as small as possible overlap between the lines that are covering the sensors and the top manipulation lines. Because the area where the sensors are situated is reduced, the manipulation lines are used to attract the magnetic beads exactly on top of the sensors. The current that passes through the lines will give rise to a high enough magnetic field to attract the magnetic markers situated at a certain distance from the line. The top manipulating lines have also the purpose of guiding the magnetic markers during dynamic measurements. The design of the lines is chosen with regards to their purposes. Further details regarding the manipulation lines are presented in Chapter 4.

The achievement of the standard sensor array encountered a series of problems on its path and some of them will be presented further. Due to the small size of the sensors, one challenge is related to the elements patterning. Many tests have been done in order to achieve the elements with a size of 100 nm×400 nm. The changing parameters in the lithographic processes were the working distance and the dose that has been applied during exposure. With an SEM working distance of 20 mm and a dose factor of 2.6 at the resist sensitivity of 170 $\mu As/cm^2$ it was possible to achieve a lateral size of the elements of 80 nm with pure resist. It is advisable to use undiluted resist in the elements preparation because the lift off after the TaO_x sputtering works faster and the elements are not kept under ultrasonic stress for long time. By these means, the elements will be more robust, yielding a functionality range between 80% and 100%. Because the distance between the elements is very small, another major challenging task is the achievement of proper top contacting conducting lines. The orientation of the sample for the third lithography step had to be in concordance with the other two lithography steps done before. This could be achieved by having multiple helping structures for a good accuracy in orientation. It must be kept in

mind that the resist properties are changing in time, and this feature has to be taken into account when small structures with high resolution are desired. Due to the construction of the additional manipulating lines on top of the sensors it is possible to have some defects in the TaO_x insulator layer. Attention must be taken in this case because the appeared imperfections can lead to the destruction of the sensors during electrical measurements. Even if TaO_x present perfect insulation properties (62) and has been proven that can be used as coating material against corrosive processes (63), it seems that the deposition conditions play an important role on insulator properties. It might be possible that by changing the sputtering parameters (e.g. oxygen pressure, argon pressure), the properties of the insulator layer could change and lead to unwanted situations as the one presented in Fig. 3.4 c. In this case, the insulator can be penetrated by water and the isolation is not ensured any more.

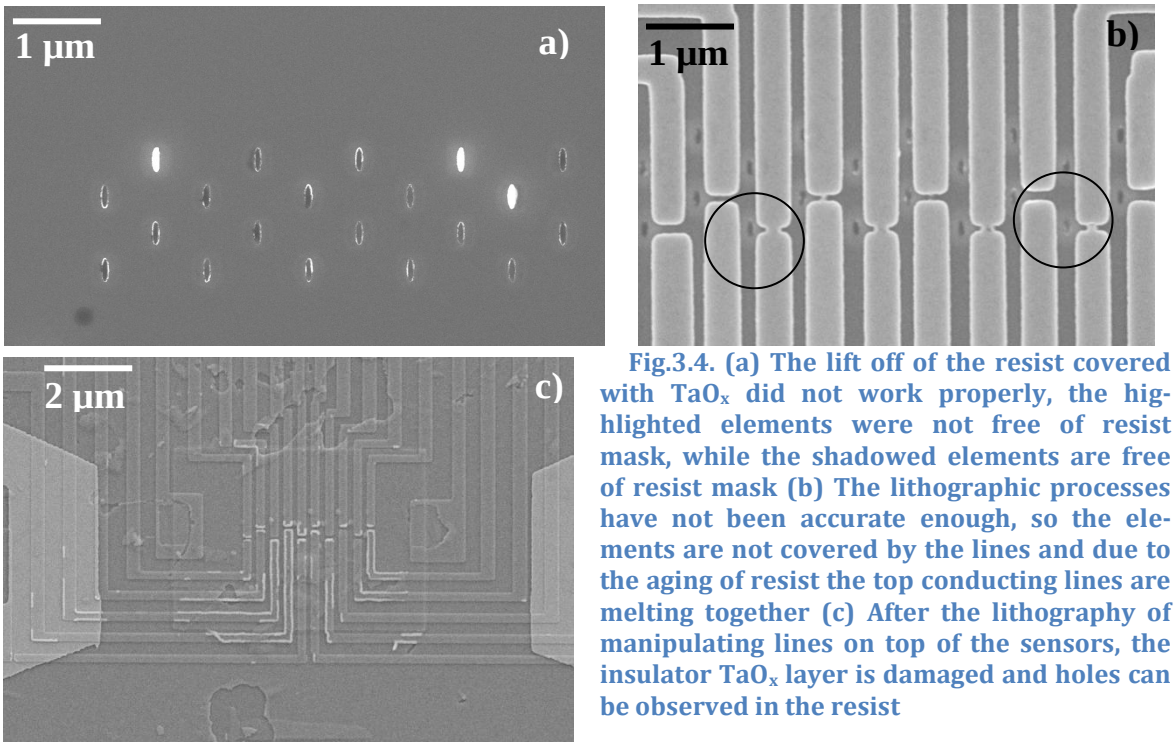

Fig.3.4. (a) The lift off of the resist covered with TaO_x did not work properly, the highlighted elements were not free of resist mask, while the shadowed elements are free of resist mask (b) The lithographic processes have not been accurate enough, so the elements are not covered by the lines and due to the aging of resist the top conducting lines are melting together (c) After the lithography of manipulating lines on top of the sensors, the insulator TaO_x layer is damaged and holes can be observed in the resist

3.2 From a TMR element to a TMR sensor

In order to use a TMR element for biosensing applications it is important to have a linear output of the tunneling magnetoresistance measurements. Because of linearization, comparison can be done between the measurements done with and without magnetic markers on top of the element area and the detection of magnetic markers can be confirmed. Sensor's linearity can be obtained if the two ferromagnetic layers that are intercalating the tunneling barrier have an orthogonal orientation of magnetization in a zero magnetic field (18). This can be achieved by setting the hard axis of the element in the direction of the cooling field. The bottom ferromagnetic layer consists of an artificial antiferromagnet (AAF) and is pinned by exchange bias to an antiferomagnetic layer (MnIr). The AAF (CoFe/Ru/CoFeB) is chosen to be used owe to the strong coupling that exists between the two ferromagnetic layers. The antiferromagnetic coupling between Co/Ru/Co is the strongest one known up to date (38). In this case the first layer of the bottom ferromagnetic electrode is CoFe, because it has a high coercitive field (is a stronger ferromagnet than the CoFeB) and the pinning with the antiferromagnetic layer will be stronger. The reason for this configuration of the bottom ferromagnetic electrode lays in the necessity of having a hard pinned layer that will not switch when an external magnetic field is applied. Therefore, only the top ferromagnetic layer is rotating when an external magnetic field is applied. The MgO barrier is intercalated between two CoFeB ferromagnetic layers because in this configuration high values of magnetoresistance ratio have been measured. This has been proved to be due to the partially crystallization of the CoFeB electrode that allows a coherent tunneling through the crystalline MgO barrier. The CoFeB ferromagnetic layer situated on the upper side of the barrier has an increased thickness compared to the thickness of the CoFeB situated below the barrier. This provides a softer top ferromagnetic electrode that should switch its orientation of magnetization at a very low value of an external magnetic field. The magnetization orientation of the top electrode will take the direction of the easy axis of the elliptical element. It has been shown in Chapter 1.3.1 that the shape

anisotropy constant is higher by a few orders of magnitude than the magnetocrystalline anisotropy constant. Because the element size is less than 500 nm (in order to avoid the formation of the magnetic domains), the shape anisotropy is defining the orientation magnetization of the top ferromagnetic layer (64). In order to achieve magnetic markers detection it is important to have the sensor size in the same dimension range with the magnetic marker. For the application of magnetic sensors in molecular biology, the size of magnetic markers has to be comparable with the size of the biomolecules. For biological applications of magnetic sensors based on magnetoresistance effect, the sensors dimension has to be minimized with respect to the e-beam lithography limits. Because only negative e-beam resist can be use for patterning of TMR elements, the lateral achievable limit with the used system is situated in the 60 – 100 nm range.

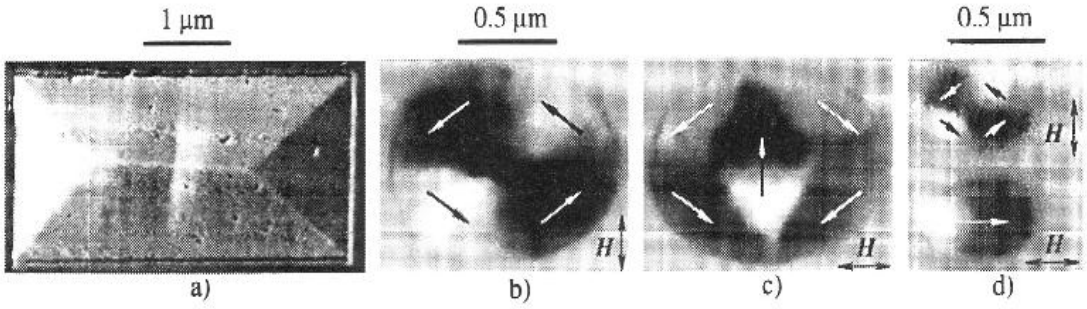

Fig. 3.5. (a) Rectangular shaped soft magnetic element. (b)–(d) Elliptical Co elements. The larger element shows either (b) a concentric state or (c) a three domain state. (d) The concentric state can also be observed in the smaller element after applying a field along the shorter axis. Otherwise a single domain state is observed which can be recognized by its black and white contrast. (Reprinted from (65)**)**

The bottom ferromagnetic electrode will have the orientation of magnetization given by the cooling field due to the strong pinning. The top ferromagnetic electrode has the magnetization oriented along the easy (long) axis of the elliptical element due to shape anisotropy. By patterning the elliptical element with the short axis along the pinning direction, the two ferromagnetic electrodes will exhibit an orthogonal orientation of magnetizations. This effect is illustrated in Fig. 3.6.

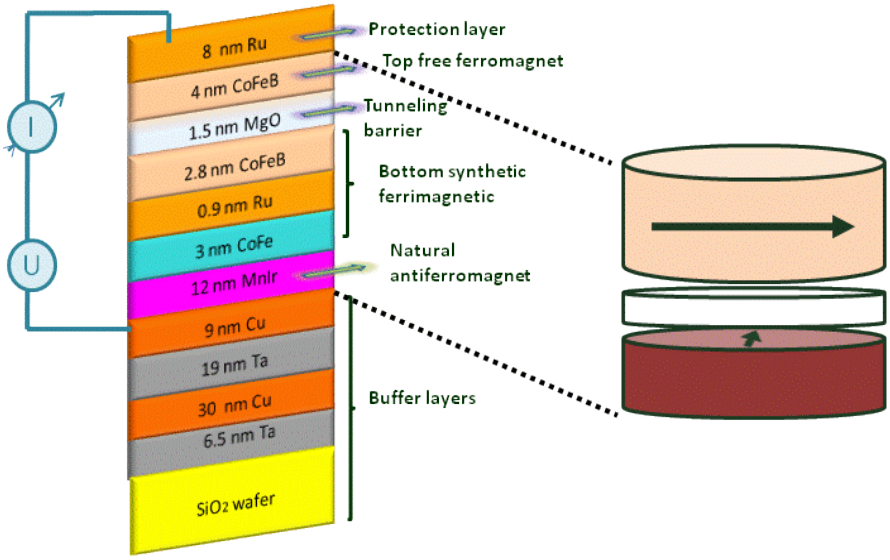

Fig.3.6 Characterization of the standard stack used for biosensing application with an emphasize on the tunneling magnetoresistance cell

3.3 Characterization of the sensor elements

In the following subchapter a characterization of the MTJ elements is required in order to emphasize their suitability for magnetic field sensing. Firstly, a comparison between the TMR outputs when the element is having the orientation of the two ferromagnetic electrodes in a parallel or orthogonal configuration is done. The influence of different aspect ratios of the element on the sensor's output and the sensitivity reached in each case has been tested. After determining all the properties, the best aspect ratio, where the element has an increased sensitivity and the magnetic field linearity range is large was chosen. A large linearity range is required when a large magnetic field to magnetize the magnetic labels. The output of a tunneling element with the orientation of the easy axis of the elliptical element is parallel to the magnetic cooling field used for the exchange bias processes is illustrated in Fig. 3.7a. In this case, see Fig. 3.7 a, the top ferromagnetic electrode is switching fast, so it's not possible to achieve a linear behavior, but a large value of the

TMR ratio is obtained. When the two ferromagnetic electrodes have an orthogonal orientation, a linear output of TMR sensor is achievable, because the top layer is rotating along the external applied field. The TMR variation follows a $\cos\theta$ dependence, where θ is the angle between the two FM electrodes. As θ approaches the $\frac{\pi}{2}$ value in the orthogonal orientation of the FM electrodes, it is expected to have also a reduced TMR value in comparison with the parallel orientation.

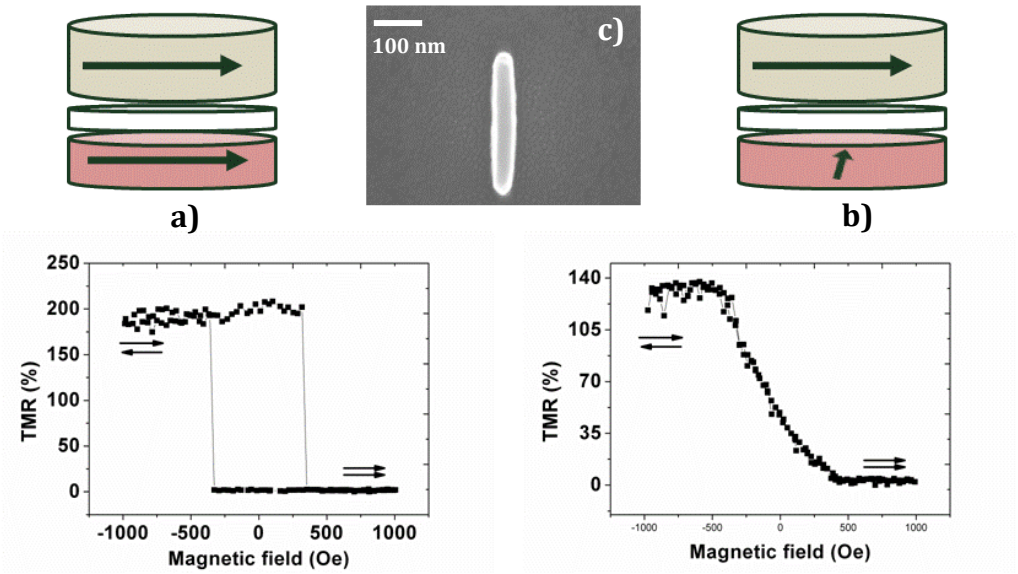

Fig. 3.7 (a) Element behavior when the two ferromagnetic electrodes are in parallel orientation (b) Sensor's output when the two ferromagnetic electrodes have an orthogonal orientation (c) SEM image of a single sensor element

The linearity range depends on the aspect ratio of the element. If the element has an aspect ratio of 1/3 the linearity range is reduced, but the sensitivity is increased. Different aspect ratios have been investigated to show their importance on the sensor's behavior. In all cases, the elements have a lateral dimension of 100 nm and the dimension of the longitudinal axis varies from 300 nm to 500 nm.

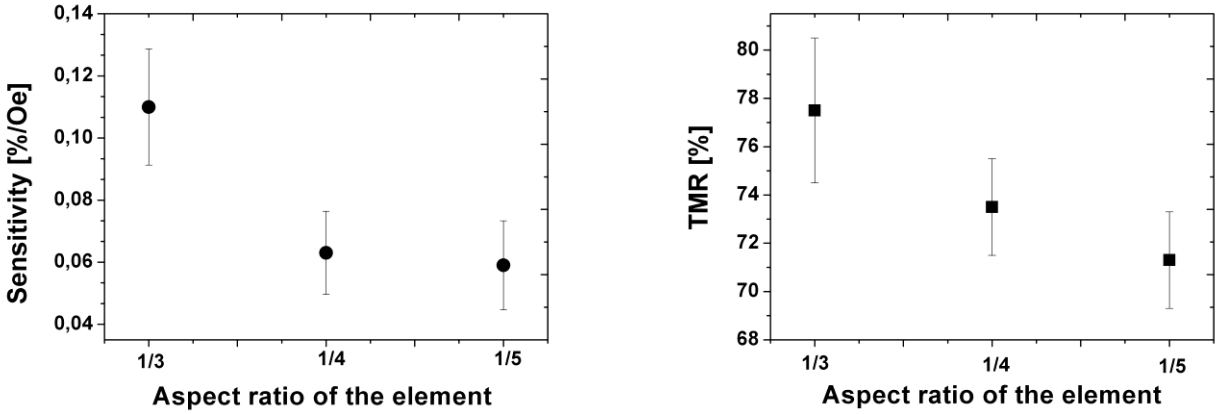

Fig.3.8. (a) Mean sensitivity variation with the aspect ratio of the element (b) Mean TMR variation in the linear range in arrays of sensors with different aspect ratios

The sensitivity is calculated by dividing the TMR ratio by the field range within the range of linear behavior. The elements with an aspect ratio of 1/3 have an increased TMR due to their small size and to their reduced magnetic field linearity range of only 300 Oe (see Fig 3.8a). By considering these properties it can be seen that they also exhibit an increased sensitivity. As the aspect ratio of the element is increasing, the TMR decreases, but the linearity is extended to higher magnetic field ranges. This is related to increasing the shape anisotropy. For sensor elements patterning, an aspect ratio of 1/4 has been chosen. The advantage lays in an increased sensitivity of detection while applying an increased value of magnetic field in order to magnetize the magnetic marker. It is important to reach a compromise between the magnetic field that can be applied on the magnetic bead and the sensor's sensitivity. By knowing this, different aspect ratios can be used as a function of the detection requirements.

Sensitivity values of up to 10%/Oe have predicted for TMR sensors (66) but due to their large range of magnetic field linearity, the predicted values have not been achieved. An advantageous factor for the sensors presented is the high value of the magnetic field that can be applied on the magnetic marker. So, the magnetic stray field exhibited by the magnetic bead or nanoparticle will be also high.

3.4 Overview of the stacks employed in sensors linearization

This subchapter will include a brief characterization of different stacks with various layer composition used to improve the sensor's quality. One essential characteristic of the standard stack used for sensor's patterning is the hard pinned bottom ferromagnetic layer. The bottom ferromagnetic layer should not switch even if large magnetic fields are applied. By using an artificial antiferromagnet as a bottom electrode, two ferromagnetic layers with Co magnetic material spaced by a 0.9 nm Ru layer, the pinning phenomenon is enhanced due to strong exchange coupling ($J = 5\ mJm^{-2}$) between the two ferromagnetic layers. To achieve a hard bottom electrode it should be considered that the lower ferromagnetic layer as part of the bottom electrode should have an increased coercivity compared to the upper ferromagnetic layer of the bottom electrode. For this reason the CoFe/Ru/CoFeB combination is chosen for the bottom electrode configuration. By inserting additional B to the CoFe alloy it becomes softer (67). The pinning is more effective when the ferromagnetic layer is positioned at the interface to an antiferromagnetic layer to improve its magnetic stiffness. The combination of CoFeB/Ru/CoFeB for the bottom ferromagnetic electrode instead of CoFe/Ru/CoFeB would lead to a weak pinning and the resulting output behavior of the sensor would not have been linear. Information regarding the pinning of bottom ferromagnetic electrode can be provided from MOKE measurements done after the sample field annealing as is shown in Fig 3.9. Another important issue is the difference of thickness between the two ferromagnetic layers that are separated by the MgO barrier. In order to use the stack for biosensor application the top ferromagnetic layer has to be softer than the bottom ferromagnetic layer. So, the bottom ferromagnetic layer has to be thinner than the top ferromagnetic layer. If the two ferromagnetic layers have the same thickness (2.5 nm) the output behavior of the element will not be linear. This is due to the stronger Néel coupling between the two ferromagnetic electrodes. In this case, both electrodes will switch when a magnetic field is applied, as is illustrated in Fig. 3.10 a.

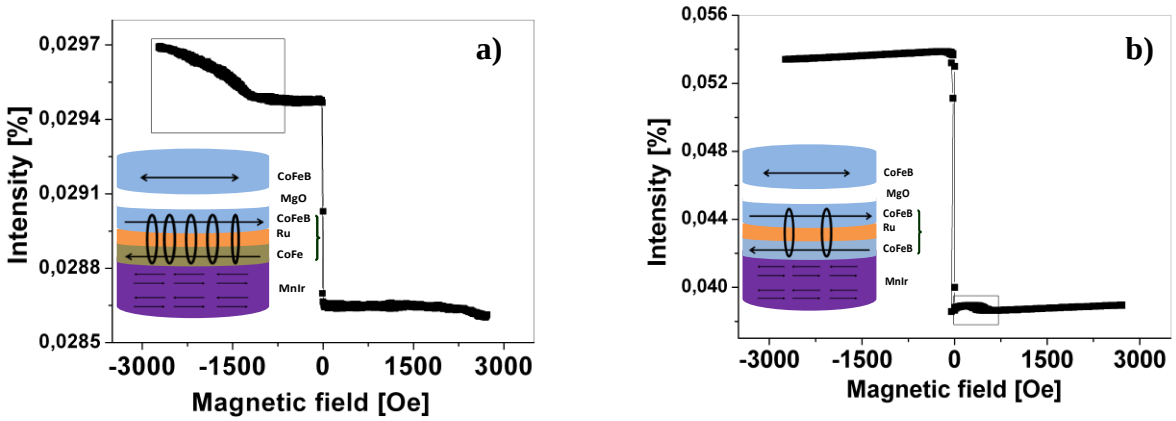

Fig. 3.9 (a) MOKE measurement of the standard stack, it can be seen in the inlet how the bottom ferromagnetic layer (that is the upper part of CoFe/Ru/CoFeB) is switching at a field higher than 1000 Oe (b) MOKE measurement for a stack that has the bottom ferromagnetic electrode formed from CoFeB/Ru/CoFeB, where it is observed in the inlet that the bottom ferromagnetic layer is switching at a field lower than 500 Oe due to its weak pinning

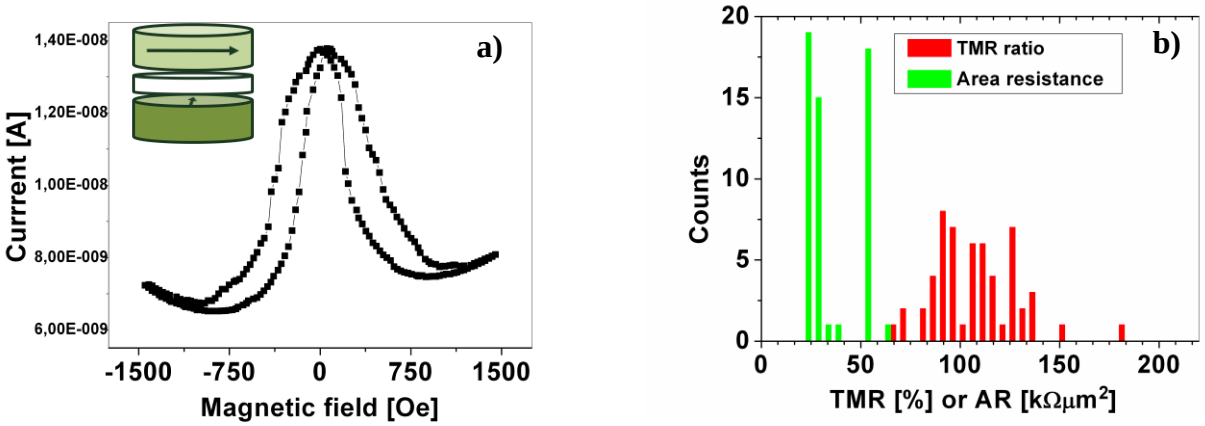

Fig 3.10. (a) TMR measurements of a layer stack with the following composition, with thickness in the brackets given in nm:Ta(10)/Ru(30)/Ta(5)/Ru(5)/MnIr(10)/CoFe(6)/Ru(0.88) /*CoFeB(2.5)*/MgO(1.8)/*CoFeB(2.5)*/Ta(5)/Ru(30) (b) Statistic TMR and area resistance data regarding the previous stack with measurements done within 3 arrays of 20 sensors each

Figure 3.10 b reveals the variation of the TMR ratio and of the area resistance within 3 different arrays of sensors. It can be observed that due to the small size of the elements, the variation of the area resistance is large even if the sensors are situated very close to each other. In order to get more insights regarding the magnetic behavior of different layer stack composition, the behavior of a stack with bottom CoFeB (2.2 nm) and the top CoFeB ferromagnetic electrode (3 nm) has been investigated. As it can be observed from the output behavior from Fig. 3.11 a, the sensor exhibits a small hysteresis, and the linear behavior is still not achieved. Figure 3.11 represents the variation of the TMR and area resistance values within the same stack. It's worth noting the large variation of the area resistance, which is common for all the stacks and is attributed to the large variation of the sensor area due to its reduced submicron dimensions.

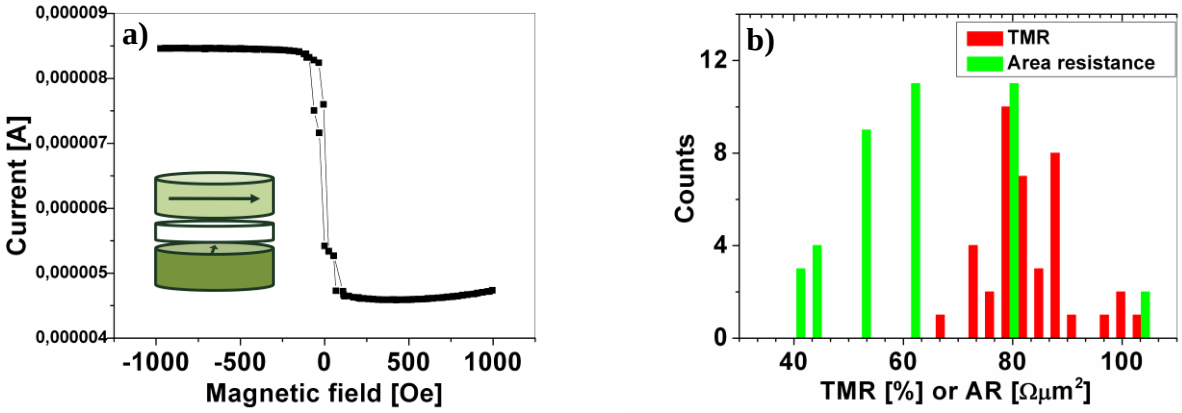

Fig 3.11. (a) TMR measurements of a layer stack with the following composition, with thickness in the brackets given in nm: Ta(5)/CuN(30)/Ta(5)/PtMn(20)/CoFe(2.3)/Ru(0.825) /*CoFeB(2.2)*/MgO(1.4)/*CoFeB(3)*/Ta(10)/CuN(10)/Ru(7) from Singulus Nanodeposition Technology (b) Statistic TMR and area resistance data regarding the previous stack with measurements done within 2 arrays of 20 sensors each

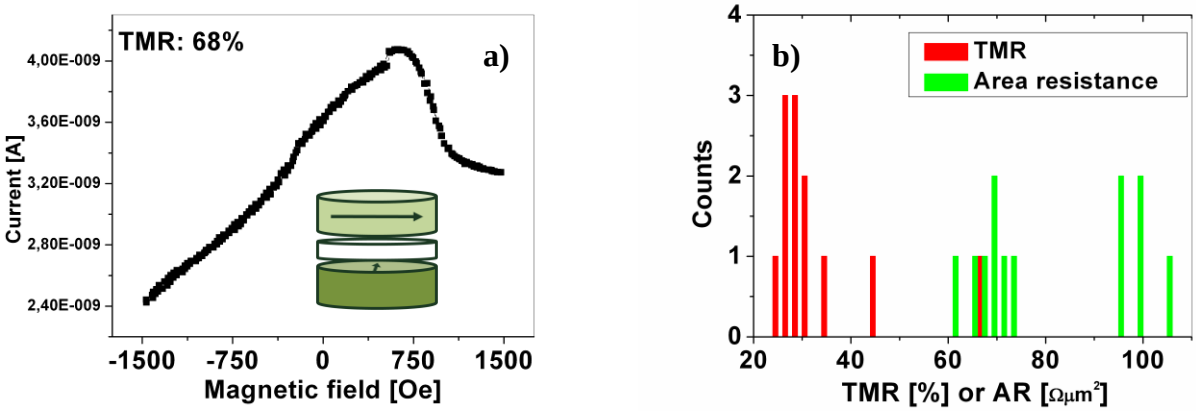

Fig 3.12. (a) TMR measurements of a layer stack with the following composition, with thickness given in nm:Ta(5)/Ru(30)/Ta(10)/MnIr(10)/CoFe(3)/Ru(0.8)/*CoFeB(3)*/MgO(1.8)/*CoFeB(10)*/Ta(7)/Ru(7) (b) Statistic TMR and area resistance data regarding the previous stack with measurements done within 1 arrays of 20 sensors each in the linearity range

An important aspect that can be excerpt from the presented results is that a linear output for a TMR element is related to the thickness of the top sensing layer and the strong pinning of the bottom ferromagnetic electrode. The magnetic behavior of the top ferromagnetic layer is determined by a cumulus of three types of anisotropies: uniaxial (K_u) induced anisotropy, magnetocrystalline anisotropy (K_1) and shape anisotropy. When the thickness of the thin film is smaller than 3.1 nm, the uniaxial anisotropy is present due to the miscut in the film sputtering and favors a strong coupling between the ferromagnetic layers with the thickness of 2.5 nm. When the K_u/K_1 ratio is comprised between 0.18 and 0.64 and in the case above the top layer has a thickness larger than 3 nm, the uniaxial anisotropy decreases, while the magnetocrystalline anisotropy increases (25). Due to the elliptical shape of the submicrometer sized element with an aspect ratio of 1/4, the shape anisotropy is dominant. This is why the top ferromagnetic layer will take the magnetization orientation of the easy axis of the ellipse. By increasing the top layer thickness and keeping the ortogonality of the two ferromagnetic layers a large linearity range can be observed in the sensors output as is exemplified in Fig. 3.12.

3.5 Noise present in TMR sensor elements

Even if noise is correlated with unwanted signals that are affecting the electrical measurements, it can provide also useful information about the structures that are studied. This part of the chapter will give a theoretical overview of noise in magnetoresistance devices. The experimental results regarding the noise present in these structures studied for sensor applications will be discussed as well. The resistance fluctuations present in the TMR elements are an important tool for probing the dynamics of magnetic instabilities and their coupling to charge carriers via spin dependent scattering processes on the nanometer scale. The most common noise sources include: defect motions, magnetic domain or spin fluctuations, charge carriers that are crossing an energetic barrier, electronic traps and current redistribution within electronic materials (68). These sources give rise to different type of noise: thermal noise, shot noise, $1/f$ noise and random telegraph noise.

Thermal (Johnson-Nyquist) noise was first observed by Johnson in 1927 and then theoretically analyzed by Nyquist in 1928. It appears in all resistors due to the thermally activated motion of the charge carriers. It can be characterized by a thermal smearing of the DOS at the Fermi level (69). Its power spectral density has the following form:

$$S_V = 4k_B TR \tag{3.5.1}$$

With $k_B$being the Boltzman constant, T the temperature and R the resistance value.

Shot noise has been experimentally observed by Schottky in 1918 and is related to the passing of current across an energy barrier, being a non-equilibrum form of noise. The shot noise arises because the current is not a continuous flow of electrical charges, it consist of a sum of discrete pulses in time. This type of noise is absent in metallic devices where the current fluctuations are smoothed by the electron-photon inelastic scattering, so the discrete character of the current is hidden. In case of magnetic tunnel junctions, the shot noise is emphasized due to the tunneling phenomenon through an insulator barrier, the discontinuous medium between two conducting layers. If the measurements are made employing a constant current source, the voltage power spectral density follows equation:

$$S_V = 2eIR_d^2 \tag{3.5.2}$$

Where e represents the electric charge of an electron and I is the current that is passing through the resistor and R_d is the differential resistance characteristic of the magnetic tunnel junction:

$$R_d = \frac{dV}{dI} \tag{3.5.3}$$

The thermal and shot noise are frequency independent and are included in the white noise category. For magnetic tunnel junctions is very difficult to distinguish between thermal and shot noise. Their contributions to the spectral power density are given by the following term:

$$S_V = 2eIR_d^2 \coth\left(\frac{eV}{2k_BT}\right) \tag{3.5.4}$$

It can be observed that for an increasing bias voltage at low temperatures, $eV \gg 2k_BT$, the noise is reduced to the shot noise relation $2eIR_d^2$ (70).

$1/f$ (flicker, excess) noise can be characterized by the fluctuations of a physical variable with a power spectral density that is following a $1/f$ law. It is worth noting that the applied current doesn't create these fluctuation, it just reveals them above the white noise (68). When the size of the measured sample is reduced, the size of the noise sources remains the same, so it is expected to have stronger fluctuations of the overall transport in small size elements. The $1/f$ resistance fluctuations can be described by the empirical Hooge formula:

$$S_V = \frac{\gamma_H V^2}{N_C f} \tag{3.5.5}$$

Where N_C represent the number of carriers participating in the current I, γ_H is the Hooge parameter constant, quantifying the magnitude of the $1/f$ noise for a certain device. Regarding magnetic tunnel junctions N_C is exchanged by the area A of the magnetic device. The resulting expression is more adequate for current perpendicular to plane geometry devices.

$$S_V^{MTJ} = \frac{\gamma_H V^2}{Af} \tag{3.5.6}$$

The $1/f$ characterization has been developed the Dutta-Dimon-Horn model for the electrical noise in the magnetic materials. The magnetic order and its stability can be measured

versus time giving insights in the spin or domain fluctuations (71). The origin of the $1/f$ noise can be electronic as the fluctuating bonds in the tunnel barrier or of magnetic origin, for example, fluctuation of the magnetization next to a structural defect (72).

Since the nature of $1/f$ noise in MTJs can be divided in a magnetic field independent part and a magnetic field dependent part (70), an initially hypotheses was that the origins of the magnetic field dependent $1/f$ noise are associated to magnetic impurities and the spin dependent charge traps (Fig. 3.13). But the presence of a specific two state fluctuator in the AP orientation of the two ferromagnetic electrodes and its absence in the P orientation of the electrodes rules out the magnetic impurities reason for magnetic field dependent $1/f$ noise. The scaling of γ_H with dR/dH (70), (69) is inconsistent with spin dependent charge traps theory. Related to these discoveries it has been postulated (70) that the 1/f noise is related to the reversal of the fixed layer, due to thermal magnetic fluctuations that couple to the resistance via the spin dependent tunneling effect.

The magnetic field independent component of the $1/f$ noise is presumed to be caused by the localized electronic traps in the barrier or by the oxygen vacancies moving between nearly equivalent sites. These effects lead to tunnel barrier height fluctuations. It has been discovered that the noise is given by the tunneling electrons with large parallel components of their k wave vector from minority or majority band (73). As in the antiparallel orientation of the two ferromagnetic electrodes, the tunneling is realized by the minority localized electrons with a large parallel component of the k wave vector, hence it is normal to expect a higher noise level in this case. This theory is in coincidence with the magnetic impurities localized charge traps in the insulator.

During experimental measurements, magnetic and non-magnetic components of the $1/f$ noise will always be combined. From the mathematical point of view, the $1/f$ fluctuations are a superposition of two independent and random processes with a wide bution of relaxation times whose time scale is coherent with the low frequency processes (68).

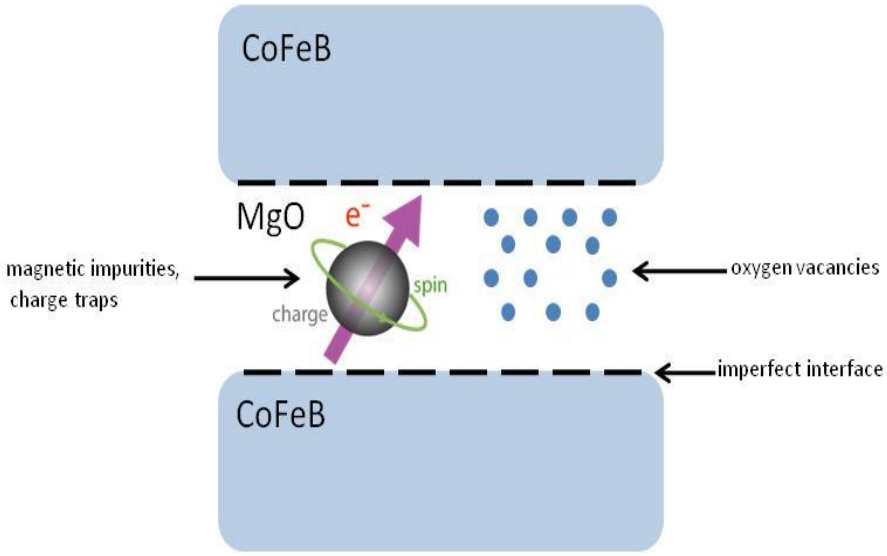

Fig. 3.13 Schematic representation for the origins of the 1/f noise sources

Random telegraph noise (RTN) is used to describe the noise when only single fluctuations or electrons are involved. This is the dominant low frequency noise in magnetic and non-magnetic junctions. It has been experimentally observed that only small sized elements in the submicromter range exhibit RTN noise. This is related to the microscopic origin of this type of noise, associated with the trapping and detrapping of electrons located in an insulator. If a charge trap is located in the insulating barrier, it will induce a Coulomb field that is changing the energy barrier. Due to the small thickness of the tunneling barrier even 50% of resistance fluctuations can be reached due to this phenomenon. It has been observed that a crossover from the 1/f to the RTN noise occurs when the size of the measured sample becomes comparable with the size of a single magnetic domain. RTN has been proved to be related to the switching of the free layer (due to thermally activated domain rotation or domain wall hopping between pinning sites). The pinning sites could be produced by: surface or edge roughness, bulk defects, random anisotropy due to the disorder of the film (70).

Summarizing the general characteristics of noise in solid state devices, it can be concluded that the noise can be classified in two categories: low frequency noise that include the RTN and the 1/f noise and the high frequency (white) noise as shot and thermal noise. In case of magnetic tunnel junctions, the low frequency noise are the ones that can

be observed and analyzed (74), (73). By examining the detection devices an important aspect consist in revealing the signal to noise ratio. This aspect provides information about the expected minimum signal that can be detected. The combined power spectral density of the noise resulting from the shot noise, thermal noise and $1/f$ noise is given by (75):

$$S_V = 2eIR_d^2 coth\left(\frac{eV_b}{2k_BT}\right) + \gamma_H \frac{I^2R_d^2}{Af} \tag{3.5.7}$$

where e is the value of the electron charge, V_b is the bias voltage over the junction, R_d is the differential resistance of the tunnel junction, k_B is the Boltzmann constant, A is the junction area and γ_H is a function of that parameterizes the $1/f$ noise magnitude. The first term in the power spectral density is given by the combination of Johnson noise and shot noise, while the second term is given by the $1/f$ contribution. In magnetic tunneling junctions used for magnetic bead detection, the noise power spectral density is found to be a superposition of shot noise, thermal noise and 1/f noise.

Figure 3.14 shows a schematic noise power spectral density including its components. It can be observed that the crossover from the frequency dependent noise to the frequency independent noise occurs below a few kHz. Figure 3.15 a shows a typical measured power spectral density (PSD) curve for a standard MTJ element used for sensing experiments. As can be seen the 1/f and RTN type of noise are dominating in the frequency range of interest. The presence of RTN noise is indicated by the existence of the bump in PSD. The time dependent measurements of the sensors (Fig. 3.15 b) revealed sharp switching caused by the RTN. The detection limits of the sensor are imposed by its fluctuations over time. The RTN noise could originate from a local non-uniformity of anisotropy.

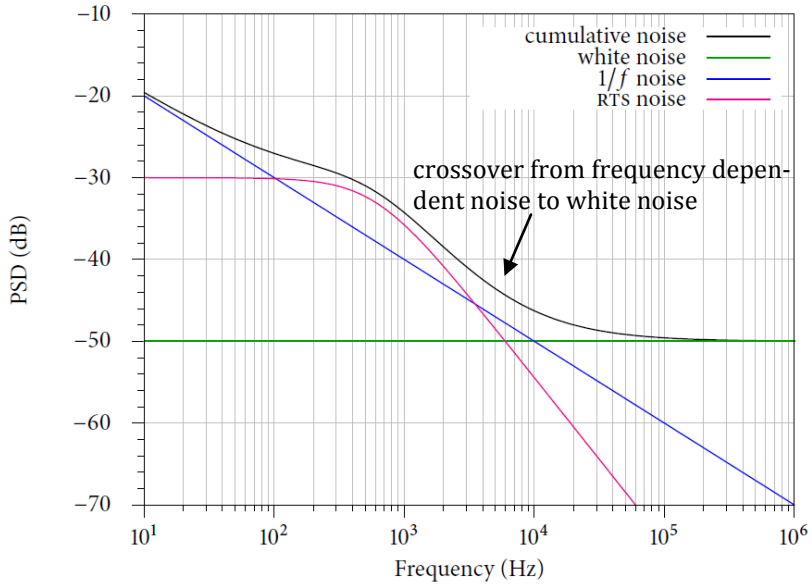

Fig. 3.14 Schematic representation of noise PSD for MTJ elements

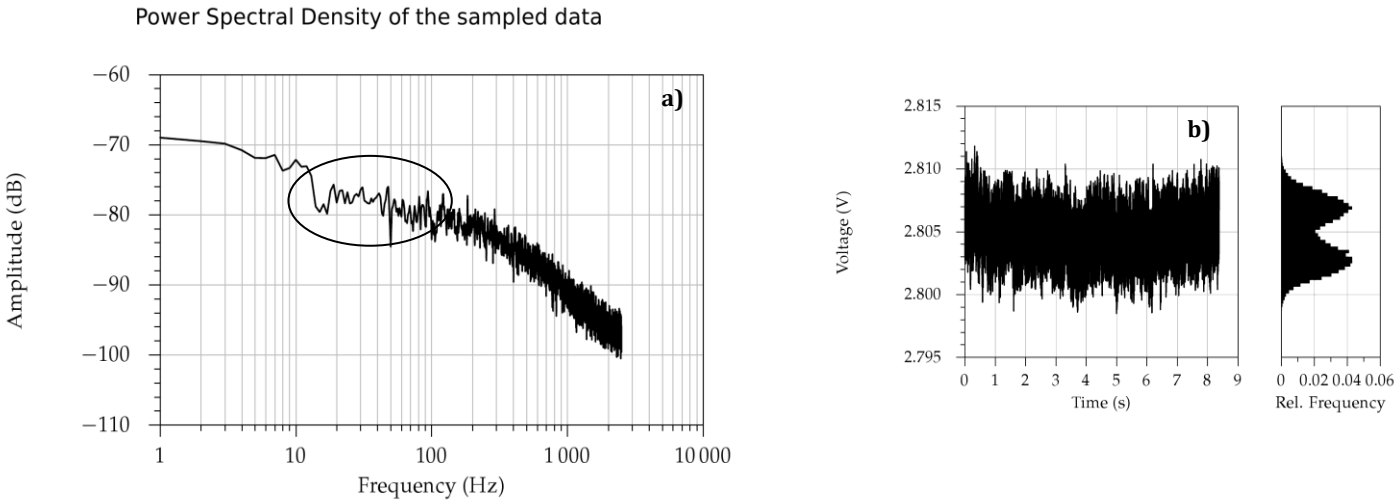

Fig. 3.15a) Typical noise measurement for a standard magnetic tunnel junction element used for sensor applications b) Time trace measurements indicates sharp switching of the sensor due to the presence of the RTN noise

3.6 Heusler alloy based sensors

In the following part of this subchapter, the basic concept about the Heusler alloys and their application for magnetic sensor devices will be discussed. The Heusler alloys have been discovered at the beginning of the last century as being formed from non-magnetic elements, but exhibiting a magnetic behavior (76). Today, Heusler components designed for spintronics are the half-metal materials with a gap for one type of spin polarized electrons and being metallic for the other spin type at the Fermi level. Hence, the majority spin band has a metallic behavior, while the minority spin band has a semiconducting behavior at the Fermi level. Because of these characteristics they can exhibit a spin polarization of 100%, which is at least theoretically predicted.

The best indication for a half metallic compound is an integral number of Bohr magnetons per unit cell (77). This can be achieved by hybridization, by pushing the 4s band with the non-polarized electrons above or below the Fermi level. The total number of electrons is given by:

$$Z_t = n\uparrow + n\downarrow \tag{3.6.1}$$

and the total spin moment by:

$$M_t = n\uparrow - n\downarrow \tag{3.6.2}$$

so the total spin moment becomes:

$$M_t = Z_t - 2\,n\downarrow \tag{3.6.3}$$

The Slater–Pauli rule gives a number of 12 e^- per unit cell in the minority band: 4 lying in the s and p bands and 8 in the d bands. By concluding, the total spin moment for full Heusler alloys is given by:

$$M_t = Z_t - 24 \tag{3.6.4}$$

The $La_{1-x}Sr_xMnO_3$ ($LSMO$) half metal crystallizes in a perovskite structure and shows 1800% TMR at 5K and a spin polarization of 95%, in LSMO/MgO/LSMO tunneling junction (78). Unfortunately, LSMO has a very low Curie temperature, so it cannot be used

for measurements at room temperature, this being the reason why is not suitable for commercial applications.

Full Heusler alloys are ternary intermetallic compounds and have a X_2YZ crystallizes in L_21 structure. This structure is formed by 4 interpenetrating fcc sublattices with atoms in the following positions: A (0 0 0), C (½ ½ ½), B (¼ ¼ ¼) and D (¾ ¾ ¾) (79). The X and Y are transition metals, while the Z is an element from the III_b or IV_b group. When there is an atomic disorder the L_21 structure will transform to B_2, DO_3 or A_2 structures. The B_2 structure is formed when the X atoms are ordered but the full disorder is between Y and Z atoms. The DO_3 structure appears when the disorder occurs between one X site and either Y or Z sites. The A_2 structure is characterized by a random disorder among the three X, Y, Z sites (80). It has experimentally been observed that thin films of Heusler alloys crystallizes in B_2 or A_2 structure if are annealed at a temperature of 630 K and present L_21 structure if the annealing temperature is higher than 600 K. An important factor to achieve the L_21 structure is given also by the substrate used for thin film deposition (81), (82). Impurities have a high contribution to the degree of disorder in the structure of Heusler thin films. A major problem is the presence of the oxygen. The oxidation of the Heusler alloys can occur during the barrier formation in case of magnetic tunnel junctions (80). The spin polarization of Co based full Heusler alloys is very sensitive to the site disorder (83), (84). Experimental observations showed similar TMR values for the thin films exhibiting B_2 or L_21 structure. This is highly important when considering multilayer structures because a high annealing temperature (required to achieve L_21 structure) may lead to layers interdifussion, so it is desirable to anneal the structures at a temperature below or equal to 630 K.

The alloy being studied for its application in the sensor devices is the Co_2FeSi (CFS). It was chosen to be investigated owe to its compatibility with MgO structure. Co_2FeSi has $T_c = 1100\ K$, $H_c = 6.5\ mT$ and regarding to Slater-Pauli rule should have a magnetic moment of $6\mu_B$. When it is measured, the magnetic moment is reduced to 5.2 μ_B (85). The reduction of the magnetic moment is expectable, because many atoms present in thin films structure are situated at the interface or in disordered atom sites compared to the bulk

structure. Some other studies revealed a Curie temperature of 980 K and a magnetic moment of 5.18 μ_B/unit cell (86). It has been experimentally observed that Co_2FeSi crystallizes in bulk by quenching after annealing at a high temperature or as a thin films sputtered on GaAs substrates. In the case of deposition on SiO_2 substrate an A_2 structure of the Heusler based thin films has usually been observed (84). The structure of Co_2FeSi has been proven to be of grain type, with a high film disorder. The deposition and annealing techniques used for Heusler alloys have a strong influence on their structural and magnetic properties. By increasing the annealing temperature, the site disorder is reduced, the crystalline phases are more likely to be formed, and also the magnetocrystalline anisotropy is stronger. The main reason why Heusler alloys don't exhibit a high spin polarization is related to the low degree of order for the L_21 structure at room temperature. The conduction through minority spins is increasing due to the thermal excitation at room temperature.

One requirement for increasing the spin polarization is to achieve a good L_21 ordering (87). By using the point contact Andreev reflection (PCAR) method it has been stated that Co_2FeSi exhibits a spin polarization of 0.49 ± 0.02 (88). It has also been reported that the TMR value could be mainly deduced from the intrinsic value of the spin polarization of the electrodes without notable influence from the interface between the Heusler alloy ferromagnet and the tunneling barrier. By using magnetic tunneling junctions with CFS as ferromagnetic electrodes and MgO tunneling barrier, a value of TMR of 44 % at RT and 68% at 5 K, after annealing the sample at the temperature of 573 K has been measured (84). An important application of the Heusler alloys can be found in spin MOSFET (89) and shape memory alloys (90).

The employment of Co_2FeSi in sensor applications has been studied in this case. Statistics for the magnetic behavior of a standard stack (see Fig. 3.6) where the top sensing layer is replaced by a 7 nm Co_2FeSi layer. Fig. 3.15 reveals the magnetotransport measurements for the Heusler based sensor stack, when the two ferromagnetic electrodes have a parallel orientation of magnetization.

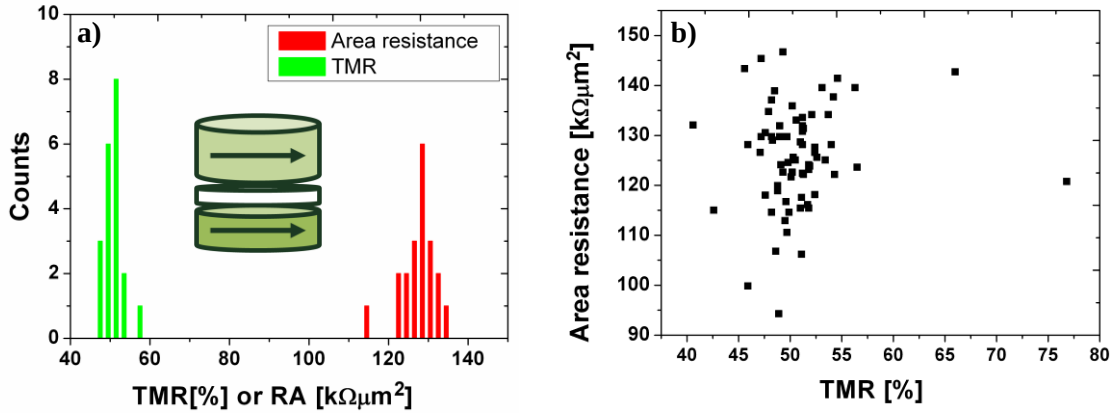

Fig. 3.16 a) Statistical data regarding the area resistance and TMR values for one array of 20 sensors with Co_2FeSi as top free layer in parallel orientation b) Area resistance plotted versus TMR values for 4 arrays with the Heusler alloy Co_2FeSi as top free layer;

In order proof whether Co_2FeSi based sensors are suitable for sensor application, samples with orthogonal orientation of the two ferromagnetic electrodes have been patterned. Their magneto transport properties are shown in Fig. 3.17.

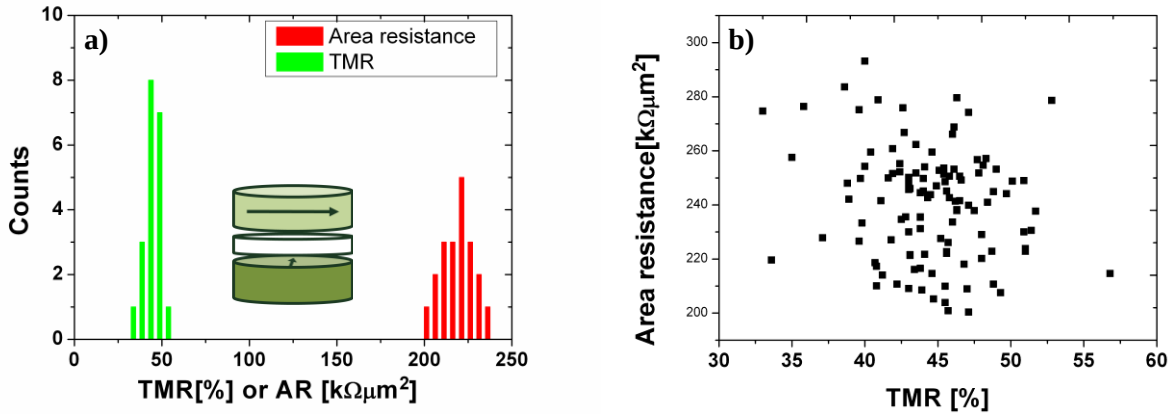

Fig. 3.17 a) Statistical data regarding the area resistance and TMR values for one array of 20 sensors with Co_2FeSi as top free layer in orthogonal orientation b) Area resistance plotted versus TMR values for 6 arrays with the Heusler alloy Co_2FeSi as top free layer;

Figure 3.18 exhibits statistical data for a standard stack having the top layer of 4 nm CoFeB as comparison for the data obtained from the Heulser based sensors. For the standard stack, the values for the area resistance and TMR are having a large distribution range.

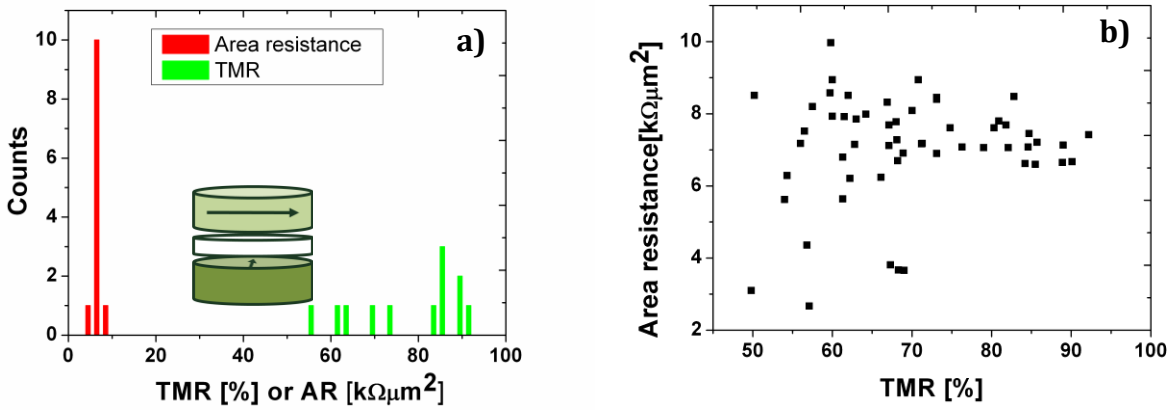

Fig. 3.18 a) Statistical data regarding the area resistance and TMR values for one array of 20 sensors with CoFeB as top free layer in orthogonal orientation b) Area resistance plotted versus TMR values for 4 arrays with CoFeB as top free layer;

Figure 3.19 shows the difference between the linear range obtained for the stack with 4 nm CoFeB and with 7 nm Co_2FeSi.

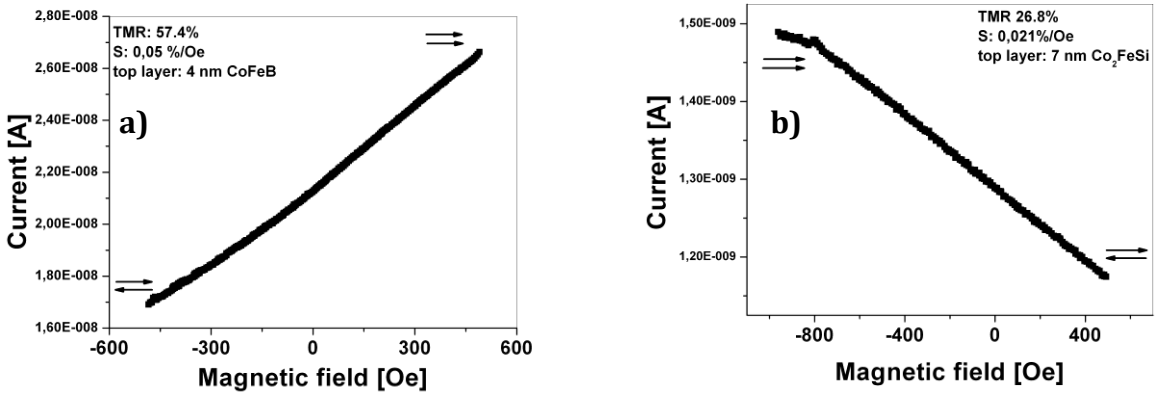

Fig. 3.19 Comparison between linearization range for the stacks having a) 4 nm CoFeB and b) 7 nm Co_2FeSi

It can be observed in Fig. 3.16 and Fig. 3.17 a very small variation of the resistance values within the sensors situated in different arrays. The Co_2FeSi alloys have very low magnetocrystalline anisotropy, thus being weak ferromagnets. Owe to this property, the Heusler based sensors are expected to have a very low intrinsic noise level. An investigation of the noise exhibited by the Heusler based sensors is shown in Fig. 3.19. When compared with the noise exhibited by the standard stack (see Fig. 3.14) with CoFeB (4 nm) as the top detection layer it is observed that the noise level for the Heusler based sensors has a smoothened profile and the RTN type of noise is absent. This is advantageous for dynamic sensing applications, where it is preferable to have the response from the magnetic stray field at higher levels compared to the intrinsic noise jumps of the sensor. The noise measured for the standard stack based sensors presents large fluctuations that might have its origin in fluctuation of crystalline lattice orientation. Although the Heusler based sensors show a reduced noise level, their sensitivity is almost ten times smaller compared to the standard stack sensors with CoFeB as free sensing layer, because the Heusler based stack has a lower MR ratio compared to the standard stack. Lately, high TMR values of up to 147% at RT have been observed for stacks using the Heusler compound Co_2FeAl as one of the ferromagnetic electrodes (91). By integrating Co_2FeAl in TMR sensor stack, a new generation of magnetic biosensors with an increased sensitivity and low noise level can be produced.

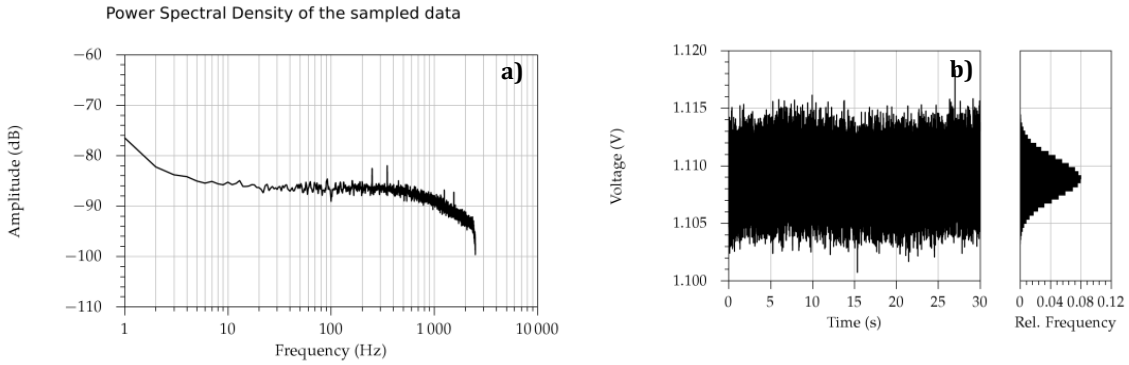

Fig. 3.20 a) Typical noise measurement for a Heusler based magnetic tunnel junction element suitable for sensor applications b) Time trace measurements reveals the absence of RTN noise in Heusler based sensors.

4. Magnetic markers manipulation

The content of this chapter includes details regarding different lithographic constructions for magnetic bead and nanoparticle manipulation. Because the area where the sensors are positioned is very small, 20 sensors over an area of 18.2 μm^2, the employment of different means to attract the magnetic markers on top of the sensors surface is necessary.

4.1 Magnetic field lines for magnetic beads manipulation

One important advantage of magnetoresistive sensors for magnetic detection purposes relies in the possibilities of manipulating magnetic beads on top of the sensors surface. To realize such manipulation additional conduction lines or other structures are constructed above the sensors surface.

The construction of the magnetic field lines requires two additional lithography steps and care must be taken for the protection of the sensors. The first lithographic step aims for covering the contact pads of the contact lines used for magneto-transport measurements with negative e-beam resist. After development, the resist will not be removed, but 100 nm of TaO_x will be sputter on top of the contacting lines. Directly after TaO_x deposition a layer of 50 nm of gold will be sputtered to provide the material for the top magnetic field lines. The second step is patterning of the magnetic field lines. In this phase, the lines itself are structured using negative e-beam resist. The magnetic field lines geometry has been changed relative to their practical purpose. The most important constructions that have been done in order to manipulate the magnetic markers will be presented in this chapter.

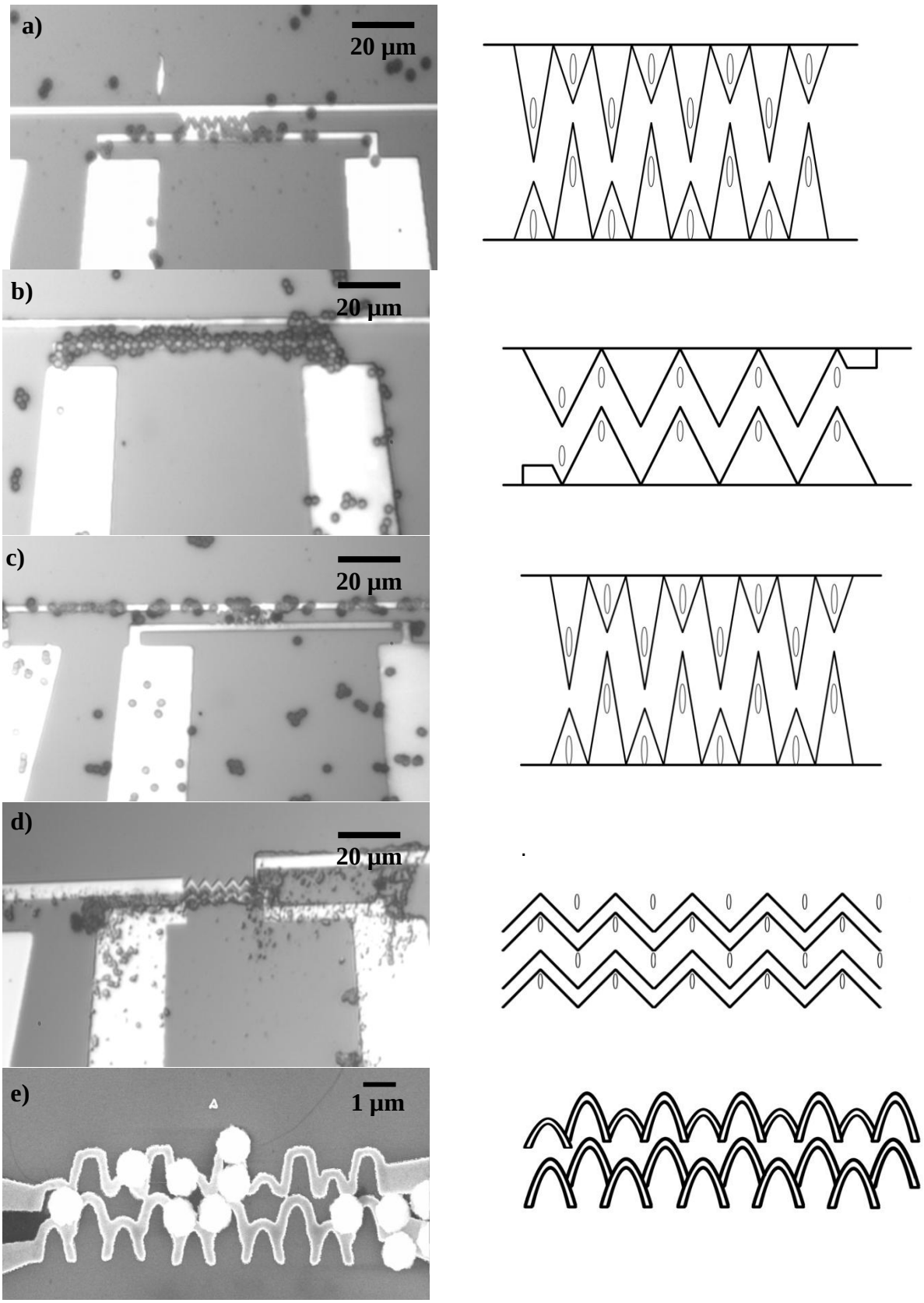

Fig. 4.1 Representation of different conduction lines concepts to achieve a proper manipulation of magnetic particles on top of the sensors; the right part of the figure presents the sketch of the design for the magnetic field lines

through the magnetic field lines, a magnetic field is generated, which attracts the magnetic markers on top of the sensor surface. By including additional layers on top of the sensor surface, the distance between the magnetic marker and sensor increases. Consequently, the stray field from the magnetic beads at the sensor position is also weakened. Figure 4.1 summarizes different geometries of magnetic field lines that have been tested to ensure the positioning of magnetic beads exactly on top or in close vicinity to the elliptical sensors. When a current between 5 and 15 mA is applied, the resulting magnetic field is strong enough to attract and guide magnetic particles towards the lines. In the region where the lines are triangular shaped, the magnetic field gradient is higher, so the magnetic beads will be attracted to that area with an increased probability. It has been observed that the velocity of the beads is increasing, and they are guided rapidly to the lines. A major disadvantage of this technique is that beads agglomeration is favored. When the beads are clustered, their magnetic moment will arrange with the aim of minimizing the total stray field of the formed cluster. Thus, their total magnetic moment would be either very small or even absent. Details regarding magnetic field lines used for magnetic beads manipulation can be found in (12).

From the geometry concepts presented in Fig. 4.1 it can be seen that the one from Fig. 4.1.b is advantageous and attracts the magnetic markers in a proper manner on top of the sensors. The sketch of the magnetic field lines is emphasized in the right part of the figure. The optical microscopy images in the left part of Fig. 4.1 exemplify how the magnetic beads are guided to the magnetic field lines. Caution must be taken regarding the maximum value of the dc current that runs along the magnetic field lines, in order to prevent electromigration. Because all the processes take place in liquid, the heating effects are high and the magnetic field lines are susceptible to easy destruction.

4.2 PMMA holes for placing the nanoparticles

For the magnetic detection of nanoparticles, the guiding magnetic field lines cannot be used because the distance between the top free sensing layer of the sensor and the nanoparticle would be more than 200 nm. Taking into account that the size of a nanoparticle is less than 20 nm, its stray field would hardly reach the sensor. Therefore, other means of manipulation have to be employed. An interesting method has been proposed by Stanford researchers (92) and adapted also for the sensor arrays used in

this thesis. The method consists in making special placed holes using positive e-beam resist (PMMA). The advantage of the PMMA is connected to the possibility of patterning small structures, with a lateral size smaller than 100 nm. Consequently, these holes can be placed at different positions on the sensor surface in order to trap the nanoparticles in a comfortable manner. The construction of the PMMA holes is done by following steps given in Fig. 4.2.

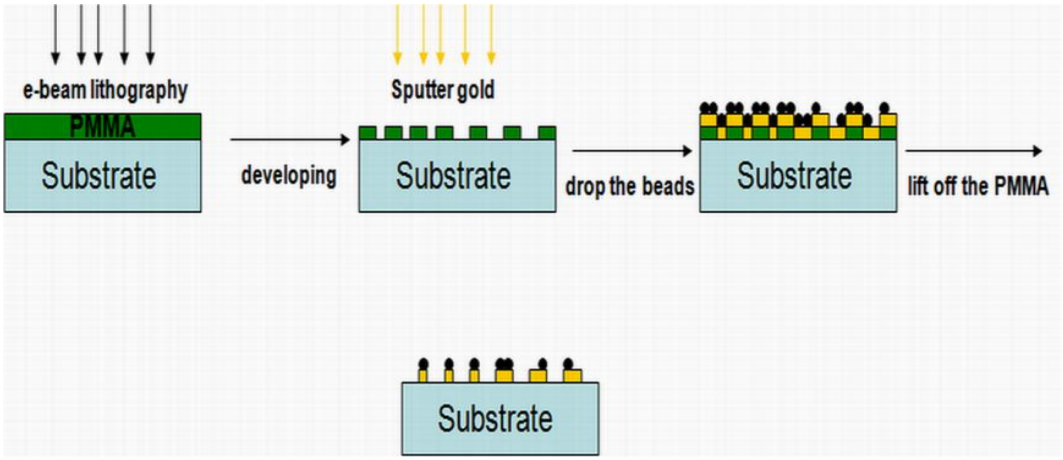

Fig. 4.2 Fabrication of PMMA holes

Due to the fact that the nanoparticles are covered with oleic acid, they are sticking to the substrate surface. Unfortunately, it was not possible to remove the PMMA resist in the vicinity of the holes. Figure 4.3a shows that nanoparticles are present in areas around the constructed hole, indicating that lift off process has not worked correctly. After a further removing step, using 1 Methyl-2-Pyrrolidinone for 60 min at 60°C, it was possible to observe that the nanoparticles were staying only in the area where the PMMA structures have been patterned.

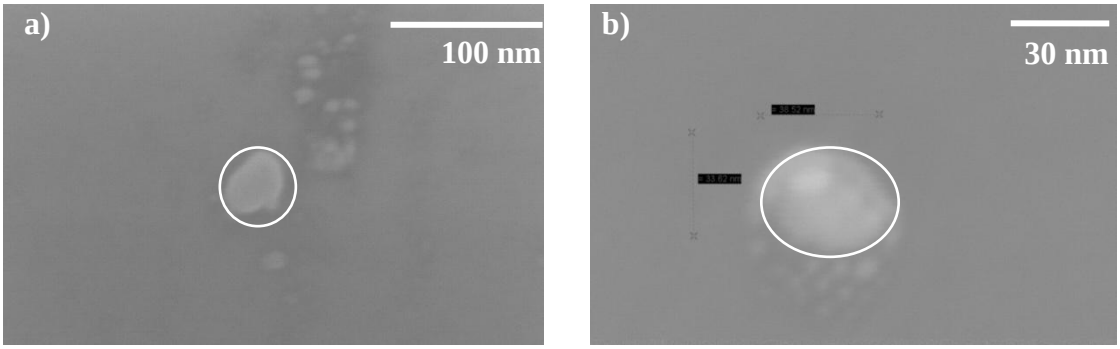

Fig. 4.3 SEM images of the nanoparticles positioning on top of the PMMA holes

Nevertheless, the process of placing magnetic nanoparticles exactly on top of the sensor area cannot be done efficiently. Furthermore, using the above mentioned lift off processes, the sensor quality will decrease also very much, more than 50% of the elements being destroyed. Hence, to further exploit the magnetic nanoparticles detection, simple dropping of nanoparticles has been used. This procedure prevents sample contamination with other unwanted materials and sensor destruction.

5. Static detection of magnetic markers

5.1 General overview regarding magnetic detection

This chapter is dedicated to describe the detection of magnetic markers by magnetic tunneling junctions. An overview of the detections schemes used by other groups for sensing magnetic beads or nanoparticles will be presented first. This is done in order to make a comparison between the results obtained by other groups and the results presented in this thesis. The major advantage of tunneling magnetoresistive sensors is the possibility of downscaling them to submicrometer dimensions without any loss of sensitivity. The TMR sensor sensitivity is increasing by shrinking the size of the elements because the TMR ratio is also increasing. The probability to contain impurity and defects in the barrier is reduced as the downscaling of the elements takes place. By having the sensor dimension in the same range as the magnetic markers, single magnetic marker detection can be achieved. By attaching one molecule to a magnetic particle, it is be possible to obtain information regarding the position of the molecule in a defined moment of time. This could lead to a deeper comprehension of processes taking place at single molecule level. Observing the chemical-physical interaction between a reduced numbers of molecules could give more insights to understand the underlying bonding mechanisms.

The principle of magnetic detection is based on the influence the magnetic stray field of magnetic marker has on the orientation of the magnetization of the top free layer of the sensor. Due to this small orientational change, the resistance and the TMR of the sensor are affected. The magnetic stray field produced by magnetic markers is characterized by a dipole as magnetic field. The orientation of this dipole field is defined by the direction of the external magnetic field. The external magnetic field can be applied in-plane or out-of-plane direction. The magnetic beads are coated with various chemical or biological species that are selectively binding to other biological species

which one wants to analyze. These coatings are non-magnetic, so they do not influence the magnetic detection, making the appliance of the magnetic sensors very specific (93), (94).

The sensor element is sensitive only to one axis in the plane of the film. By applying a magnetic field perpendicular to the sensitive axis, it is possible to obtain a linear behavior of the sensor output. The sensor's linearity is obtained by applying the external magnetic field along the short axis of the elliptical sensor, which is in the y direction as is pictured in Fig. 5.1 (95).

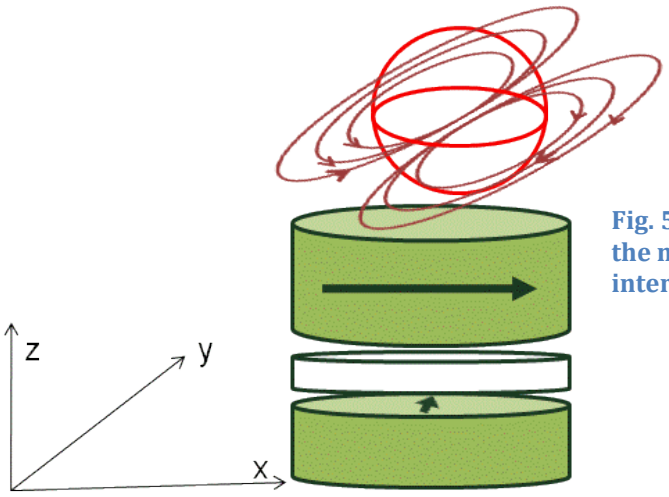

Fig. 5.1 Scheme of magnetic detection: the magnetic dipole field of the bead interacts with the TMR sensor

Figure 5.1 reveals a schematic representation of a magnetic detection. The dipole field of the magnetic bead will influence the TMR sensor behavior. The magnetic marker is superparamagnetic, which means it exhibits magnetic properties only when it is immersed in an external magnetic field. The magnetic field of the magnetic bead is localized and decreased with $1/r^3$ as a function of r. A critical issue is to magnetize the marker with a sufficiently high magnetic field, in order to have an increase value of magnetization and therefore a strong local stray magnetic field, without saturating the sensor. The advantage of the sensors used in this work is their wide magnetic field range due to their linear behavior without saturating the sensor. This increases the detection sensitivity. It's worth noting that the magnetic bead stray field is not uniform and doesn't have the same intensity for each and every bead. This is due to the variation of magnetic content of each bead.

The magnetic field of the magnetized bead is characterized by a pure dipole as follows:

$$B = \frac{\mu_0}{4\pi}\frac{1}{\hat{r}^3}[3(\hat{m}\cdot\hat{r})\hat{r} - \hat{m}]$$

(5.1)

Considering the bead magnetized along the x axis, in Cartesian coordinates, the magnetic field produced by the magnetic bead in the x direction will be:

$$\hat{m} = m\cdot\hat{x} \tag{5.2}$$

$$B_x = \frac{\mu_0}{4\pi}\left[\frac{3mx^2}{(x^2+y^2+z^2)^{5/2}} - \frac{m}{(x^2+y^2+z^2)^{3/2}}\right] \tag{5.3}$$

The characteristic of such a field yields a curve with two negative peaks at its edge and a positive component centered between them (94). In many cases the markers used for magnetic detection are magnetized along the x direction. The magnetic dipole expressed in Cartesian coordinates gives a good approximation of the field when the bead is situated directly on top of the sensor. For practical reasons it is important to convert the magnetic dipole produced by the magnetic moment of the bead in polar coordinates. This helps to understand the influence of the magnetic dipole of the bead when oriented in various directions relative to the sensor (96). The two components of the dipolar field at a location r from the center of the bead are described by the radial component H_r and the angular component H_θ.

$$H_r = \frac{2\hat{m}}{\hat{r}^3}\cos\theta \tag{5.4}$$

$$H_\theta = \frac{\hat{m}}{\hat{r}^3}\sin\theta \tag{5.5}$$

In the equations above θ is the angle between the position vector $\hat{r}$ and the direction of the magnetic moment $\hat{m}$. The vector $\hat{r}$ is pointing from the center of the bead to the center of the sensor.

If the bead is situated exactly above the sensor with an angle θ of $\pi/2$, then the dipolar magnetic field from the bead will oppose the applied magnetic field and the resistance of the sensor should drop. This effect has been observed from the experiments of several groups working with diverse types of magnetoresistive sensors. A large amount of experiments have been proceeded on giant magneto-resistance and

spin-valve sensors due to their easier process of fabrication and facile means of measurements.

Magnetic beads can be also magnetized by applying an out-of-plane magnetic field. The advantage of this method is that the sensor's sensitivity will not be influenced. In this case, the stray field of the magnetic marker will be radially symmetric compared to the uni-directional stray field of an in-plane magnetized bead (97), (98). Another advantage of the out-of-plane magnetization is that high magnetic fields can be applied to magnetize the beads without saturating the sensor. It is worth noting that in this case, an in-plane magnetic field has also to be applied so as to sense the resistance change of the sensor (99). From the simulated magnetic bead detection it can be concluded that the fingerprints of a magnetized bead is different relative to their magnetization direction. For better results it is important to consider the sensor and the magnetized bead as an unit and not to study the effect of the stray field of the bead over the sensor.

In the following paragraphs is given a chronological evolution of magnetoresistive sensors at different institutions. The overall trend was to cross from giant magnetoresistive sensors to highly sensitive tunneling magneto-resistance sensors, first the ones with Al_2O_3 and then with MgO as insulator barrier material. Ideal sensors should be sensitive enough to detect a small number of nanoparticles tags with single DNA strands.

5.1.1 Magnetoresistive sensors evolution at Bielefeld University

Former colleagues of Bielefeld University have done a comparison between the detection of DNA with fluorescent markers and with magnetic beads. The external field was applied in the out-of-plane direction, the GMR sensor detecting the in plane field of the bead. The experiment has been done over a broad range of concentration analytes, from 16 pg/µl to 10 ng/µl. It has been observed that for low probe DNA concentrations, the magnetoresistive detection is superior to fluorescence detection by a factor of 2.7 at a concentration of 400 pg/µl (100). The main advantages of the magnetoresistive detection over the fluorescent one is found in the low cost of production. In the first case, no laser or detection optics is needed. Another advantage of magnetoresistive sensors is given by the absence of the background signal. Furthermore, due to the magnetic

based detection, the photobleaching effects encountered by the fluorescent dyes are nonexistent, so repeated measurements can be performed with the same sample. The detection signal from the 0.86 μm beads sensed by a 70 μm spiral shape GMR sensor has been proved to be linear with the sensor coverage, 200 being the minimum number of detected beads (101). As a remark to the previous experiments it has been uttered that the limiting factor in the magnetoresistive detection is not given by the magnetoresistance sensor, but by the binding process between the magnetic markers and the analyte molecules.

A comparison regarding the detection sensitivity between the GMR and the TMR sensors was also performed by the former colleagues from Bielefeld University (102). During the experiments it has been determined that the sensitivity of TMR sensors is four times higher than that of GMR sensors (97). It has been concluded that the TMR sensor is suitable to detect single magnetic bead, which will lead to single molecule detection. The TMR sensor capability to detect single magnetic markers has been tested with an MFM tip that mimics the presence of a single bead on top of the sensor surface (97). The magnetic tip is magnetized in a perpendicular direction and its dipole magnetic field will rotate the local magnetization by some degrees (103). It has been observed that the minor loop of the top sensing layer is influenced by the relative position of the magnetic tip towards the sensor.

5.1.2 Magnetoresistive sensors evolution at Lisbon, Portugal

Spin valve sensors have been initially proposed as read heads in tape systems, speed sensors and monitoring devices (104). Further, their applications have been extended to biological detection, when the superparamagnetic labels of different sizes and functionalization have been detected (105). Guiding lines have been integrated on the sensor's chip in order to manipulate the magnetic labels and bring them on top of the sensor surface. A change of 1% in MR has been observed when beads were passing by the sensor area. It is worth noting that the signal came from a cluster of beads that have been guided with the AC current lines (106). An important goal was to sense the biomolecular recognition in real time, which would lead to the investigation of single DNA molecule interaction. Using small spin-valve sensors ($2 \times 6\ \mu m^2$) it was possible to detect the binding of a single 2 μm streptavindin coated bead to a biotinylated sensor

surface (107). The magnetic field used to magnetize the bead was only 15 Oe. Thus, the magnetic bead's stray field is very small. The real time detection of the magnetic labels was realized. Using streptavidin-biotin bonding simultaneous detection of hybridization on-chip was achievable. The DNA sensing via the 250 nm magnetic markers was possible for very low target concentrations (108). The real time detection has been achieved by having initially an increased number of magnetic particles on top of the sensor surface. Due to the large number of labels, the sensor was saturated. Afterwards, several washing steps have been performed, so as to reduce the number density of beads which could be monitorized with the sensor (109). It has been theoretically predicted that the sensor response to the magnetic label stray field varies in sign with respect to the label orientation relative to the sensor (110). Due to the large amount of markers situated on the sensor surface, this prediction could not be proven experimentally. By attracting the DNA onto the sensor area with the help of special AC guiding lines (111) it was possible to reach a detection limit of 1pM concentration over a dynamic range of at least two orders of magnitude. It has been observed that the sensor signal is linear with the concentration of biological samples (112).

The cross over to magnetic tunnel junctions has been done as well motivated by a higher magnetoresistance ratio. The signal to noise ratio for MTJs and spin valve sensors has been compared. The conclusion of these studies was that the MTJs sensors are more suitable for single bead detection, so as to analyze a small amount of biologic material. The spin valve sensors on the other hand, seem to be appropriate for quantitative measurements of biological analytes that require an increased amount of magnetic labels. One characteristic that increases the signal to noise ratio for the magnetic tunnel junction elements is their high resistance. The preparation and operation conditions of MTJs are more complicated compared to the spin valve ones, making them a difficult choice. By testing the biological sensitivity between spin valve and magnetic tunnel junctions sensors it has been observed that the spin valve sensors are able to detect a smaller amount of DNA used as biomolecular label due to the fact that their fabrication and configuration is more convenient. In case of MTJ sensor elements, it was necessary to use a thicker passivation layer, to protect the sensors from damages caused by the biological fluids (113). Because the label signal decreases with the cube distance between it and the sensor surface, it is straightforward why the thick passivation layer decreases the detection signal. The author's opinion was that when used under identic-

al condition MTJ must be superior to the spin valve sensors. Other improvements done by the group from Portugal was to pattern on the sensor chip a U shape current line in order to attract the magnetic labels inside of it where the magnetic sensors are arranged. This would allow for a much faster hybridization time and is one of the advantages that the magnetoresistive chips are having (114). In series with Al_2O_3 based MTJ it can be fabricated a thin film diode that can select the cell of the matrix by forward biasing while the others are reverse-biased sensing and controlling the temperature of the place where it is located. It has also been studied the cross over from MTJs with Al_2O_3 to MTJs with MgO as the barrier layer. This was motivated by the larger magnetoresistance ratio for the MTJ's with MgO (115). Magnetic tunnel junctions with MgO tunneling barrier are the optimum choice for their use in the detection of magnetic field of low intensity in the pT range.

5.1.3 Magnetoresistive sensors evolution at Standford University

At the beginning of magnetoresistive sensor technology, spin valve sensors were the first choice of use (116). One spin-valve sensor had the smallest dimension of 2.5×10 μm^2 and was able to detect a single magnetic bead from Dynabead with a diameter of 2.8 μm and several 11 nm Co nanoparticles. The detection system is based on a Wheatstone bridge circuit, the voltage signal being amplified and then measured with a lock-in amplifier. The measurements are based on a detection scheme as follows: the detection signal is measured with the beads on top and is compared to the detection signal measured after the beads have been removed. When 16 nm Fe_3O_4 nanoparticles are used for detection it is observed that the most intense signal is obtained when the particles are situated in the center of the sensor (0.3×4 μm^2) area. Interestingly, the signal intensity decreases when the nanoaprticles are approaching the sensor edge, due to the fact that in this case, the nanoparticle's magnetic moment is enhanced by the stray field present at the edge of the sensors. In this case, the stray field of the sensor is also enhanced by the presence of the nanoparticles. The dependence of the signal intensity with distance between the free detection layer and the nanoparticles has been also studied. The maximum signal is reached when the nanoparticles are at a distance of 70 nm away from the sensor, not when the nanoparticles are directly situated on the sensor area. This has been assumed to be related to the fact that when the nanopar-

ticles are too close to the sensor area, the magnetostatic interaction between the stray field of the sensor and the stray field of the nanoparticles is very high (117). The cross over to the MTJ type sensors has been done so as to increase the sensitivity, which led to the detection of 12 nm $MnFe_2O_4$ that were functionalized with DNA (118), (119). Due to the lack of evidence for the superior sensitivity of the MTJ sensors over the spin valve sensors, it has been decided to use the spin valve sensors, thanks to their ease in fabrication. Interestingly it has been observed that the presence of 16 nm Fe_3O_4 nanoparticles on top of the sensor area gives a uniform signal when the nanoparticles are situated in the center of the sensor. But, when the nanoparticles are approaching the sensor edge, the detected signal is changing its shape due to the strong interaction with the sensor's stray field (92), (120). The detection limit was theoretically estimated to 14 nanoparticles, 11 femu, but a detection of 23 nanoparticles,17 femu, could be achieved experimentally.

5.1.4 Magnetoresistive sensors at Naval Research Laboratory

The group from Naval Research Laboratory was the first that published the idea of introducing the giant magnetoresitive effect in the field of biomedicine, by producing magnetoresitive biosensors. How the first BARC (bead array counter) came into being and its evolution in biodetection will be shortly presented in the further paragraphs. The idea starts from the necessity of measuring intermolecular forces between different proteins in a precise manner. The previous AFM based methods faced several difficulties in measuring the forces that holds together the basic building blocks of biomolecules. For this reason, the biosensor based on magnetoresistive technology was developed in order to test whether the magnetic markers are bonding to DNA produced by PCR (polymerase chain reaction). After removing the weakly bound magnetic beads, the remaining beads on the surface are counted with the signal change of the sensor, revealing the concentration of the analyte DNA in the sample (121). Further, several development steps have been done in order to achieve a high dense array with integrated microfluidics for a real time detection of hybridization. The detection of a single 2.8 μm magnetic bead from Dynal is possible by using two sensors, one for reference and the other for signal, combined in a Wheatstone bridge. An AC field was applied to magnetize the magnetic bead and to detect the resistance change of the sensor with a

lock-in amplifier (122). The future goals are oriented towards a fast and multiplexed detection of biological analytes. The dimension of a GMR sensor is 5 μm × 80 μm, and works in a current in plane configuration mode. The magnetic bead is magnetized using an AC magnetizing field (100 Oe at 200 Hz) in the z direction, so only the field from the bead will influence the sensor in so called x-direction (123). Thus, the experimental BARC sensor has a detection limit of 10 beads with a diameter of 2.8 μm, but the detection range is over three decades, owe to the large area of the sensor. The sensor is able to detect a single 4.35 μm NiFe bead (13). Considering the sensitivity of a biosensor array, it has to be taken into account the assay sensitivity and the detector sensitivity. The assay sensitivity is related to the biochemical sensitivity connected to the arrival time of the magnetic markers onto the sensor area. This feature is disadvantaged by the small dimensions of the sensor. But, when the magnetic labels are on the sensing area (using magnetic fluidics or electrochemical forces), the detector sensitivity (related to the detection of a small amount of magnetic field coming from the magnetic label) becomes important. Analytical calculations and finite elements simulations have been proceed in order to calculate the analyte transport limitations as a matter of sensors geometry, size and analyte concentration. It has been concluded that even if the small size sensors are suitable for sensitive detection heading towards single molecule experiments, the time for analyte transport would be too high. Considering this, large sensors are preferred because the analyte flux to the sensor can be increased through fluidic low. The assay sensitivity for small dimension sensors is affected by the transport in the fluidic systems, so even if the magnetic detection limit is low, the minimum concentration that could be detected would only be in the range of pM. From the authors' point of view, the sensitivity should be expressed as the minimum detectable concentration over a short period of time (124). Based on the previous findings, a GMR based biosensor has been developed, with a diameter of 100 μm that is able to detect protein in attomolar concentration by using semi-homogenous fluidic force discrimination assays. In this approach, the magnetic labels are first mixed with the target in a solution, and then distributed on the microarray, increasing the capture by 1000 fold when compared to laminar flow. Further, the nonspecifically bound beads are removed by laminar fluidic forces and the remaining beads are counted to determine the concentrations of the solution (125). In the development of a biosensor, the detection sensitivity, its selectivity and sensing time are the most important parameters that describe its

performance. By combining semi-homogenous and fluidic force discrimination assays it is possible to detect attomolar protein concentrations in 10 minutes using only two reagent mixtures and three assay steps.

5.1.5 Magnetic biosensors research at Brown University

The spintronic based sensors have been developed at the Brown University in order to achieve a very sensitive detection of small magnetic fields provided by the magnetic beads. The detection signal has been extracted by using an AC bridge configuration and lock-in technique. Two external magnetic fields in an in-plane and perpendicular configuration have been used to magnetically excite the magnetic bead and to have the sensor in its linear sensitive operation range. An AC voltage with a frequency of 8 kHz was applied on the 2 μm×6 μm tunneling magneto-resistance sensor with an Al_2O_3 barrier. By using finite elements simulation it has been calculated that the magnetic field provided by a 2.8 μm magnetic bead is 0.4 Oe when an external field of 15 Oe is applied. This magnetic field will induce a change of 0.15 % in the sensor resistance (126). By using the detection schemes described earlier it was possible to detect micrometer sized magnetic beads that were flowing over the sensor array through a microchannel. The next step in the magnetoresistive sensors developments has been done by integrating TMR sensors with MgO insulator as barrier material and to detect DNA target labeled with 50 nm MACS™ nanoparticles and 16 nm Fe_3O_4 nanoaparticles (127). In the biodetection of DNA hybridization, no microchannles have been used, being possible to detect 2.5 μM single strands DNA after hybridization process. The resistance change due to the presence of the magnetic field from the bead is varying with respect to the bead from 3% up to 6%.

5.1.6 Magnetic biosensors developed at Philips Research Laboratories

The authors achieved the detection of a single 2.8 μm bead attached to an AFM tip by colloid probe technique. The detection scheme include: GMR sensor with the dimension of 100 μm×3 μm and current wires of 0.35 μm wide. The current wires create the magnetic field to magnetize the superparamagnetic beads, so no external

magnetic field is needed. By scanning magnetic bead with the help of the AFM tip over the sensor surface it was possible to observe the magnetic influence of the bead over the GMR sensor with respect to different orientations of the bead relative to the sensor. The advantage of this sensing scheme relies in its simplicity, avoiding microchannels above the sensors or the difficulties given by the static dry measurements when the signal from the sensor has to be measured before placing the beads and after the bead's removal from the sensors surface. A disadvantage of this sensing scheme is given by the capacitive coupling that can appear between the current wires and the sensor. This could be avoided by modulating the current through the wires and the current passing through the sensor at different frequencies. Later on, microchannels have been integrated above the GMR sensors, and the magnetic detection of 300 nm magnetic beads has been performed with the help of an integrated micropatterned trench that was situated on top of the sensor. Several processes such as diffusion and sedimentation in the fluid have been also evaluated. The GMR sensors have been integrated in a Wheatstone bridge configuration and the external field to magnetize the magnetic labels was applied perpendicular to the sensor surface (128). The signal from the sensor has been proven to be proportional to the concentration of the nanoparticles in solution. The next step in magnetic label detection is their real time detection (129). The magnetic beads of 1 μm and 2.8 μm have been detected when passing by the sensor, being manipulated by two current wires situated on both sides of the sensor. No microchannels have been used in this case. It was possible to distinguish the signal coming from a bead situated at different positions relative to the sensor. By sensing the presence of the bead, by manipulating the bead and trace its positions it could be possible in the near future to probe functional information about molecules. Several approaches to analyze individual particles near a chip surface in low magnetic field and high field gradients have also been performed by the same group (130). A magnetophoretic analysis can be done if the particles diameter is in the range of 1 μm. If the nanoparticles diameter is decreasing, a confined Brownian motion analysis is desirable due to the diffusion forces that are higher for smaller particles. All these information regarding magnetic properties of the magnetic labels can be further used for their better integration in a lab-on-a-chip system.

5.1.7 Development of magnetoresistive sensors in Singapore and Shanghai

Some other groups working in the field of magnetoresistance detectors used spin valve or GMR sensors in order to see their response to various magnetic labels. Different magnetizations schemes have been used. A group from Singapore has tested the response of a spin valve sensor of an 8 μm bead that was scanned over the sensor surface by using an AFM tip. It has been concluded that the sensor response to the magnetic field of the bead depends on the magnetization direction of the bead (in plane or out-of-plane) and its orientation relative to the sensor (95). Several calculations have been performed for the improvement of the tunneling based magnetoresistance sensors. In those calculations, Co ferromagnetic nanoparticles have been used for detection, due to their high stray field and stability. Their magnetic properties are superior compared to superparamagnetic beads, making them a better candidate for biosensing applications. The influence of the ferromagnetic stray field over the sensor free layer gives information about the desired geometrical shape of the sensor for "*in vitro*" applications (131). By having accurate data about magnetic sensing of ferromagnetic nanoparticles, biosensors of high performance can be produced. Simulations regarding the employment of a magnetic shielded layer on top of the sensing layer predict an improvement in the magnetic detection of ferromagnetic nanoparticles (132). Another group from Shanghai has elaborated micromagnetic simulation for the detection of 250 nm magnetic labels modulated by AC magnetic fields. The results of the simulations conclude that the response of a linear spin valve sensor is proportional to the number of magnetic labels (133).

5.1.8 Development of magnetoresistive sensors at Nonvolatile Electronics

The research regarding the evolution of magnetoresistive sensors at Nonvolatile Electronics has started recently after the implementation of this idea. Firstly, a model for detection has been developed (96), where a single micron sized bead is able to be detected by a 1 μm×1 μm size GMR sensor. The conclusions of the simulations comprehend that a GMR sensor can detect a single paramagnetic bead of any size if the following conditions are accomplished:

(1) the sensor is at about the same size as the bead

(2) the bead surface is at 0.2 bead radii away from the sensor surface

(3) the bead has $\chi_m = 0.05$

(4) the GMR sensor response is adequate

The next step in the magnetoresistive biosensors applications was the integration of the GMR sensors in a Wheastone bridge and the integration of the entire detection assay in a microfluidic system (134). The dependence of the detected signal with the distance between the sensor and the magnetic label, has also been investigated highlighting the d^{-3} dependence (94). The same GMR sensor assay has been used for the detection of biotin-streptavidin binding with the help of 1μm magnetic beads (93) as well as for their use in immunosorbent assays by using a capture antibody surface compose of mouse IgG and magnetic nanoparticles modified with a layer of goat α-mouse IgG (135).

Table 5.1 Schematic overview regarding the development of magnetoresistive biosensors

	GMR				Spin valve				TMR			
	Nano size sensor	<15 nm nanoparticle detection	≥ 200nm particle detection	Biological sensing	Nano size sensor	<15 nm nanoparticle detection	≥200nm particle detection	Biological sensing	Nano size sensor	<15 nm nanoparticle detection	≥200nm particle detection	Biological sensing
Bielefeld University[1]			●	●					●	●	●	
Lisbon							●	●			●	●
Standford University						●	●			●		●
Naval Research			●	●								
Brown University										●	●	●
Philips			●									
Singapore, Shanghai			●									
Non-volatile Electronics			●	●								

[1]In Table 5.1 the results presented in this thesis are also included

5.2 Detection of MyOne magnetic beads by TMR sensors

Resuming the presented short overview of the work from the groups that have included the development of magnetoresistive sensors in their research program, it can be said that the overall attention is focused on developing sensors assays of high density with an increased biological and physical sensitivity. Continuing these ideas, it has already been presented in Chapter 3 the array of sensors that have been developed in this presented study. The lateral dimension of the sensors has been reduced to 100 nm ×400 nm. Their small size allows integration in a closed packed array, where 20 sensors are situated in an area 18.2 μm^2. The sensors have been employed in the detection of 1.05 μm MyOne magnetic beads from Dynal Biotech (136). The magnetic beads surface is functionalized with carboxylic acid (COOH) ending groups that give the hydrophobic characteristics of the bead surface. On top of the sensor surface is the Au conducting line that is needed for the outside connection of the element. The carboxylic acid interacts poorly with the gold surface, so the functionalized magnetic beads can be easily removed from the sensor area. The detection of magnetic labels can be achieved by magnetizing them in three different orientation of external magnetic field: in plane, out-of-plane, or a combination of both that gives a 45º angle magnetic field.

5.2.1 In plane detection of magnetic beads

General characteristics regarding in-plane detection

A detailed description will be given for the detection with an in-plane magnetic field. An external DC magnetic field is applied so as to rotate the top free layer of the tunneling sensor to change the amplitude of the tunneling magneto-resistance. Simultaneously, the applied field will magnetize the superparamagnetic bead, thus inducing a dipole as magnetic field. The strength of the dipole magnetic field depends on the magnitude of the applied field. If the magnetic bead is situated directly on top of the sensor, the magnetic dipole field will directly oppose the external field. Consequently, the magnetic field produced by the superparamagnetic bead will weakly decrease the strength of the external field. Since, the sensors have a linear TMR characteristics in this field, it can be roughly calculated the magnetic field produced by the superparamagnetic bead

by considering the sensor response. In the previously introduced models (96) it has been concluded that the magnetic field of the bead is:

$$H_{bead} = 0.05 \cdot H_{appl} \tag{5.6}$$

From the calculated values of the detection done with the MgO based tunneling magnetoresistive sensors for the 1 μm magnetic bead detection it has been pointed out that the magnetic field produced by the label is in the range of 1-10% of the applied field. The easiest method to detect the magnetic labels is by noticing the difference between the sensor output without the magnetic beads on top and with the magnetic beads situated on top of the sensors. The linear output of the sensor is of great advantage making the subtracting procedure between both output signals beads very facile. In the detection practice, two consecutive measurements of the sensors are done in their initial state. These measurements characterize the noise level of the sensor. By subtracting the resistance of these measurements for every sensor the limits of detection is known. If the signal from the magnetic bead would be within these limits, no detection would be possible. The next step is done by keeping the sensors in the same position and dropping the solution of diluted beads (1/10) in DI water with a handheld pipette on top of the sensors surface. The beads are dropped directly on the surface of the conducting lines, which have a thickness of 55 nm, that electrically contact the sensors. The underlying reason for this is to test the highest signal gained from the sensors in the presence of the beads to know in what range this signal should be classified. After the drop has dried, the sensor's output is measured with the presence of the beads on top. When the three measurements are finished, an SEM picture of the assay is taken to know the orientation of the beads relative to the sensors. Due to the small size of the sensors, an SEM imaging is necessary due to the lack in precision and resolution of the optical microscope in the submicrometer range. The next step in the detection procedure is removing the beads in ethanol solution in ultrasonic bath for about 5 minutes. The COOH coated magnetic beads are usually easily removed and the sensors can be further used for other detection measurements. The detection signal is obtained by subtracting the resistance of the bare sensor from the resistance of the sensor obtained after the measurements done with beads on top of the sensor surface. The bead detection signal is then compared with the noise signal of the sensor. When the bead signal is at a different level compared to the noise signal, the detection of the magnetic bead is confirmed. The detection signal varies with respect to the orientation direction and

distance of the bead towards the sensor. Computer simulations have been carried on (137) so as to characterize the magnetic stray field exhibited by a magnetic dipole as a function of the size of one bead. The micromagnetic simulations reveal the behavior of the magnetoresistance sensor when the two ferromagnetic layers that are separated by a tunneling barrier are in parallel orientation and detailed information regarding them will further be given. The experimental data are taken over a sweeping field from -500 to + 500 Oe range, when the two ferromagnetic layers are in both the parallel and the antiparallel state. Because the bead exhibits superparamagnetic properties it should carry a magnetic moment only when it is induced by a magnetic field. Thus, when no external magnetic field is applied, the response of the sensor to the magnetic field of the bead should be at the noise level. When a signal from the magnetic bead is present although no external magnetic field is applied, the magnetic bead is magnetized by the top ferromagnetic free layer of the sensor. A very weak interaction between the top sensor layer and superparamagnetic bead can here not ne neglected when the magnetic bead is situated exactly on top of the sensor surface.

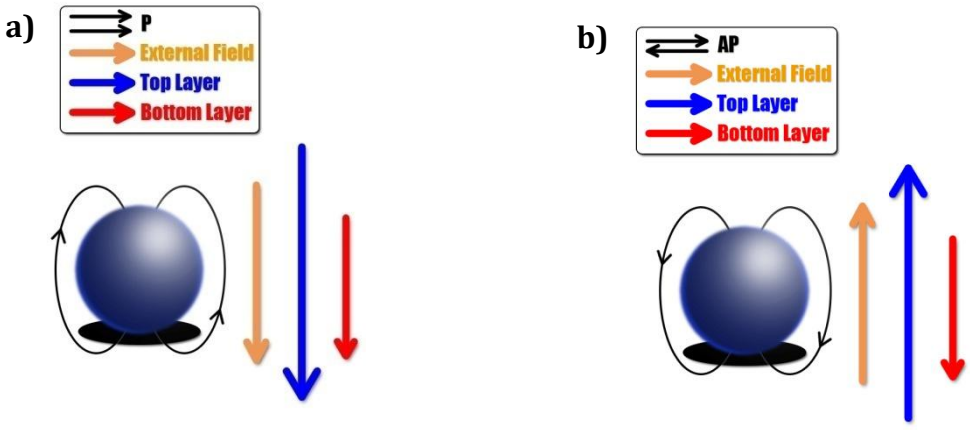

Fig. 5.2 (a) Orientation of the magnetization for the top and bottom layer when the two are in a parallel orientation (b) Orientation of the magnetization for the top and bottom layer when the two are in an antiparallel orientation

Figure 5.2 displays the orientation of the magnetization for the bottom and top layer with respect to the direction of the external magnetic field that is directing the parallel or antiparallel alignment. The orientation of the field lines corresponding to the dipole type magnetic field of the bead is also indicated. The orientation of the bottom ferro-

magnetic layer stays fixed in one direction, the top layer being free to rotate and change the value of the resistance corresponding to parallel or antiparallel orientation. This sketch gives a suggestion related to the correlation between the external magnetic field orientation, top and bottom ferromagnetic layers magnetization orientation and stray field of the magnetic bead. This can be useful in understanding the influence the magnetic field of the bead has on changing the resistance of TMR sensors.

Correlation between bead orientation and detected signal

During the in-plane detection mode of magnetic beads their dipole field can increase or decrease the strength of the external applied field in correlation with the bead orientation relative to the sensor. Applying the external field along the hard axis of the element y, the in-plane component of the magnetic stray field of the bead has been calculated from equation (5.1) and is given in Fig. 5.3.

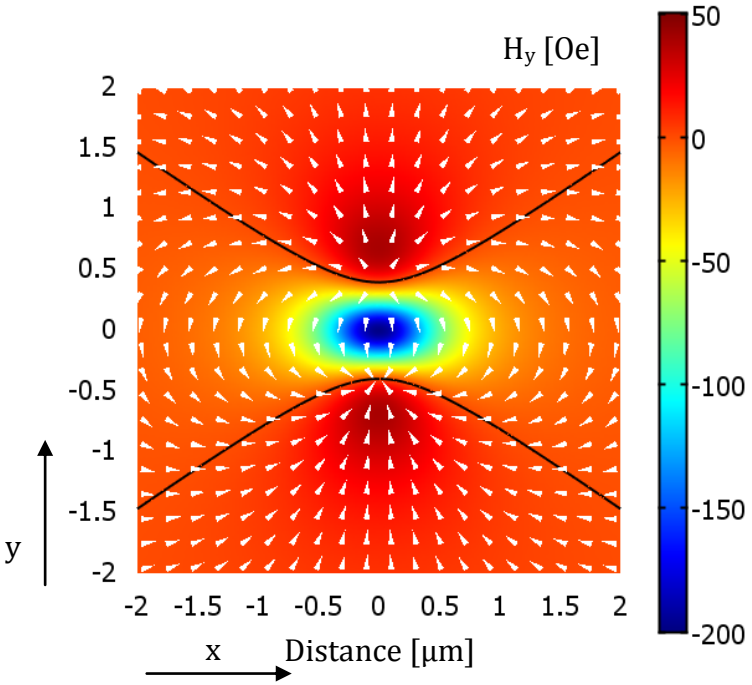

Fig. 5.3 in plane magnetic field of a bead with magnetic moment aligned parallel with the hard axis. The black lines indicates the component value Hy=0 which separates the areas where $Hy > 0$ (top and bottom) and $Hy < 0$ (center) from each other (given by A. Weddemann (137))

By taking this into account it is expected to sense a different signal with respect to the orientation of the magnetized bead relative to the sensor. If the sensor is situated in the $Hy < 0$ area, the direction of magnetization of free electrode experiences a torque, tending to orient both electrodes antiparallel to each other. The tendency to an

antiparallel orientation configuration of the electrodes means that the stray field of the magnetic bead will weaken the external applied field. In a similar way, if the sensor is situated in the area Hy > 0, the torque tends to orientate the two ferromagnetic electrodes parallel to each other, thus the stray field provided by the bead will enhance the external field.

Figure 5.4 exemplifies the detection case where the sensor is situated in the Hy < 0 area. By plotting the resistances of the sensor with and without beads in the same graph (Fig. 5.4 a) it is observed that the presence of the bead decreases the sensor resistance when the two ferromagnetic electrodes are antiparallel.

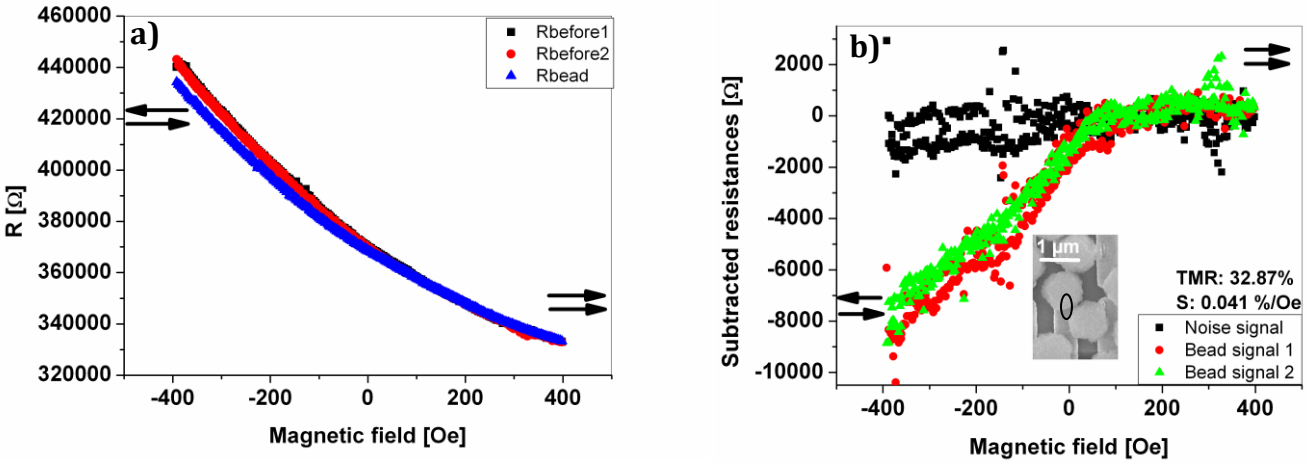

Fig. 5.4 (a) Resistance change of the sensor when the sensor is situated in the $Hy < 0$ region of the in plane component of the magnetic bead stray field (b) Detection signal obtained from the subtracted resistances of the sensor when the bead is situated in the $Hy < 0$ region; the inset represent the experimental situation

This means that the external applied field is weakened by the presence of the superparamagnetic bead. The same graph shows that the presence of the bead is increasing the resistance of the sensor when the two ferromagnetic electrodes are parallel oriented and on the other hand the stray field from the magnetic bead weakens the applied external field. Figure 5.4 b represents the subtracted resistances data for the detection case presented in Fig. 5.4a. In this representation, the Noise signal $=R_{before1}-R_{before2,}$ while Bead signal $1=R_{bead}-R_{before1}$ and Bead signal $2= R_{bead}-R_{before1.}$ The inset from Fig. 5.4b shows the experimental situation of the bead arrangement around the sensor. It can be seen that there are two magnetic particles oriented along the longitudinal axis

of the sensor. Thus the sensor is situated in the Hy < 0 region of the magnetic beads stray field presented in Fig. 5.3.

Figure 5.5 shows the detection case which reveals a reversed situation, where the sensor is situated in the Hy > 0 area of the magnetic bead stray field. When the two ferromagnetic electrodes are in an antiparallel orientation, the presence of the bead increases the resistance of the sensor. So, the stray field from the magnetic bead enhances the magnetic field at the site of the sensor. In the parallel orientation of the two ferromagnetic electrodes, the resistance of the sensor is decreased due to the presence of the bead, so its stray field enhances the overall field at the sensor position. In the inset the experimental bead arrangement reveals the orientation of the sensor in the Hy > 0 area of the magnetic bead stray field.

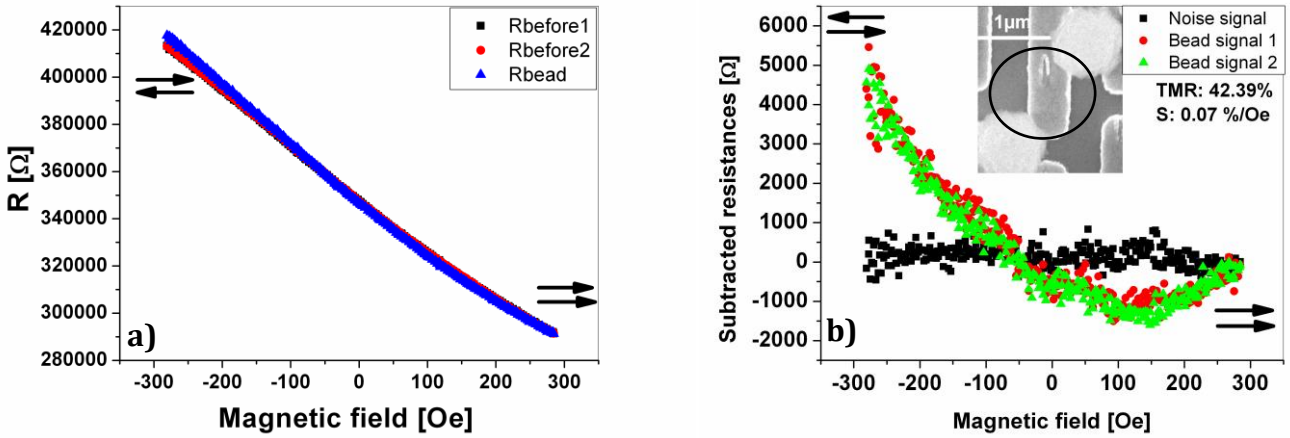

Fig. 5.5 (a) Resistance change of the sensor when it is situated in the $Hy > 0$ region of the magnetic bead stray field (b) Detection signal obtained from the subtracted resistances when the sensor is situated in the $Hy > 0$ region; the inset present the experimental situation.

The results of detection can be interpreted also by considering the radial and angular components expressed in equations (5.4) and (5.5). Taking these equations into account it can be seen that the angle between $\hat{m}$ and $\hat{r}$ is $\pi/2$ when the magnetic bead is situated on top of the senor area. This corresponds to the case when the sensor is in the Hy < 0 region of the magnetic bead stray field presented in Fig. 5.3. When the angle between $\hat{m}$ and $\hat{r}$ is increasing and approaching the π value, this corresponds to the situation when the sensor is situated in the area where Hy > 0. In this case $\cos\pi = -1$, the external magnetic field that acts on the sensor will be enhanced by the presence of the bead's stray field.

In order to have an accurate understanding of magnetic detection, micromagnetic simulations on a trilayer model CoFeB(4nm)/MgO(2nm)/CoFeB(4nm) were carried out. Because the area of TMR elements is in the submicrometer range (100 nm×400 nm), their stray field starts to have an important role. Under the influence of the stray field coupling, an antiparallel alignment of the two ferromagnetic layers is facilitated. Another coupling mechanism between the two ferromagnetic layers is given by the surface roughness spacer, also known as Néel coupling. Having an opposite effect, the Néel coupling encourage a parallel alignment of the two ferromagnetic layers. By considering both a TMR map is simulated by a finite element approach. The ΔTMR express the change in percentage due to the influence of the stray field of the bead:

$$\Delta\mathrm{TMR} = \frac{R_{bead+sensor} - R_{sensor}}{R_{sensor}} \%, \qquad (5.7)$$

where $R_{bead+sensor}$ represents the resistance of the sensor with the bead on top and R_{sensor} denotes the resistance of the bare sensor.

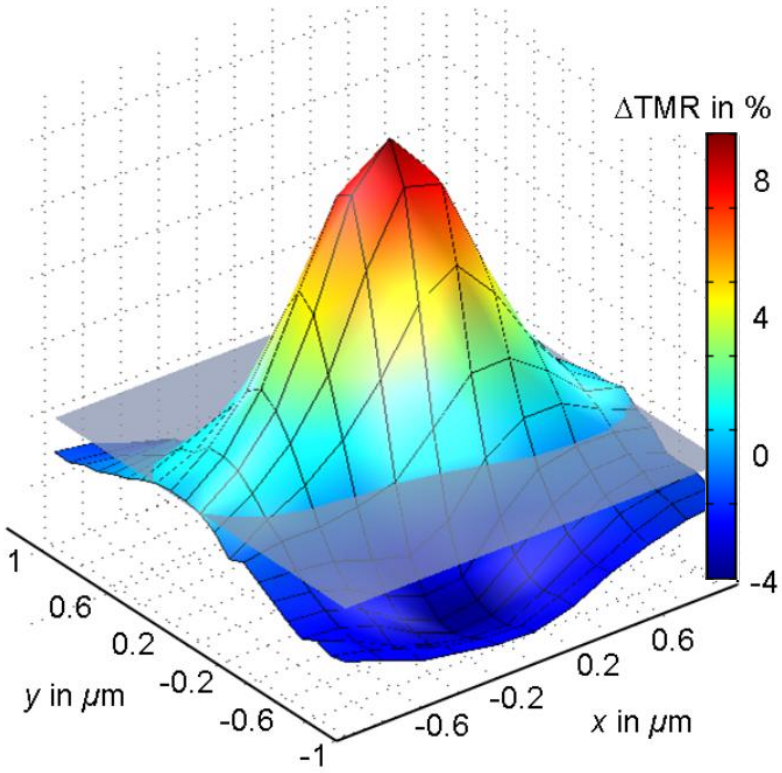

Fig. 5. 6 ΔTMR values map for particle positions; the map has been calculated for the case when the two ferromagnetic layers are having a parallel orientation, the gray level separates positive from negative values (given by (137))

Observing the ΔTMR map one can deduce that different detection schemes can occur. In the following paragraphs a comparison between experimental and simulation data will be performed.

Beads situated along the longitudinal axis of the sensor (Hy < 0)

The first detection scheme that will be analyzed is the influence of the magnetic bead's stray field when it is situated about the longitudinal axis of the sensor, so the sensor is situated in the in the Hy < 0 region of the magnetic bead stray field**.** One situation is when the bead is positioned exactly on top of the sensor, so the entire fringe field of the bead will influence the top free layer of the sensor. In another situation, the bead is positioned in different orientations and distances about the longitudinal axis. A third situation is when an additional bead is affecting the sensor from its transversal side. In this case, when the orientation of the two ferromagnetic layers of the electrode is parallel, the stray field of the bead situated in the longitudinal direction will act towards external field weakening, but the stray field of the bead positioned along the latitudinal side of the sensor tends to enhance the external applied field. Due to this, the detected signal will be merged with the noise signal.

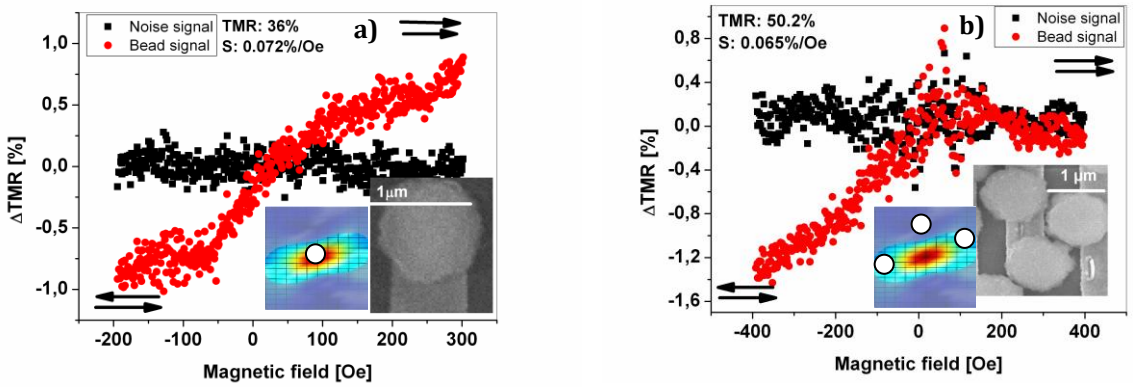

Fig. 5. 7 (a) Detection of the bead positioned on top of the sensor (b) Detection of the two beads situated along the longitudinal axis and one bead along the lateral side of the sensor; the insets present the SEM image of the experimental situation as well as the top view of the ΔTMR map with the white circles standing for bead positions

Figure 5.8a shows detection situation where two beads very close to each other are situated along the longitudinal axis of the sensor, so their net magnetic moment will be zero, because they will cancel each other's magnetic moment. An opposite situation is presented in Fig. 5.8b where two separate beads are positioned at 1.75 μm away from

the sensor in the longitudinal axis. In this case, the beads will merge their magnetic moment and will magnetically affect the sensor.

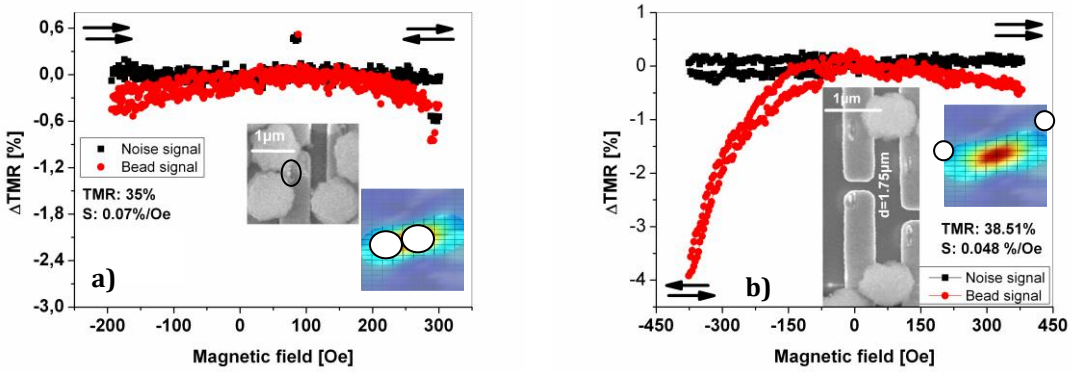

Fig. 5. 8 (a) Detection of two beads that are canceling each other signal (b) Detection of two beads situated along the longitudinal axis of the sensor; the insets present the SEM image of the experimental situation as well as the top view of the ΔTMR map with the white circles standing for bead positions

Beads situated along the short axis of the sensor (Hy > 0)

The magnetic bead dipole field will enhance the applied external magnetic field when the bead is situated along the short axis of the sensor, so the sensor is situated in the $Hy > 0$ region of the stray field of the bead. One detection case (Fig. 5.9 a) presents the situation when one magnetic bead is situated along the short axis of the sensor and another bead is placed a bit further away along the longitudinal axis of the sensor. Thus, the stray field of both beads will affect the sensor and the combined signal will tend to be merged with the noise level. Another case (Fig. 5.9 b) identifies a situation where the beads will influence the sensor only from its transversal side. The resistance of the sensor will decrease when the two ferromagnetic layers of the sensor are in a parallel orientation, and hence the signal will be in the negative range.

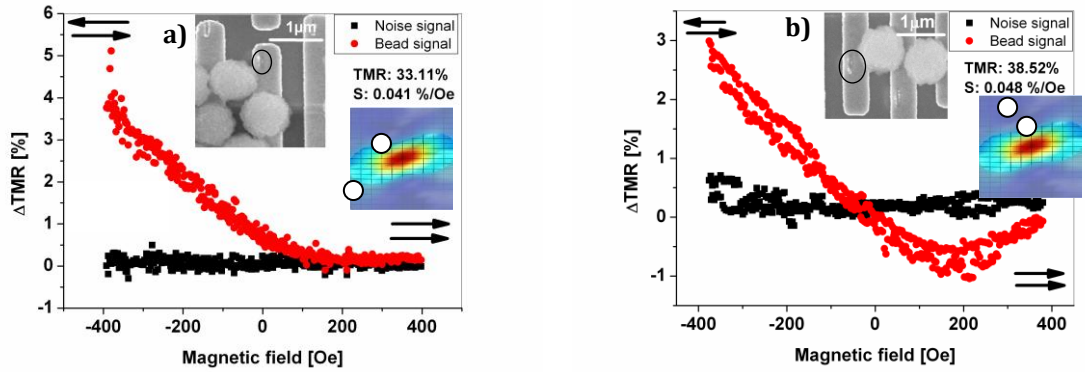

Fig. 5. 9 (a) Detection of one bead along the short axis of the sensor and situated along the longitudinal axis of the sensor (b) Detection of two beads situated along the short axis of the sensor; the insets present the SEM image of the experimental situation as well as the top view of the ΔTMR map with the white circles standing for bead positions

Figure 5.10a summarizes an example when two magnetic beads will cancel each other's signal because they are positioned very close to each other along the transversal axis of the sensor. When the magnetic bead is at a distance larger than 1.8 µm (Fig. 5.10b) away from the sensor its stray field is too weak to be seen by the TMR sensor.

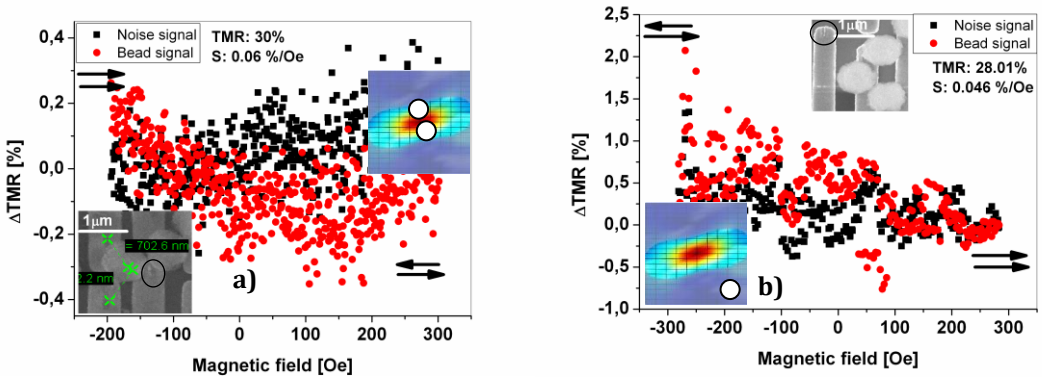

Fig. 5. 10 (a) Detection of two beads that are canceling each other signal along the short axis of the sensor (b) Non-detection of one bead situated at a distance of 1.8 µm away along the short axis of the sensor; the insets present the SEM image of the experimental situation as well as the top view of the ΔTMR map with the white circles standing for bead positions

Conclusions and future perspectives regarding the sensitive detection of 1 micrometer magnetic beads

Based on the bead detection in all situations described above it can be concluded that downscaling the size of the magnetoresistive sensors in the nanometers range allowed accurately detecting the stray field of one magnetic microbead. It was possible to observe a distinct detection signal with respect to the orientation of the bead relative to the sensor plane. This distinguished behavior has been theoretically predicted and is related to the asymmetry exhibited by the stray field of the bead in the in-plane projection. In addition, it has been revealed that two or more magnetoresistive sensors can simultaneously detect the signal from one magnetic bead. Consequently, this gives rise to an idea to monitor the magnetic bead trajectory through an array of sensors by sensing its stray field contributions with different sensors nearby its path. Subsequently, the exact position of the bead will be known. Potential biological applications from this "magnetic tracking" of magnetic beads are multiple. Until now the molecular mechanism by which individual cell recognizes and respond to external forces is not fully understood. Very little is known about how cells convert mechanical signal into a chemical response (138). The significance of this cell feature comes along with the fact that the mechanotransduction mechanism is set on the basis of all sensoric functions of the body such as: touch, hearing, baroreception, gravity sensation and others (139). It is established that the activation of signaling molecules inside the cell is mediated through changes in the cytoskeleton. The internal cytoskeleton is formed from an interconnected network of actimyosin microfilaments, microtubules which are hollow nanoscale biopolymers and intermediate filaments that link the nucleus to the surface adhesion receptors (140), (141) . The most suitable cell model is the one that describes it as the prestressed tensegrity structure. Within this model, the cell has the property to maintain its shape stability within an applied tensed force. By developing a magnetoresistive microscope, the modification of the cytoskeleton structure could be detected by the MR sensors via a magnetic bead.

During the past years, the biologists discovered that organogenesis and pattern formation is governed by genes controling the developmental signaling pathways. It is not yet known how nature builds tissues with specialized form and function. During the

studies of cancer cells it has been determined that the tissue form and geometry may give a feed back to control cell proliferation by concentrating stress at particular sites and mechanically restructuring the actin cytoskeleton inside cells within this area. So, the study of cytoskeleton movements and its response to mechanical forces applied to the cell with the help of a MR microscope may lead to the discovery of basic phenomena that constitute life precursors (142).

5.2.2 Out-of-plane and 45° angle detection of magnetic beads

A magnetic bead can also be magnetized with an out-of-plane magnetic field. The advantage of a z type of external field relies on the fact that it doesn't affect the MR sensors response because the sensors are sensitive only in the direction of the x axis. So, the magnitude of the out-of-plane magnetic field can be very large and the magnetic moment of the bead can approach the saturation while the sensors are still in the linear range. Nevertheless, in plane components of the stray field of the magnetic bead allow for a similar response as if the external field is applied in the in-plane direction. Another case of detection is a superposition of the two types of external field (in plane and out-of-plane) resulting in an 45° angle of the applied magnetic field. When the magnetic bead is magnetized in the y direction, the B_x component of the magnetic field will have the following form:

$$B_x = \frac{\mu_0}{4\pi} \frac{3mxy}{(x^2+y^2+z^2)^{5/2}} \tag{5.8}$$

In a very similar way, when the magnetic bead is magnetized by an out-of-plane magnetic field in the z direction, the x component of the magnetic bead's stray field will have the following configuration:

$$B_x = \frac{\mu_0}{4\pi} \frac{3mxz}{(x^2+y^2+z^2)^{5/2}} \tag{5.9}$$

Figure 5.11 presents the angle and out-of-plane detection results for a 1 μm magnetic bead.

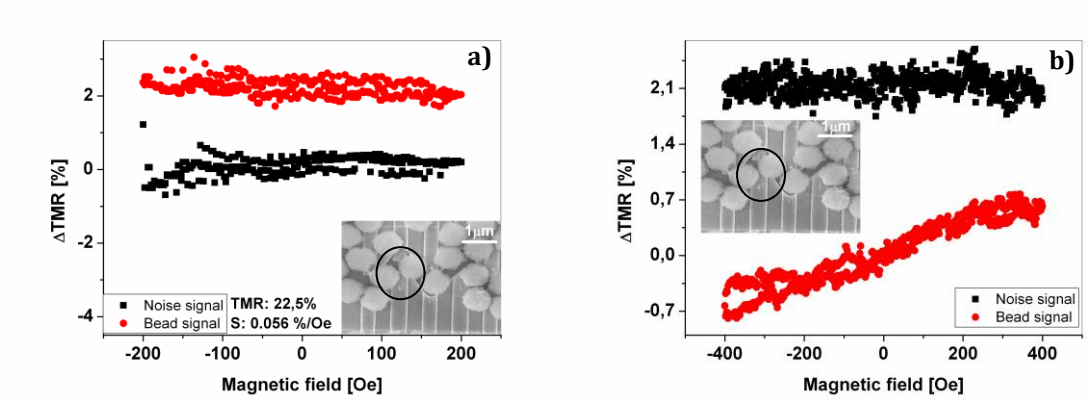

Fig. 5.11 (a) Example of out-of-plane detection of magnetic bead (b) Example of 45° angle detection of magnetic bead

After the subtraction of the sensor resistance for the three types of measurements (1) before placing the beads, (2) with the beads and (3) after removing the beads from the sensor's surface, the resulting bead and noise signal are at different levels. One reason for this observed mismatch could be the field set-up. Very likely, the magnetic coil in these experiments did not provide a homogenous field, so artifacts are present in the measured signals. This might lead to the misfit observed in the subtraction data. However, the angle and out-of-plane measurements of magnetic beads provides data where the bead signal does not match the noise level, as it is expected when no external magnetic field is applied on the superparamagnetic bead.

5.3 In-plane detection of magnetic nanoparticles

In order to determine the sensitivity of the TMR biosensors, superparamagnetic nanoparticles were used as test objects. Details regarding the physical properties of magnetic nanoparticles can be found in the first chapter of the thesis. The basic detection schemes and acquisition set-ups is the same as the one used for the in plane detection of magnetic beads. Magnetic cobalt nanoparticles characterized by a diameter of 14 nm are diluted 2:10 in 2'propanol solution.

Considering the small size of the nanoparticles relative to the size of the sensor, it is expected to detect the entire stray field of the nanoparticles. This brings up another

problem because the superposition of magnetic stray fields of many nanoparticles has to be taken into account.

The detection of magnetic nanoparticles can be divided into two separated situations which involve the number of Co nanoparticles on the sensor area for discrimination. The first situation is considered for monodispersed Co nanoparticles over the sensor area. The detected signal can be correlated to the single magnetic bead detection because the nanoparticles are arranged on the sensor area without magnetostatic interaction, therefore their entire stray field of the bead is captured by the sensor (Fig. 5.7a). This corresponds to the detection case of $Hy < 0$ from Fig. 5.3. In the second case, as the number of nanoparticles situated on the sensor area is increasing, their dipole coupling fields will lead to a collective nanoparticle interaction and the detected magnetic signal will exhibit a hysteresis.

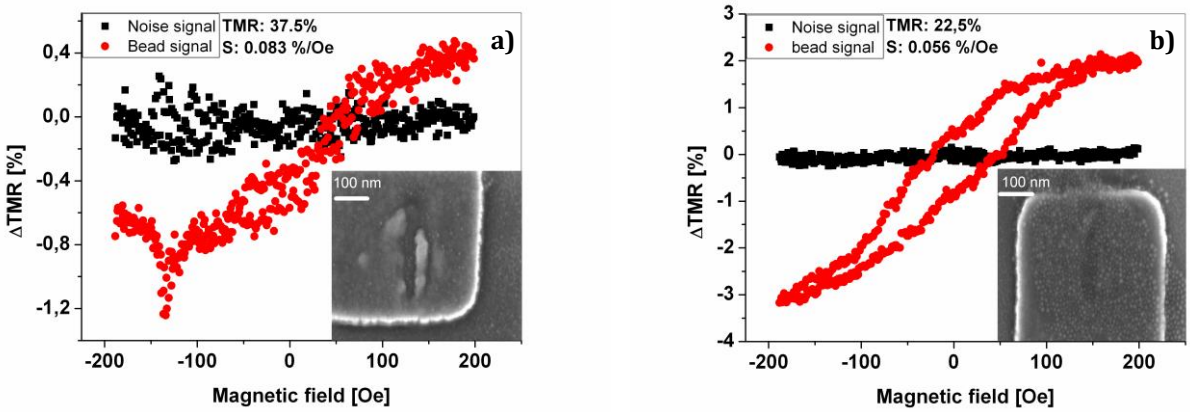

Fig. 5. 12 (a) Detection of monodispersed 14 nm Co nanoparticles (b) Detection of interacting 14 nm Co nanoparticles

The detection results in Fig. 5. 12b are correlated with AGM (alternating gradient magnetometer) measurements carried out on a monolayer of Co nanoparticles. For the AGM evaluation, the magnetic nanoparticles are dropped to form a monolayer and their magnetic properties are evaluated. In Fig. 5.13a typical AGM magnetic response of a monolayer of nanoparticles is given. It can be seen that they exhibit a coercitive field of 47 Oe. The same coercitive field value measured with the AGM measurement set-up is seen in the TMR sensors, indicating the strength of coupling fields between the nanoparticles. The interaction between nanoparticles should give rise to the same magnetic response irrespective to the type of magnetic measurements being performed. The connection observed between the two types of measurements

demonstrates the application of magnetoresistive sensors as a powerful tool for accurate magnetic measurements as well.

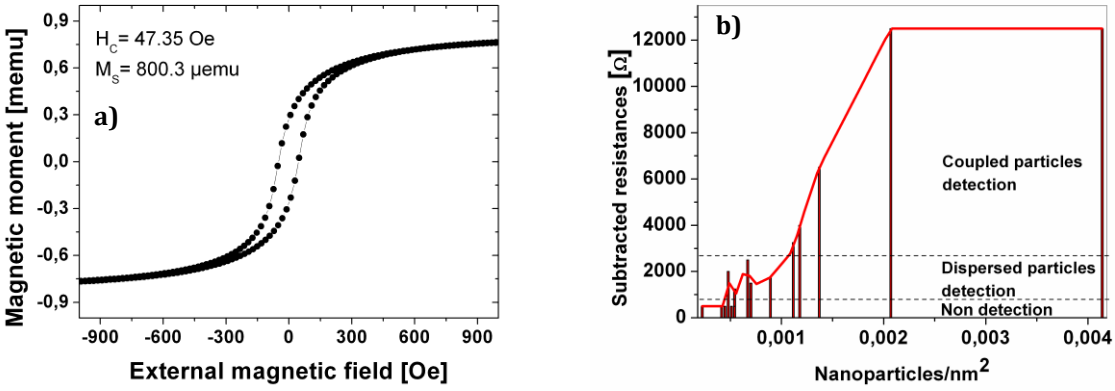

Fig. 5. 13 (a) AGM measurements of 14 nm Co nanoparticles (b) Statistic regarding detection of 14 nm Co nanoparticles

More importantly, the tunneling magnetoresistive sensors are capable to make a distinction between monodispersed and coupled nanoparticles, by exhibiting a non-hysteretic or a hysteretic signal. It has experimentally been confirmed that the signal of nanoparticles is stronger if they are positioned in the center of the sensor area. If the nanoparticles are situated in a big cluster on one of the lateral sides of the sensor, an inversion of the signal is observed. Due to the fact that a large number of nanoparticles are situated in the $Hy > 0$ area. If only a reduced number of monodispersed nanoparticles is situated onto the sensor area, the detected signal cannot be distinguished from the noise signal, because the magnetic signal from the nanoparticles is too low. In the figures that will be presented below can be observed that the detected signal depends on the orientation of the coupled nanoparticles towards the long or short axis of the sensor.

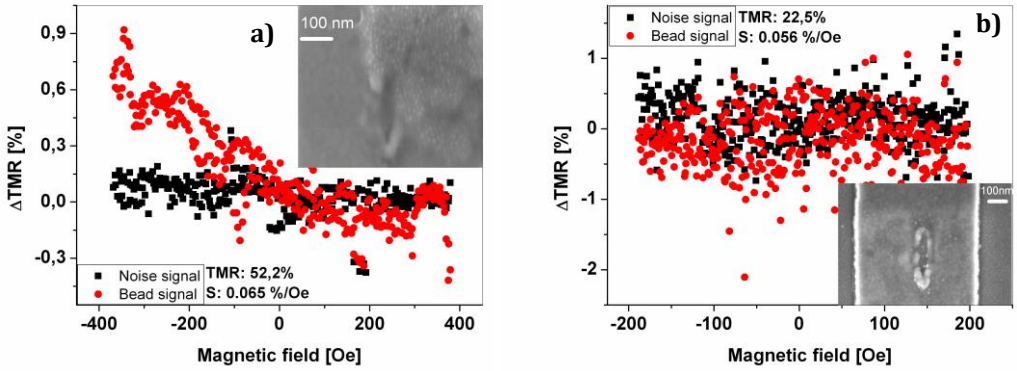

Fig. 5.14 (a) Detection of magnetic nanoparticles influencing the sensor from its transversal axis (b) Non-detection of magnetic nanoparticles owe to their reduced number on the sensor area

In order to test the sensing limits, detection of 9.4 nm CoFe nanoparticles has been performed. The magnetic moment of CoFe nanoparticles is very small due to a reduction upon oxisation in atmospheric conditions (29). Thus, their magnetic stray field cannot influence the rotation of the free top layer of the tunneling magnetoresitive sensor anymore.

Conclusions and future perspectives related to the detection of magnetic nanoparticles

The downscaling of the sensors to submicron dimensions in order to detect a reduced number of magnetic nanoparticles about a size of 10 nm was required. This could have been also anticipated if we bear in mind that the magnetic stray field of the magnetic bead or nanoparticles have similar physical characteristics. The minimum number of 14 nm magnetic nanoparticles as a detection limit has been determined to 16. One main condition for their detection is their arrangement in the center of the sensor. If a number of 12 magnetic nanoparticles are evenly distributed over the sensor area, their detection is not possible. The biological application of magnetic nanoparticles detection can be identified for the field of single molecule dynamics. In this field time resolved spectroscopy and near field optics methods are commonly used and is possible to probe dynamical processes such as molecular motions and chemical rotations at a single molecule level (143). The fluorescence single molecule detection and single molecule spectroscopy methods can be used to localize molecules within few

tens of nm. The future expectations of molecular biology include local, dynamic structural information of one biomolecule and the visualization of molecules dynamics in parallel (144). Furthermore, the localization of interaction between single biomacromolecules is addressed (145). By combining centroid localization analysis with the photobleaching of single fluorophores, single fluorescent molecules that are 8 nm apart can be seen with a 2.5 nm resolution in fluorescence microscopy (146). Probing the interaction between two different molecules would be a different option for magnetoresistive microscopy where the distance between two sensors is in the few hundred nanometers range. By attaching a reduced number, up to 20, of magnetic nanoparticles to a biomolecule, it could be possible to sense the movement and interaction of two biomolecules within a resolution of 1 nm. The trajectory of one biomolecule can be detected with the aid of three or four adjacent sensors that are detecting different signals with respect to the orientation of the biomolecule towards the sensor. If two or more biomolecules would agglomerate, the detected signal changes, exhibiting a hysteresis due to the dipolar coupling between nanoparticles.

Tunneling magnetoresistance microscopy could facilitate the achievement of challenges from biomolecular field if dynamic detection of magnetic beads and nanoparticles is accomplished. The next chapter will present improvements concerning dynamic detection of magnetic markers.

6. Dynamic magnetic detection by tunneling magnetoresistive sensors

The previous chapter describes the static detection of magnetic markers of different dimensions by means of various configurations of external magnetic fields. The next challenge for tunneling magnetoresistive sensors is to detect the movement of magnetic markers over the sensors. Dynamic detection of magnetic beads is a basic requirement for biological applications. In order to achieve dynamic detection, several sensors have to be measured simultaneously to sense the movement of biological molecule above the sensors. Processes like biorecognition, force bonding between two biomolecules, the motion of a biomolecule, interaction between two biomolecules and many others can be monitored only by means of active detection of magnetic markers. Details regarding the measurement set-up specialy designed for dynamic measurements can be found in (147). This measurement set-up is able to measure 8 sensor elements simultaneously. The magnetic transport measurements are performed by applying a bias voltage of 50 mV from a battery supply. The tunneling current is measured with operational amplifiers. Different experimental approaches have been tested so as to achieve a dynamical detection of moving particles. Some of them will be briefly discussed. During the experiments several difficulties have been encountered. Some of them were solved, but others are still remaining and possible experimental solutions will be addressed.

The combined system, sensors and electronics has been tested by a “magnetic pendulum”. One macroscopic magnet was oscillating above sensor array and the corresponding sensor characteristics were recorded.

Figure 6.1 allows determining the oscillation period of the “macroscopic bead”. The intensity of the magnetic field from the “macroscopic bead” at different heights was measured with a Gaussmeter (148). The magnetic field values measured by the Gaussmeter correspond with the values obtained from the TMR recording. As conclusions to “macroscopic bead” experiments one can observe that the tunneling magnetoresistive sensors sensitivity in magnetic field detection is comparable with the one of the Hall probe. From the dynamic detection of the “macroscopic bead” magnetic pendulum,

time resolution of the measurement set-up designed for dynamic measurements can be observed.

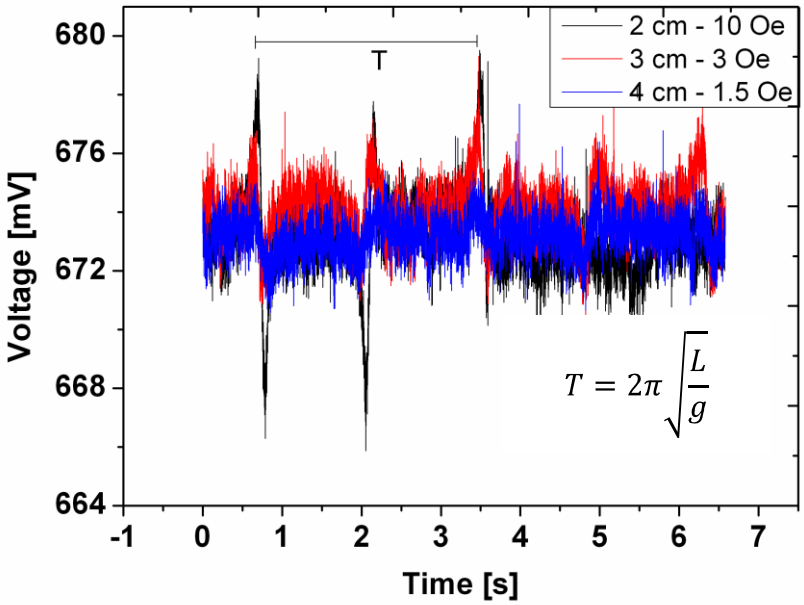

Fig. 6.1 Dynamic detection of a "macroscopic bead" that oscilates at different heights above the array of sensors

In order to analyze the new measurement set-up sensitivity, static detection of magnetic beads has been carried out. This experiment provides information regarding the maximum signal level that can be recorded from a magnetic bead. The test has been accomplished after the evaporation of the bead solution that was placed on top of the sensors. The sensor array prepared for dynamic detection is complied with additional lithographic steps that are increasing the distance between the sensor and the magnetic bead. Firstly, an extra layer of 100 nm of tantalum oxide is sputtered to electrically isolate the conducting lines that are contacting the sensor from the magnetic field manipulation lines that are used to attract the magnetic beads on top of the sensor's surface. By considering this, the minimum distance between the top layer of the sensor and the surface of the magnetic bead is of 212 nm. The static measurements presented in Chapter 5 have been achieved at a distance of 62 nm between the free ferromagnetic layer of the sensor and the surface of the superparamagnetic bead. The magnetic bead exhibits a magnetic field of 19% of the external field when the distance between the

sensing layer and the center of the magnetic bead is of 562 nm. The same magnetic bead will exhibit a magnetic field of only 4% from the applied external magnetic when the separation between the top layer and bead center is increased to 750 nm. Figure 6.2 reveals how the intensity of the detected signal decreases as the distance between the sensor and the magnetic bead is increased. A distance of 750 nm between the sensing layer and bead's center is considered to be the detection limit of the TMR sensors downscaled to submicron dimensions.

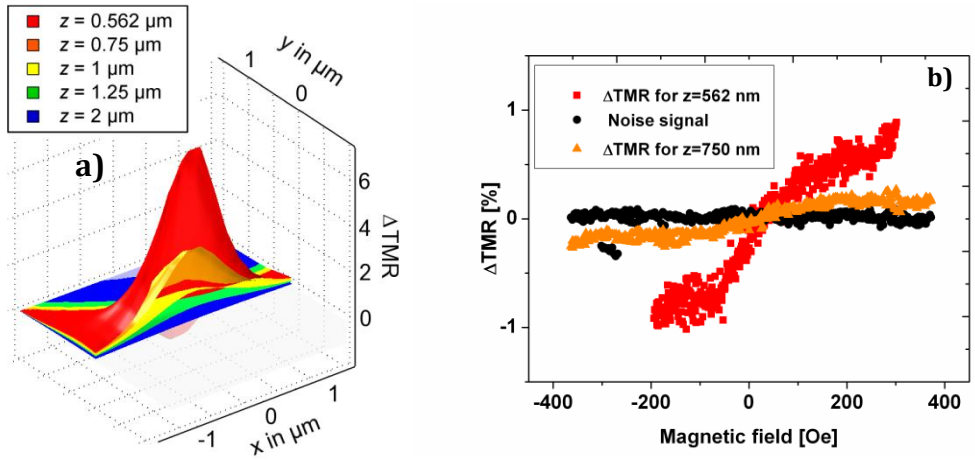

Fig. 6.2 a) Simulation map regarding the signal dependence on the height of the bead above the sensor area b) Signal from the magnetic bead situated at different height above the sensor, in the z value is included the bead radius of 500 nm

A comparison for static measurements between the measurements set-up used for static in-plane detection presented in Chapter 5 and the acquisition set-up designed for dynamic measurements is displayed in Fig. 6.3.

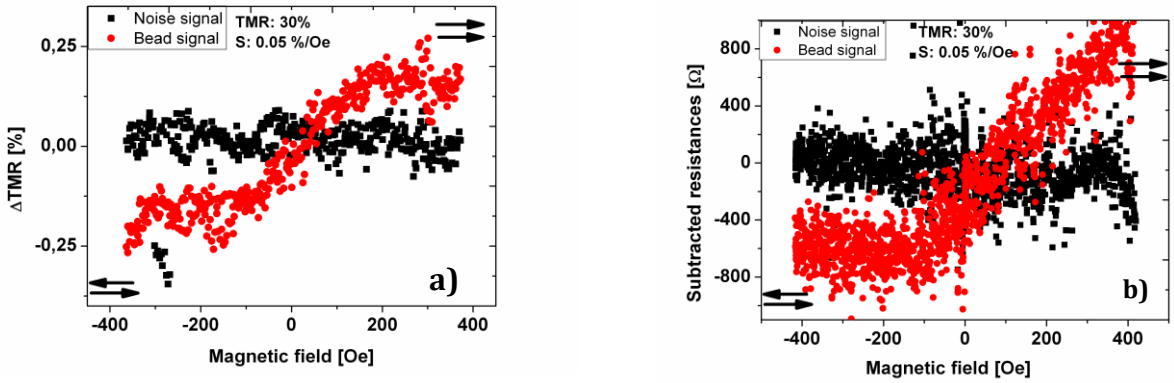

Fig. 6.3 Comparison of static measurements of magnetic beads between the standard set-up (a) and the set-up design for dynamic measurements (b)

The detection of magnetic beads in motion is more difficult to accomplish due to two main reasons: (1) the presence of magnetic beads in solution increases the distance between the sensor and the bead and (2) the rapid movement of the magnetic beads above the sensor surface. In order to decrease the distance between the TMR sensor and magnetic bead, the following options have been approached: (1) employ the detection of larger magnetic beads and (2) fabrication of microcrochannels above the sensor array. The movement and the speed of the magnetic beads can be controlled by the magnetic field manipulation lines.

The detection of 1 μm diameter MyOne Dynal magnetic beads and 3 μm diameter magnetic beads diluted in 1:10, 1:50 or 1:100 water solution has been attempted. Their magnetic detection has been tested by considering their Brownian movement in the liquid above the sensors. Several varieties of external magnetic fields have been applied to magnetize the magnetic beads: an in-plane magnetic field of 300 Oe, an out-of-plane magnetic field provided by a permanent magnet situated below the sensors and a combination of the two types of magnetic field. No signal from the magnetic beads has been intercepted by the measurement set-up. The non-detection is associated with the increased height between the sensors and the magnetic markers.

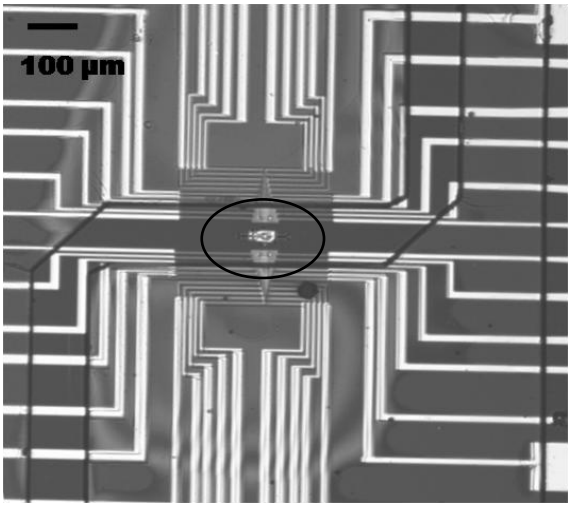

Fig. 6.4 Microchannel construction above the sensor arrays

With the intention of guiding magnetic beads closer to the sensor surface, so the influence of the water to be negligible, microchannels have been constructed on top of the sensors surface. The microchannels are built by using parallel lithography, from a special polymer called SU-8 and have a thickness of approximately 20 μm (149). Details regarding the applicability of microchannels in the lab-on-a-chip systems can be found in (150), (151), (152), (153), (154), (155), (156), (157). An image of the sensor array with the constructed microchannels on top is shown in Fig. 6.4. By considering such an approach the magnetic beads flow will be directed over the sensors surface. In the image is highlighted the area where are situated two separated arrays of sensors. Dynam-

ic detection with microchannels has been tested by using additional external out-of-plane magnetic field of 300 Oe. The set-up for dynamic detection is meant to measure sensors bonded in an IC socket. For dynamic detection of the magnetic markers, the socket has to be placed under an optical microscope to visualize the detection moment when the beads were passing over the sensors area. By these means, the optical detection of the beads movement can be correlated with the magnetotransport measurements of the sensors. In this stage of measurements, several problems have been encountered. The noise signal of the sensors increases because of the interferences between the sensors measurement set-up and the electrical components of the optical microscope. To avoid this, a metal case was built, so the sensors were shielded from the outside electrical sources. Due to the multitude of equipments that have to be used simultaneously and to the interaction between them is very difficult to achieve a clear signal coming from the bead. Another encountered problem is the unexpected breakdown of the sensors. Several models have been proposed to elucidate the physical reason for the dielectric breakdown of the tunneling magnetoresistive elements. The most suitable model for MgO based MTJ's is the E-model, which relates the breakdown to field-induced displacement of atomic bonds in the oxide barrier (158). The sensors elements used throughout the work of this thesis have a high resistance, so the presence of an external charge in the near vicinity of the arrays is providing a sufficient electrostatic field to "break" the sensors.

A different approach used for dynamic bead detection is the integration of magnetic field manipulating lines on top of the sensors. Figure 6.5a illustrates the construction of the lines used to control the bead movement. When a current is applied through one line, the beads are moving towards that line, being guided by the magnetic field induced by the electric current. By switching on the current to the other line, the beads will change their direction and move towards the second induced magnetic field. Different magnetic field line designs have been proposed with respect to their applicability. The design for bond force measurements is pictured in Fig. 6.5b. For this purpose, the middle line should be functionalized with biomolecules. The functional groups present on the bead surface are bonded to the biomolecules situated on the middle line. When an electric current passes through one side line, the magnetic bead will be attracted by the magnetic field which is produced and the bonding between the two biomolecules will break.

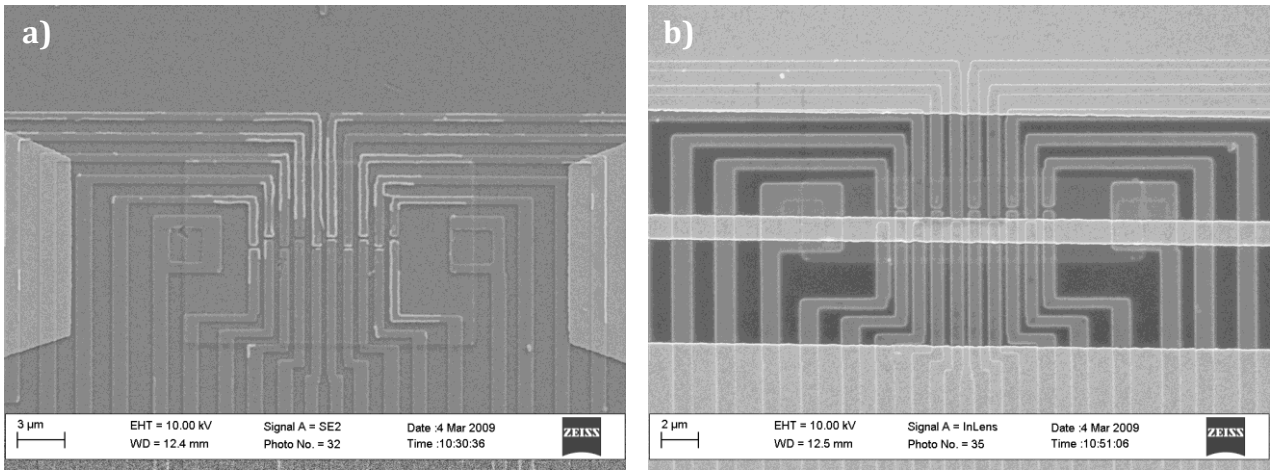

Fig. 6.5 a) Sensor array with magnetic field manipulation lines on top b) Sensor array with magnetic field manipulations lines for bond test measurements

The real time measurement of a magnetic bead trajectory was not achievable with the submicron TMR sensors array within the approaches presented above. The present state difficulties in achieving dynamic detection of magnetic beads with several recommended solutions are comprised in table 6.1.

In the future, different approaches for transportation and separation of magnetic beads are planned to be developed (159), (160). The magnetic ratchet is a transportation mechanism that employs the periodic on-off switching of an asymmetric potential and the freely diffusion of magnetic beads. The advantage of the magnetic ratchet system consists in their easy integration with the TMR sensor arrays, so as no micropumps are necessary. By combining the sensor arrays for magnetoresistive microscope purposes with integrated magnetic ratchets, the possibility to sense a magnetic bead trajectory becomes more likely.

Table 6.1 Encountered problems in real time measurements and proposed solution to them

Encountered problems	Proposed solutions
Capacitance effect	• New sensor array, where the manipulations lines are not contacting the sensors conduction lines • Approach different TaO_x thicknesses to reduce the capacitance effect (62)
Electrostatic discharge, cross talk, noise pickup	• Develop sensors that are having a low resistance and a high signal to noise ratio • Provide a better grounding for the sensors, resistive/capacitive shunt (161) • The sensors should be the last ones that are connected and the first disconnected for real time measurements • Supply a lead connection for sensor measurements
Increased height of the magnetic beads above the sensors	• Microchannels with a ramp construction would control the height of the magnetic beads above the sensors during dynamic measurements • By increasing the sensor area a higher amount of field will be catch by the sensor
Reaching sensitivity limits	• Provide an AC current through the manipulation lines or an out-of-plane AC magnetic field modulation for $1/f$ noise reduction

7. Conclusions and future perspectives

The idea of integrating MgO based TMR sensors with microfluidics and manipulation systems on a hand-held chip aims towards the implementation of superior biomedical devices. The TMR biosensors are able to detect a signal under the influence of magnetized magnetic beads or nanoparticles. For accurate biosensing purposes, the dimensions of the sensors, magnetic labels and biomolecules should be in the same size regime.

Considering the requirement of a very sensitive detection, the sensor's output must be linearized in order to observe the effect of the magnetic marker's stray field on the sensor. The linearization of the sensor is achieved by employing several thin films engineering procedures. The bottom ferromagnetic electrode is strongly pinned along the hard axis of the sensor, so it will not be affected by external applied magnetic fields. The tunneling crystalline MgO barrier is intercalated between CoFeB electrodes in order to achieve TMR ratios of up to 200%. The top soft ferromagnetic electrode orientates its magnetization along the long axis of the elliptical element. The fabrication of the MTJs elements employs e-beam lithography and of ion beam etching processes. The elements have increased shape anisotropy because their short axis has the length of 100 nm, while their long axis is 400 nm. These sensors present a linear response over a magnetic field range of ±500 Oe and sensitivities values of up to 0.1%/Oe. For biological use, the sensors are placed in a closed packed array where 20 sensors are distributed over an area of 18.2 μm^2.

The employment of these highly sensitive and linearized TMR sensors in magnetic markers detection have been investigated by performing static detection of magnetic beads and nanoparticles. The static detection of magnetic beads of 1 μm in diameter provides information regarding the position and orientation relative to the sensor. A good correla-

tion between experimental and simulation data regarding the high spatial resolutive detection of magnetic beads has been realized (162). Submicron sized magnetoresistive sensors are good candidates for the detection of nanometers sized magnetic nanoparticles, as well. The detection of 14 nm Co nanoparticles reveals the presence of a threshold in nanoparticle detection. It indicates a different detection signal coming from the non-interactive and coupling magnetic nanoparticles. When the 14 nm Co nanoparticles are dipolar coupled, the detected signal indicates a hysteretic behavior. The static detection of magnetic markers provides useful information regarding the orientation and interaction of magnetic nanoparticles.

For the integration of magnetoresistive sensors with biological entities, it is necessary to achieve dynamic detection of magnetic beads or nanoparticles in a liquid environment. Because the magnetic beads are distributed in aqueous medium, the distance between the labels and the sensors is increased. Thus, aiming for a real time detection of magnetic beads in microfluidic channels requires much sensitive sensors. A long term objective regarding magnetoresistive sensors development is directed at the exploration of low resistance sensors with an increased signal to noise ratio. A short term goal could be the introduction of magnetoresistive sensors with large dimensions. The sensor elements with an increased area, in the range of a few tens of micrometers squares, will display magnetic domains. The magnetic domains switch fast during magneto-transport measurements, arising the sensors sensitivity to 5.6%/Oe. By employing finite element method of simulation a different interaction of the magnetic bead with the TMR sensor of large dimension is revealed. By employing TMR sensors of large dimensions, the dynamic detection of magnetic beads situated in liquid above the sensors area could be achievable (163), (126).

When designing future approaches for tunneling magnetoresistive sensors, the dynamic detection of magnetic markers is obtainable only with sensors of large dimensions. So, extended sensors can be used when information regarding the presence or absence of magnetic labels is needed. If details regarding the orientation or interaction between the

magnetic labels are required, the spatial resolution provided by the submicron sized sensors is of great interest and already solved within this thesis.

Bibliography

1. *Biosensor: A Tutorial Review.* **S.P. Mohanty, E. Kougianos.** Issue 2, Potentials IEEE, 2006, Vol. Vol. 25, pp. Pag. 35-40 .

2. *The use of nanocrystals in biological detection.* **Alivisatos, P.** No. 1, Nature Biotechnology, 2004, Vol. Vol. 22, pp. Pag 47-51.

3. *Biosensors: Sense and Sensitivity.* **Turner, A. P. F.** No 5495, Science, 2000, Vol. Vol. 290.

4. *Electrochemical biosensors – Sensor principles and architectures.* **D. Grieshaber, R. MacKenzie, J. Vörös, E. Reimhult.**, Sensors , 2008, Vol. 8, pp. 1400-1458.

5. *Biosensor recognition elements.* **J. P. Chambers, B. P. Arulanandam, L. L. Matta, A. Weis, J. J. Valdes.**, Curr. Issues, Mol. Biol., 2008, Vol. 10, pp. 1-12.

6. *Immunosensors: The next generation.* **Turner, A. P. F.**, Nature Biotechnology, 1997, Vol. 15.

7. *Immunosensors: technology and opportunities in laboratory medicine.* **C. L. Morgan, D. J. Newman, C. P. Price.** 2, Clinical Chemistry, 1996, Vol. 42, pp. 193-209.

8. *Immunochemical potentiometric sensors.* **J. Janata, G. F. Blackburn.,** Annals New York Academy of Science, 1984.

9. *Surface plasmon resonance sensors: a review.* **J. Homola, S. S. Yee, G. Gauglitz.,** Sensors and Actuators, 1999, Vol. B 54, pp. 3-15.

10. *Present and future of surface plasmon resonance biosensors.* **Homola, J.,** Anal bioanal Chem, 2003, Vol. 377.

11. *Femtotesla magnetic field measurement with magnetoresistive sensors.* **M. Pannetier, C. Fermon, G. Le Goff, J. Simola, E. Kerr.** 2004, Science, Vol. 304, p. 1648.

12. Panhorst, M. *On-chip manipulation and positioning of biomolecules with magnetic beads.*, Bielefeld University, PhD thesis in physics, 2005.

13. *Design and performance of GMR sensors for the detection of magnetic microbeads in biosensors.* **J. C. Rife, M. M Miller, P. E Sheehan, C. R. Tamanaha, M.Tondra, L. J. Whitman.,** Sensors and Actuators A, 2003, Vol. 107, pp. 209-218.

14. *Magnetoresistive sensors.* **P. P Freitas, R. Ferreira, S. Cardoso and F. Cardoso.**,Journal of physics: Condensed Matter , 2007, Vol. 19. 165221 .

15. *Effect of spin-valve sensor magnetostatic fields on nanobead detection for biochip applications.* **H. A Ferreira, N. Feliciano, D. L. Graham, P. P Freitas.** 2005, Journal of Applied Physics, 97, 10Q904.

16. *Large tunnel magnetoresistance of 1056% at room temperature in MgO based double barrier magnetic tunnel junction.* **L. Jiang, H. Naganuma, M. Oogane, Y. Ando.** 083002, Applied Physics Express , 2009, Vol. 2.

17. *Magnetic bead handling on-chip: new opportunities for analytical applications.* **M. A. M. Gijs.** 2004, Microfluid Nanofluid, Vol. 1, pp. 22-40.

18. *The Stoner-Wohlfarth model of ferromagnetism.* **C. Tannous, J. Gieralttowski.,** Eur. J. Phys., 2008, Vol. 29, pp. 475-487.

19. *Superparamagnetic nanoparticles for biomedical applications: Possibilities and limitations of a new drug delivery system.* **T. Neuberger, B. Schöpf, H. Hofmann, M. Hofmann, B. von Rechenberg.** 2005, J. M.M.M, Vol. 293, pp. 483-496.

20. *Magnetic nanoparticles, applications beyond data storage.* **G. Reiss, A. Huetten.** 2005, Nature Materials, Vol. 4.

21. *Effects of superparamagnetism in MgO based magnetic tunnel junctions.* **W. Shen, B. D. Schrag, A. Girdhar, M. J. Carter, H. Sang, G. Xiao.**, Phys. Rev. B, 2009, Vol. 79. 014418.

22. *Magnetic nanoparticles.* **Kodama, R. H.**, M. M. M., 1999, Vol. 200, pp. 359-372.

23. *Thermal fluctuation of single-domain particle.* **Jr., W. Fuller Brown.** 5, Phys. Rev., 1963, Vol. 130.

24. *Nanoparticles – known and unknown health risks.* **P. H. M. Hoet, I. Brüske-Hohfeld, O. V. Salata.** 2004, J. of Biotechn., Vol. 2, p. 12.

25. Buschow, K. H. J. *Handbook of Magnetic Materials.*, Elsevier B. V, 2006. Vol. Vol. 16.

26. Getzlaff, M. *Fundamentals of Magnetism.*, Springer Verlag Berlin Heidelberg, 2008.

27. D. Sellmyer, R. Skomski. *Advanced Magentic Nanostructures.*, Springer, 2006.

28. *Characterisation of Dynabeads® by magnetization measurements and Mössbauer spectroscopy.* **G. Fonnum, C. Johansson, A. Molteberg, S. Mørup, E. Aksnes.** 2005, JMMM, Vol. 293, pp. 41-47.

29. Ennen, I. *Magnetische Nanopartikel als Bausteine fuer granulare Systeme: Mikrostruktur, Magnetismus und Transporteigenschaften.* Bielefeld University, PhD Thesis, 2008.

30. *New magnetic nanoparticles for biotechnology.* **A. Hütten, D. Sudfeld, I. Ennen, G. Reiss, W. Hachmann, U. Heinzmann, K. Wojczykowski, P. Jutzi, W. Saikaly, G. Thomas.** 2004, Journal of Biotechnology, Vol. 112, pp. 47-63.

31. *Ferromagentic CoFe nanoparticles for biotechnology.* **A. Hütten, D. Sudfeld, I. Ennen, G. Reiss, K. Wojczykowski, P. Jutzi.** 2005, JMMM, Vol. 293, pp. 93-101.

32. *Colliodal nanocrystal shape and size control: the case of cobalt.* **V. F. Puntes, K. M. Krishnan, A. P. Alivisatos.** 2001, Science, Vol. 291.

33. *Antibody immobilization on magnetic particles.* **A. C. A. Roque, S. Bispo, A. R. N. Pinheiro, J. M. A. Antunes, D. Gonçalves, H. A. Ferreira .** 2008, J. Mol. Recognit.

34. H. Kronmueller, S. Parkin. *Handbook of magnetism and advanced magnetic materials, Vol. 2 Micromagnetism.,* Willley, 2007.

35. *Growth-induced uniaxial in-plane magnetic anisotropy for ultrathin Fe deposited on MgO(001) by oblique incidence molecular beam epitaxy.* **Y. Park, E. E. Fullerton, S. D. Bader.** 16, Appl. Phys. Lett., 1995, Vol. 66 .

36. Heinrich, B. *Ultrathin magnetic structures II.* [ed.] J.A.C Bland., Springer Verlag, 1994.

37. *Oscillatory coupling between ferromagnetic layers separated by a non-magnetic metal spacer.* **P. Bruno, C. Chappert.** 12, Phys. Rev. Lett., 1991, Vol. 67.

38. *Theory of interlayer magnetic coupling.* **Bruno, P.,** Physical Review B, 1995, Vol. 52.

39. *http://nobelprize.org/nobel_prizes/physics/laureates/2007/press.html.*

40. Chapter 5. *Tunneling phenomena in solids.* New York : Plenum Press, 1969.

41. M. J. Thornton,. *Spin electronics, Chapter 7.* [ed.] M. Ziese., Springer-Verlag Berlin Heidelberg, 2001. pp. pp 15-171. LNP 569.

42. *Magnetoelectronics.* **Gary A. Prinz, et al.** 1660, Science, 1998, Vol. 282.

43. *Spin-dependent tunneling in magnetic tunnel junctions.* **E. Y. Tsymbal, O. N. Mryasov, P. R. LeClair.** J. Phys. Condens. Matter, 2003, Vol. 15.

44. *Tunneling between ferromagnetic films.* **Julliere, M.**, Physics Letters 3, 1975, Vol. 54A.

45. *230% room-temperature magentoresistance in CoFeB/MgO/CoFeB magnetic tunnel junctions.* **D. D. Djayaprawira, K. Tsunekawa, M. Nagai, H. Maehara, S. Yamagata, N, Watanabe.,** Appl. Phys. Lett, 2005, Vol. 86. 092502.

46. *Large magnetoresistance in bcc Co/MgO/Co and FeCo/MgO/FeCo tunnel junctions.* **X.-G. Zhang, W. H. Butler.,** Physical Review B, 2004, Vol. 70. 172407.

47. *Effect of electrode composition on the tunneling magnetoresistance of pseudo-spin-valve magnetic tunnel junction with a MgO tunnel barrier.* **Y. M. Lee, J. Hayakawa, S. Ikeda, F. Matsukura, H. Ohno.,** Appl. Phys. Lett., 2007, Vol. 90. 212507.

48. *Highly spin-polarized materials and devices for spintronics.* **K. Inomata, N. Ikeda, N. Tezuka, R. Goto, S. Sugimoto, M. Wojcik, E. Jedryka.** Sci., Technol. Adv. Matter, 2008, Vol. 9 . 014101 .

49. *Magnetic tunnel junctions.* **J-G. Zhu, C. Park.,** Materials Today 11, 2006, Vol. 9.

50. L. I. Maissel, M. H. Francombe. *An introduction to thin films.*, Gordon and Breach Science Publishers, 1973.

51. *Nanoelectronics and information technology, Advanced electronic materials and novel devices.*, Willey-VCH Verlag, 2003.

52. O., Milton. *Materials science of thin films, deposition and structure.*, Academic Press, 2002, Second Edition.

53. http://www.oerlikon.com/leyboldvacuum/. [Online]

54. http://www.huettinger.com/produkte/plasmaanregung/truplasma-rf.html. [Online]

55. Thomas, A. *Preparation and characterization of magnetic single and double barrier junctions.*, Bielefeld University, PhD Thesis, 2003.

56. Drewello, V. *Untersuchung der Spinpolarization von 3d Ferromagneten in MgO Tunnelsystemen.*, Bielefeld University, Diplomarbeit in Physik, 2006 .

57. http://www.crystec.de/. [Online]

58. http://www.zeiss.de. [Online]

59. http://www.raith.com. [Online]

60. http://allresist.de. [Online]

61. http://www.sigmaaldrich.com. [Online]

62. *Tantalum oxide thin films as protective coatings for sensors.* **C. Christensen, R. de Reus, S. Bouwstra.**, J. Micromech.Microeng, 1999, Vol. 9, pp. 113-119.

63. *Tantalum pentaoxide (Ta2O5) thin films for advanced dielectric applications.* **C. Chaneliere, J. L. Autran, R. A. B. Devine, B. Balland.,** Materials Science and Engineering, 1988, Vol. R22, pp. 269-322.

64. *Shape-anisotropy-controlled magnetoresistive response in magentic tunnel junctions.* **Y. Lu, R. A. Altman, A. Marley, S. A. Rishton, P. L. Trouilloud, G. Xiao, W. J. Gallagher, S. S. P. Parkin.**, Appl. Phys. Lett. 19, 1997, Vol. 70, pp. 2610-2612.

65. Getzlaff, M. *Fundamentals of Magnetism.* s.l. : Springer Verlag Berlin Heidelberg, 2008.

66. Schotter, Jörg. *Development of a magnetoresistive biosensor for the detection of biomolecules.*, Bielefeld University, PhD thesis, 2004.

67. *Magnetic characterization of CoFeB/MgO and CoFe/MgO interfaces.* **E. Negusse, A. Lussier, J. Dvorak, Y. U. Idzerda, S. R. Shinde, Y. Furukawa, K. Tsunekawa, D. D. Djayaprawira.,** Appl. Phys. Lett., 2007, Vol. 90. 092502.

68. M. Ziese, M. J. Thornton. *Spin electronics.*, Springer-Verlag Berlin Heidelberg, 2001.

69. *Low-frequency noise in magnetic tunnel junctions.* **C. Ren, X. Liu, B. D. Schrag, G. Xiao.,** Phys. Rev. B., 2004, Vol. 69. 104405.

70. *Low-frequency magnetic and resistance noise in magnetic tunnel junctions.* **L. Jiang, E. R. Nowak, P. E. Scott, J. Johnson, J. M. Slaughter, J. J. Sun, R. W. Dave.** 054407, Phys. Rev. B, 2004, Vol. 69.

71. *Low-frequency magnetic noise in micron-scale magnetic tunnel junctions.* **S. Ingvarsson, G. Xiao, S. S. P. Parkin, W. J. Gallagher, G. Grinstein, R. H. Koch.**, Physical Review Letters 15, 2000 , Vol. 85.

72. *Electronic noise in magnetic tunnel junctions.* **S. Ingvarsson, G. Xiao, R. A. Wanner, P. Trouilloud, Y. Lu, W. J. Gallagher, A. Marley, K. P. Roche and S. S. P. Parkin.**, J. Appl. Phys. 8, 1999, Vol. 85.

73. *Low-frequency noise measurements on commercial magnetoresistive magnetic field sensors.* **N. A. Stutzke, S. E. Russek, D. P. Pappas, M. Tondra.,** Journal of Applied Physics, 2005, Vol. 97. 10Q107.

74. *Noise in small magnetic systems – applications to very sensitive magnetorestive sensors.* **M. Pannetier, C. Fermon, G. Le Goff, J. Simola, E. Kerr, J. M. D. Coey.,** Journal of Magnetism and Magnetic Materials, 2005, Vols. 290-291, pp. 1158-1160.

75. *A method to design high SNR nanoscale magnetic sensors using an array of tunneling magneto-resistance (TMR) devices.* **P. Gomez, D. Litvinov, S. Khizroev.,** J. Phys.D: Appl. Phys., 2007, Vol. 40.

76. *Ueber die synthese ferromagnetischer manganlegierungen.* **Heusler, Fr.,** Verhandlungen der Deutschen Physikalischen Gesellschaft, 1903, Vol. 5, pp. 219-223.

77. Venkatesan, M. Half-metals. [ed.] Helmut Kronmueller and Stuart Parkin. *Handbook of Magnetism and Advanced Magentic Materials.*, John Wiley & Sons, 2007, Vol. 4 Novel Materials .

78. *Tunnel magnetoresistance in magnetic tunnel junctions with Co2Fe(Al,Si) full Heusler films.* **N. Tezuka, N. Ikeda, A. Miyazaki, S. Okamura, M. Kikuchi, S. Sugimoto, K. Inomata.,** J. Magn. and Magn. Materials, 2007, Vol. 310.

79. Groot, Rober A. de. Heusler Alloys. [ed.] Helmut Kronmueller and Stuart Parkin. *Handbook of Magnetism and Magentic Materials.*, John Wiley & Sons, 2007, Vol. 4 Novel Materials.

80. *Films of Heusler alloys.* **D. Dubowik, I. Gościańska, A. Szlaferek, Y. V. Kudryavtsev.**, Materials Science-Poland 2, 2007, Vol. 25.

81. *Preparation of Heusler thin films: The quaternary alloy Co2Fe0.5Mn0.5Si.* **D. Ebke, A. Thomas, A. Huetten, B. Balke, C. Felser, J. Schmalhorst, G. Reiss.** 10, Phys. Stat. Sol. (a), 2008, Vol. 205, pp. 2298-2301.

82. *Large tunnel magnetoresistance in tunnel junctions with Co2MnSi/Co2FeSi multilayer electrode.* **D. Ebke, J. Schmalhorst, N.-N. Liu, A. Thomas, G. Reiss.** Appl. Phys. Lett. , 2006, Vol. 89. 162506.

83. *Role of structural defects on the half-metallic character of Co2MnGe and Co2MnSi Heusler alloys.* **S. Picozzi, A. Continenza, A. J. Freeman.,** Phys. Rev. B, 2004, Vol. 66. 094423.

84. *Highly spin-polarized materials and devices for spintronics.* **K. Inomata, N. Ikeda, N. Tezuka, R. Goto, S. Sugimoto, M. Wojcik, E. Jedryka.,** Sci. Technol. Adv. Mater, 2008, Vol. 9.

85. *Magnetic microstructure of candidates for epitaxial dual Heusler magnetic tunnel junctions.* **A. Kaiser, D. Banarjee, A. D. Rata, C. Wiemann, S. Cramm, C. M. Schneider.,** J. Magn. and Magn. Materials, 2008.

86. *Investigation of Co2FeSi: The Heusler compound with highest Curie temperature and magnetic moment.* **S. Wurmehl, G. H. Fecher, H. C. Kandpal, H-J. Lin.,** Appl. Phys. Lett., 2006, Vol. 88. 032503.

87. *Current-perpendicular-to-plane giant magnetoresistance of a spin valve using Co2MnSi Heusler alloy electrodes.* **K. Kodama, T. Furubayashi, H. Sukegawa, T. M. Nakatani, K. Inomata, K. Hono, .**

88. *Spin polarization of Co2FeSi full-Heusler alloy and tunneling magnetoresistance of its magnetic tunneling junctions.* **Z. Gercsi, A. Rajanikanth, Y. K. Takahashi, K. Hono, M. Kikuchi, N. Tezuka, K. Inomata.,** Appl. Phys. Lett., 2006, Vol. 89. 082512.

89. *Characterization of half-metallic L21- phase Co2FeSi full-Heusler alloy thin films formed by rapid thermal annealing.* **Y. Takamura, R. Nakane, H. Munekata, S. Sugahara.,** J. Appl. Phys., 2008, Vol. 103. 07D719.

90. *Structural properties of magnetic Heusler alloys.* **A. Ayuela, J. Enkovaara, K. Ullako, R. M. Nieminem.,** J. Phys.: Condens. Matter, 1999, Vol. 11.

91. *Low ordering temperature and high tunnel magnetoresistance in Co2FeAl/MgO/CoFe magnetic tunnel junctions* . **D. Ebke, P. Thomas, O. Schebaum, M. Scaefers, D. Nissen, A. Huetten, A. Thomas.** in press, 2009.

92. *Spin valve sensors for ultrasensitive detection of superparamagnetic nanoparticles for biological applications.* **G. Li, S. Sun, R. J. Wilson, R. L. White, N. Pourmand, S. X. Wang.** 2006, Sens. And Act. A 126, pp. 13030-13035.

93. *Giant magnetoresistive sensors. 2. Detection of biorecognition events at self referencing and magnetically tagged arrays.* **R. L. Millen, J. Nordling, H. A. Bullen, M. D. Porter, M. Tondra, M. C. Cranger.** 2008, Anal. Chem 80 (21).

94. *Giant magnetoresistance sensors 1. Internally calibrated readout of scanned magnetic arrays.* **J. Nordling, R. L. Millen, H. A. Bullen, M. D. Porter, M. Tondra, M. C. Granger.** 2008, Anal. Chem.80 (21) .

95. *Detection of ferromagnetic particles using spin valve sensors.* **L. W. Y. Lui, Y. Y. Tan, K. B. Li, C. H. Sow, S. J. O'Shea.,** Journal of Appl. Phys., 2006, Vol. 100. 044909.

96. *Model for detection of immobilized superpara-magnetic nanosphere assay labels using giant magnetoresistive sensors.* **M. Tondra, M. Porter, R. J. Lipert** J., Vac. Sci. Technol. 4, 2000, Vol. A 18.

97. *Detection and manipulation of biomolecules by magnetic carriers.* **M. Brzeska, M. Panhorst, P. B. Kamp, J. Schotter, G. Reiss, A. Puehler, A. Becker, H. Brueckl.,** J. of Bio-techn, 2004, Vol. 112.

98. *Single molecule detection with magnetic beads – computer simulation.* **W. Schepper, J. Schotter, H. Brückl, G. Reiss.,** Journal of Magn. and Magn. Mat., 2004, pp. 272-272.

99. *Analyzing a magnetic molecule detection system – computer simulation.* **W. Schepper, J. Schotter, H. Brückl, G. Reiss.,** Journal of Biotechnol., 2004, Vol. 112.

100. *Comparison of a prototype magnetoresistive biosensor to standard DNA detection.* **J. Schotter, P. B. Kamp, A. Becker, A. Pühler, G. Reiss, H. Brückl.,** Biosensors and Bioelectronics, 2004, Vol. 19, pp. 1149-1156 .

101. *A biochip based on magnetoresistive sensors.* **J. Schotter, P. B. Kamp, A. Becker, A. Pühler, D. Brinkmann, W. Schepper, H. Brückl, G. Reiss.**, IEEE Transaction on magnetic 5, 2002, Vol. 38.

102. *Magnetoresistive sensors and magnetic nanoparticles for biotechnology.* **G. Reiss, H. Brueckl. A. Huetten, J. Schotter, M. Brzeska, M. Panhorst, D. Sudfeld, A. Becker, P. B. Kamp, A. Puehler, K. Wojczykowscki, P. Jutzi.,** J. Mater. Res., 2005, Vol. 20.

103. *New materials and applications for magnetic tunnel junctions.* **G. Reiss, J. Schmalhorst, H. Brückl, A. Thomas, J. Schotter, M. Brzeska, A. Hütten, S. Kämmerer.,** Mol. Phys. Rep., 2004, Vol. 40.

104. *Spin valve sensors.* **P. P. Freitas, F. Silva, N. J. Oliveira, L. V. Melo, L. Costa, N. Almeida.,** Sensors and Actuators A, 2000, Vol. 81, pp. 2-8.

105. *Single magnetic microsphere placement and detection on-chip using current line designs with integrated spin valve sensors: Biotechnological applications.* **D. L. Graham, H. Ferreira, J. Bernardo, J. M. S. Cabral.**, Journ. of Appl. Phys. 10, 2002, Vol. 91.

106. *On-chip manipulation and magnetization assessment of magnetic bead ensembles by integrated spin-valve sensors.* **L. Lagae, R. Wirix-Speetjens, J. Das, D. Graham, H. Ferreira, P. P. F Freitas, G. Borghs, J. De Boek.**, Journ. of Appl. Phys. 10, 2002 , Vol. 91.

107. *High sensitivity detection of molecular recognition using magnetically labeled biomolecules and magentoresistive sensors.* **D. L. Graham, H. A. Ferreira, P. P. Freitas, J. M. S. Cabral.**, Biosens. and Bioel., 2003, Vol. 18.

108. *Magnetoresistive-based biosensors and biochips.* **D. L. Graham, H. A. Ferreira, P. P. Freitas.,** Trends in Biotechn., 2004, Vol. 22.

109. *Biodetection of magnetically labeled biomolecules and arrays of spin-valves sensors.* **H. A. Ferreira, D. L. Graham, P. P. Freitas, J. M. S. Cabral.**, J. Appl. Phys. 10, 2003, Vol. 93.

110. *Effect of spin-valve sensor magnetostatic fields on nanobead detection for biochip applications.* **H. A. Ferriera, N. Feliciano, D. L. Graham, P. P. Freitas.** J., Appl. Phys, 2005, Vol. 97. 10Q904.

111. *Rapid DNA hybridization based on ac field focusing of magnetically labeled target DNA.* **H. A. Ferreira, N. Feliciano, D. L. Graham, L. A. Clarke, M. D. Amaral, P. P. Freitas.,** Appl. Phys. Lett., 2005, Vol. 87. 013901.

112. *Magnetoresistive DNA chips based on ac field focusing of magnetic labels.* **H. A. Ferreira, F. A. Cardoso, R. Ferreira, S. Cardoso, P. P. Freitas.,** J. Appl. Phys., 2006, Vol. 99. 08P105.

113. *Detection of 130 nm magnetic particles by a portable electronic plat-form using spin valve and magnetic tunnel junction sensors.* **F. A. Cardoso, J. Germano, R. Ferreira, S. Cardoso, V. C. Martins, P. P. Freitas, M. S. Piedade, L. Sousa.**, J. Appl. Phys., 2008, Vol. 103. 07A310.

114. *Diode/magnetic tunnel junction cell for fully scalable matrix-based biochip.* **F. A. Cardoso, H. A. Ferreira, J. P. Conde, V. Chu, P. P. Freitas, D. Vidal.,** J. Appl. Phys., 2006, Vol. 99. 08B307.

115. *Tuning MgO barrier magnetic tunnel junction bias current for picotesla magnetic field detection.* **R. Ferreira, P. Wisniowski, P. P. Freitas, J. Langer, B. Ocker, W. Maass.,** J. Appl. Phys. , 2006, Vol. 99. 08K706.

116. *Detection of single micron-sized magnetic bead and magnetic nanoparticles using spin-valve sensors for biological applications.* **G. Li, V. Joshi, R. L. White, S. X. Wang, J. T. Kemp, C. Webb, R. W. Davis, S. Sun,.** 10, J. Appl. Phys., 2003, Vol. 93.

117. *Spin valve biosensors: Signal dependence on nanoparticle position.* **G. Li, S. Sun, S. X. Wang.**, J. Appl. Phys., 2006, Vol. 99. 08P107.

118. *Towards a magnetic microarray for sensitive diagnostics.* **S. X. Wang, S-Y. Bae, G. Li, S. Sun, R. L. White, J. T. Kemp, C. D. Webb.,** J. M. M. M., 2005, Vol. 293.

119. *Bio-functionalization of monodispersed magnetic nanoparticles and their use as biomolecular labels in a magnetic tunnel junction based sensor.* **S. G. Grancharov, H. Zeng, S. Sun, S. X. Wang, S. O'Brien, C. B. Murray, J. R. Kirtley, G. A. Held,** J. Phys. Chem. B, 2005, Vol. 109, pp. 13030-13035.

120. *Advances in giant magnetoresistance biosensors with magnetic nanoparticle tags: review and outlook.* **S. X. Wang, G. Li .**, IEEE Trans. on Magn.7, 2008, Vol. 44.

121. *A biosensor based on magnetoresistance technology.* **D. R. Baselt, G. U. Lee, M. Natesan, S. W. Metzger, P. E. Sheehan, R. J. Colton.**, Biosens.Bioel., 1998, Vol. 12, pp. 731-739.

122. *The BARC biosensor applied to the detection of biological warfare agents.* **R. L. Edelstein, C. R. Tanamaha, P. E. Sheehan, M. M. Miller, D. R. Baselt, L. J. Whitmann, R. J. Colton.,** Biosens. Bioel., 2000, Vol. 14, pp. 805-813.

123. *A DNA array sensor utilizing magnetic microbeads and magne-toelectronic detection.* **M. M. Miller, P. E. Sheehan, R. L. Edelstein, C. R. Tamanaha, L. Zhong, S. Bounnak, L. J. Whitman, R. J. Colton.,** J. M. M. M., 2001, Vol. 225, pp. 138-144.

124. *Detection limits for nanoscale biosensors.* **P. E. Sheehan, L. J. Whitman.** 4, Nano Lett., 2005 , Vol. 5.

125. *Attomolar protein detection in complex sample matrices with semi-homogenous fluidic force discrimination assays.* **S. P. Mulvaney, K. M. Myers, P. E. Sheehan, L. J. Whitman.**, Bios. Bioel., 2009, Vol. 24, pp. 1109-1115.

126. *In situ detection of single micron-sized magnetic beads using magnetic tunnel junction sensors.* **W. Shen, X. Liu, D. Mazumdar, G. Xiao.,** Appl. Phys. Lett., 2005, Vol. 86. 253901.

127. *Detection of DNA labeled with magnetic nanoparticles using MgO-based magnetic tunnel junction sensors.* **W. Shen, B. D. Schrag, M. J. Carter, J. Xie, C. Xu, S. Sun, G. Xiao.,** Journ. of Appl. Phys., 2008, Vol. 103. 07A306.

128. *Measurement of the concentraction of magnetic nanoparticles in a fluid using giant magnetoresistance sensor with a trench.* **R. E. Thilwind, M. Megens, J. B. A. D. von Zon, R. Coehoorn, M. W. J. Prins.**, J. M. M. M., 2008, Vol. 320, pp. 486-489.

129. *On-chip manipulation and detection of magentic particles for functional biosensors.* **X. J. A. Janssen, L. J. van Ijzendoorn, M. W. J. Prins.**, Biosens. Bioel., 2008, Vol. 23, pp. 833-838.

130. *Analysis of individual magentic particle motion near a chip surface.* **K. van Ommering, C. C. H. Lamers, J. H. Nieuwenhuis, L. J. van IJzendoorn, M. W. J. Prins.**, J. Appl. Phys., 2009, Vol. 105. 104905.

131. *Optimizing the geometry of an in vitro tunneling magnetoresistance biosensor using an immobilized ferrimagnetic nanoparticle agent.* **S. Kim, S. Bae.,** J. Appl. Phys., 2008, Vol. 104. 113911.

132. *Improvements of sensing performance by specially designed shield layer in an in vitro tunneling magnetoresistance biosensor using immobilized ferrimagnetic nanoparticles agents.* **S. Kim, S. Bae, J. K. Lim.,** J. Appl. Phys., 2008, Vol. 103. 07E916.

133. *Micromagnetic simulation of spin valves with synthetic free and pinned layers and detection of magnetic labels with AC field.* **Y. Liu, Z. Hou.** 6, IEEE Trans. Magn., 2007 , Vol. 43.

134. *Microfabricated tools for manipulation and analysis of magnetic microcarries.* **M. Tondra, A. Popple, A. Jander, R. L. Millen, N. Pekas, M. D. Porter.**, J. M. M. M., 2005, Vol. 293, pp. 725-730.

135. *Giant magnetoresistive sensors and superparamagnetic nanoparticles: A chip-scale detection strategy for immunosorbent assays.* **R. L. Millen, T. Kawaguchi, M, C. Granger, M. D. Porter, M. Tondra.** 21, s.l. : Anal. Chem., 2008, Vol. 80.

136.http://tools.invitrogen.com/content/sfs/brochures/Surface_Activated_Dynabeads.PDF. [Online]

137. Weddemann, Alexander. *Micromagnetic simulation, PhD thesis.* Bielefeld Bielefled University, 2009.

138. *Cellular basis of mechanotransduction.* **Ingber, D. E.** 23-327, s.l. : Biol. Bull., 1998, Vol. 194.

139. *Mechanotransduction across the cell surface and through the cytoskeleton.* **N. Wang, P. P. Butler, D. E. Ingber.**, Science, 1993, Vol. 260.

140. *Microtubules can bear enhanced compressive loads in living cells because of lateral reinforcement.* **C. P. Brangwynne, F. C. MacKintosh, S. Kumar, N. A. Geisse, J. Talbot, L. Mahadevan, K. K. Parker, D. E. Ingber, D. A. Weitz.**, The Journal of Cell Biology 5, 2006, Vol. 173, pp. 733-741.

141. *Mechanical behavior in living cells consis-tent with the tensegrity model.* **N. Wang, K. Naruse, S. Stamenović, J. J. Fredberg, S. M. Mijailovich, I. M. Tolić-Nørrelykke, T. polte, R. Mannix, D. E. Ingber.**, PNAS 14, 2001, Vol. 98.

142. *Mechanical control of tissue growth: Function follows form.* **Ingber, D. E.**, PNAS 33, 2005, Vol. 102.

143. *Probing single molecule dynamics.* **X. S. Xie, R. C. Dunn.,** Science, 1994, Vol. 265.

144. *Fluorescence spectroscopy of single biomolecules.* **S. Weiss et. al.**, Science 1676, 1999, Vol. 283.

145. *Illuminating single molecules in condensed matter.* **W. E. Moerner et. al.**, Science 5408, 1999, Vol. 283.

146. *Nanometer-localized multiple single-molecule fluorescence microscopy.* **X. Qu, D. Wu, L. Mets, N. F. Scherer.**, PNAS 31, 2004, Vol. 101.

147. Hedwig, Peter. *Dynamic detection of magentic markers.* Diploma thesis, Bielefeld University, 2009.

148. http://www.lakeshore.com/mag/hlp/hpm.html. [Online]

149. http://www.geocities.com/guerinlj/. [Online]

150. *A hydrodynamic switch Microfluidic separation system for magnetic beads.* **A. Weddemann, F. Wittbracht, A. Auge and A, Huetten.**, Appl .Phys. Lett., 2009, Vol. 94, p. 173501.

151. *Integrated microfluidic isolation platform for magnetic particle manipulation in biological systems.* **E. Mirowski, J. Moreland, S. E. Russek, M. J. Donahue.**, Appl. Phys. Lett 10, 2004, Vol. 84, pp. 1786-1788.

152. *Fabrication of topologically complex three-dimensional microfluidic systems in PDMS by rapid prototyping.* **J. R. Anderson, D. T. Chiu, R. J. Jackman, O. Cherniavskaya, J.C. McDonald, H. Wu, S. H. Whitesides, and G. M. Whitesides.** Anal. Chem., 2000, Vol. 72, pp. 3158-3164.

153. *Towards ferrofluidics for micro-TAS and lab on-a-chip applications.* **L. Mao and H. Koser.** s.l. : Nanotechnology, 2006, Vol. 17, pp. 34-47.

154. *Magnetism and microfluidics.* **Pamme, N.,** Lab Chip, 2006, Vol. 6, pp. 24-38.

155. *Fabrication of an SU-8 based microfluidic reactor on a PEEK susbstrate sealed by a 'flexible semi-solid transfer' (FST) process.* **Y. Song, C. S. S. R. Kumar, and J. Hormes.,** J. Micromech. Microeng. , 2004, Vol. 14, pp. 932-940.

156. *An integrated microfluidic cell for detection, manipulation, and sorting of single micron-sized magnetic beads.* 2006.

157. *Microfluidic large-scale integration.* **T. Thorsen, S. J. Maerkl, and S. R. Quake.,** Science, 2002, Vol. 298, pp. 580-584.

158. *Dielectric breakdown in Co-Fe-B/MgO/Co-Fe-B magnetic tunnel junction.* **A. A. Khan, J. Schmalhorst, A. Thomas, O. Schebaum, and G. Reiss.,** J. Appl. Phys., 2008, Vol. 103, p. 123705.

159. *Magnetic ratchet for biotechnological applications.* **A. Auge, A. Weddemann, F. Wittbracht, and A. Hütten.,** Appl. Phys. Lett, 2009, Vol. 94, p. 183507.

160. Auge, A. *Magnetic ratchet.,* Master thesis, Bielefeld University, 2008.

161. E. Cheuk, W. Leung, A. Wai, Y. Lai, P. Kin, W. D. Hu, M. Dovek, R. Lee. *ESD, cross talk and noise pickup minimizing scheme for CPP and TMR devices. AG11B512FI* 2008.

162. *Tunneling magnetoresistance sensors for high resolutive particle detection.* **C. Albon, A. Weddemann, A. Auge, K. Rott, A. Huetten.,** Appl. Phys. Lett. , 2009, Vol. 95. 023101.

163. *Toward a magentoresistive chip cytometer: Integrated detection of magnetic beads flowing at cm/s velocities in microfluidic channels.* **J. Loureiro, R. Ferreira, S. Cardoso, P. P. Freitas, J. Germano, C. Fermon, G. Arrias, M. Pannetier-Lecoeur, F. Rivadulla, and J. Rivas.,** Appl. Phys. Lett., 2009, Vol. 95. 034104.

164. *Femtotesla magnetic field measurement with magnetoresistive sensors.* **M. Pannetier, C. Fermon, G. Le Goff, J. Simola, E. Kerr,** 2004, Science, Vol. 304, p. 1648.

165. *230% room-temperature magentoresistance in CoFeB/MgO/CoFeB magnetic tunnel junctions.* **D. D. Djayaprawira, K. tsunekawa, M. Nagai, H. Maehara, S. Yamagata, N, Watanabe.,** Appl. Phys. Lett, 2005, Vol. 86. 092502.

166. *Effect of electrode composition on the tunneling magnetoresistance of pseudo-spin-valve magnetic tunnel junction with a MgO tunnel barrier.* **Y. M. Lee, J. Hayakawa, S. Ikeda, F. Matsukura, H. Ohno,** Appl. Phys. Lett. , 2007, Vol. 90. 212507.

167. http://www.rothrau.de. [Online]

168. Groot, Rober A. de. Heusler Alloys. [ed.] Helmut Kronmueller and Stuart Parkin. *Handbook of Magnetism and Magentic Materials.*, John Wiley & Sons, 2007, Vol. 4 Novel Materials.

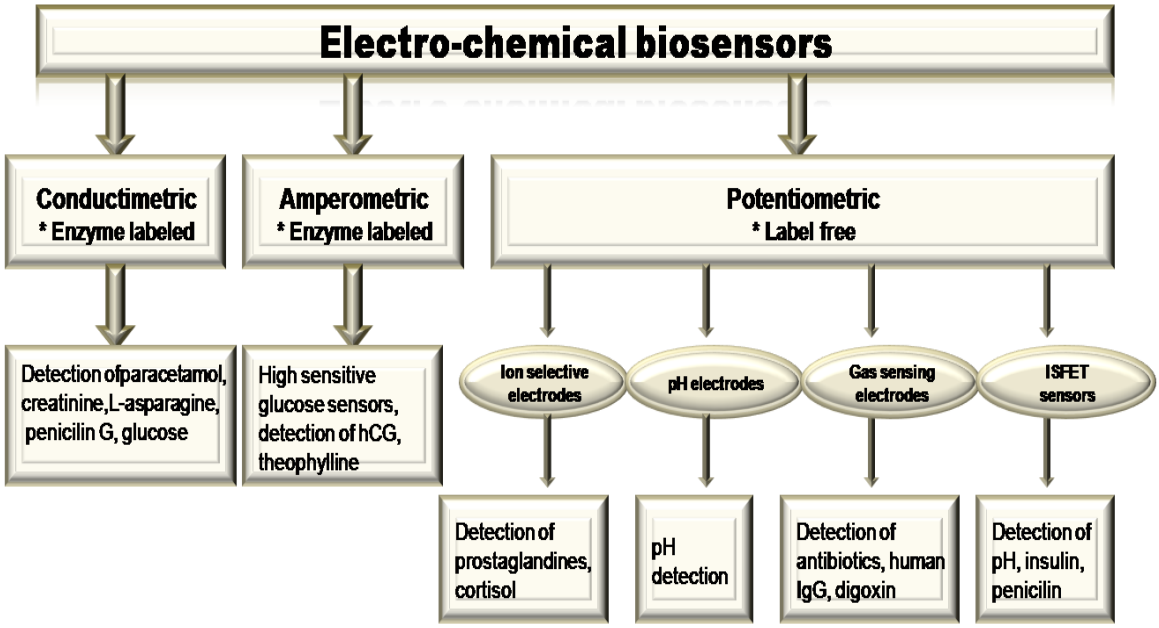

ANNEX I Classification of electro-chemical biosensors

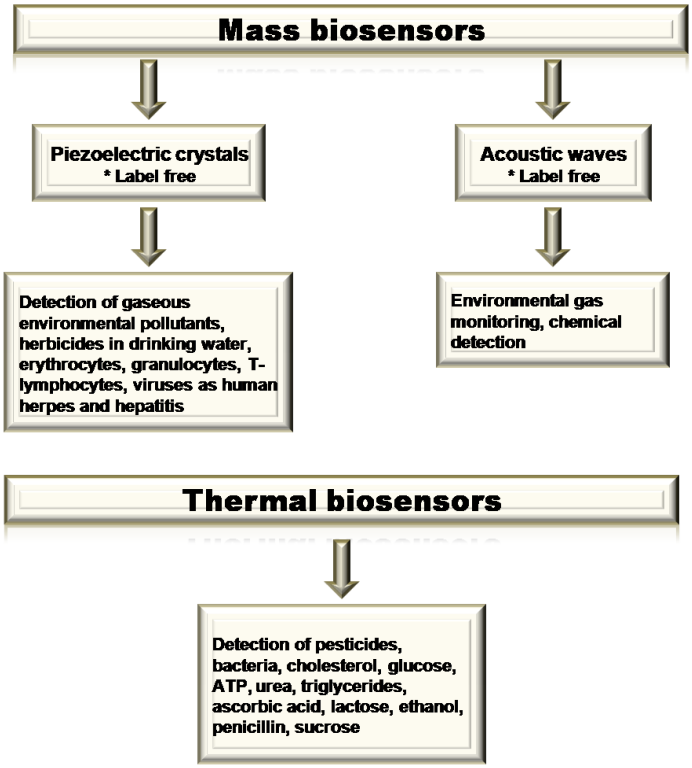

ANNEX II Classification of mass and thermal biosensors

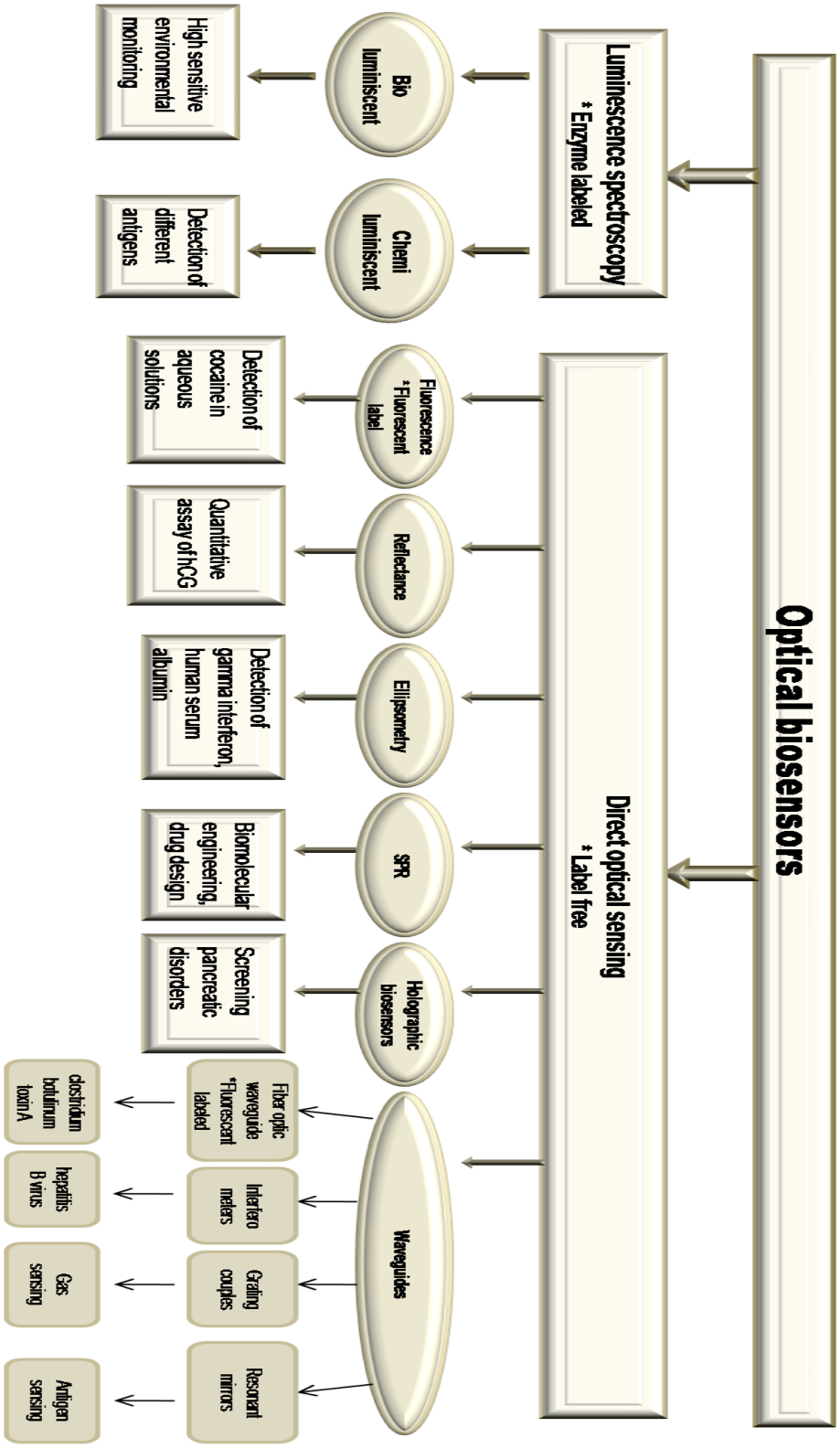

ANNEX III Classification of optical biosensors

Acknowledgements

I am grateful for being accepted to work in the TMR based biosensors project, for the interesting topic of the thesis that has been attributed to me. Without the continuous help from all the co-workers in the D2 group this thesis could not be possible. I would like to thank especially to my supervisors **Prof. Dr. Andreas Hütten, Dr. Michael Schilling** and **Prof. Dr. Günter Reiss** for the support and funding of this thesis. Particularly, I would like to thank **Dr. Karsten Rott** for introducing me in the lab work and for his perpetual patience with me. His knowledge and thrust offer me the foundation for the work done throughout this thesis.

Exceptional I would like to thank **Alexander Weddemann** for providing the simulation results. I am thankful to **Patryk Krzysteczko, Peter Hedwig, Alexander Auge** and **Daniel Ebke** for proofreading parts of the thesis. Their encouragements and fruitful discussions were of great help. Notably I would like to thank **Frank Wittbracht** and **Dieter Akemeier** for the group atmosphere they introduced in the biosensing projects.

Moreover I would like to thank to **Dr. Simone Herth**, **Dr. Jan Schmalhorst** and **PD Dr. Andy Thomas** for their helpful and suggestive comments done during several steps in my work.

I would like to thank to all the persons responsible for the machines that had to be utilized for the work of the thesis. Without their great care and proper maintenance a lot from this work could not be done. I would like to thank to **Volker Drewello**, **Oliver Schebaum, Inga Ennen, Britta Vogel, Dirk Meyners** and mainly to **Markus Schäfers** for their help and orientation they offered me throughout the work in these years.

Furthermore I would like to thank **A. G. Venkatesh**, **Ning Ning Liu**, **A. Khan**, **K. Bhutta and M. Meinert** for the beautiful time we spend together having scientifically talks and not only.

Last, but not least I would like to thank my family and friends for their permanent reinforcements they provide throughout the years.